2010

Stress concentration factors for v-notched plates under axisymmetric pressure

Nathan J. Mutter
University of Central Florida, njmutter@hollandhart.com

STRESS CONCENTRATION FACTORS FOR V-NOTCHED PLATES UNDER AXISYMMETRIC PRESSURE

by

NATHAN J. MUTTER

A Thesis submitted in partial fulfillment of the requirements
for the Honors in the Major Program in Mechanical Engineering
in the College Engineering and Computer Science
and in the Burnett Honors College
at the University of Central Florida
Orlando, Florida

Spring Term 2010

Thesis Chair: Dr. Ali P. Gordon

Abstract

The topic of this thesis is the investigation of the local states of stress resulting from the introduction of a v-notch in a coaxial circle on the pressurized surface of a circumferentially clamped plate subject to axisymmetric loading. The understanding of the fracture behavior of a component experiencing such a condition is of particular interest to the aerospace and defense industries where circular plate components are often utilized. In such applications, it is imperative that the designer be able to predict the loading conditions facilitating dynamic fracture. As a step towards solving such problems, the quasi-static analogy is studied. Specifically, the purpose of this research is to examine and model the precise effects a stress raiser will have on the fracture behavior and strength reduction of a circular plate machined from Ultem 1000. Parametric FEM simulations were employed to determine the correlation between notch geometry and the resulting maximum stress and stress distribution in the notch root vicinity. Stress concentration factor (SCF) relationships were developed which characterize the effect individual geometric parameters have on the notch root stresses. Mathematical models were developed to provide the elastic stress concentration factor for any combination of geometric parameters within the range studied. Additionally, the stress distributions along the notch root and ahead of the notch were characterized for a variety of geometric configurations. Test coupons were employed to not only characterize the mechanical behavior of the material, but also characterize the correlation between simple and axisymmetric loading, respectively. The development of a predictive approach for designers of such circular components to be able to accurately determine the fracture behavior of these components was the motivating factor of this study.

Dedications

For my wife, Catherine, whose love makes every day better than the last.

Acknowledgements

I would like to take this time to thank a number of people whose support was integral to the completion of this study. Most importantly, I would like to express my gratitude for my thesis chair, Dr. Ali P. Gordon, whose skillful guidance, wisdom, and energy facilitated the most meaningful learning experiences throughout my undergraduate career. Dr. Gordon's encouragement to strive beyond the classroom and emphasis on professionalism has driven me to participate in numerous academic competitions which have enriched my educational experience and developed essential technical communication skills. Also, Dr. Gordon's passion for research and exploration has motivated me to further my academic endeavors to the graduate level. I would also like to individually thank the graduate research assistants within the Mechanics of Materials Research Group at UCF. Scott Keller mentored me through many of my research challenges and always came through when something had to be finished at the last minute. Calvin Stewart frequently supported me with my numerical methods research and played a key role in the development of codes throughout this study. Lastly, Justin Karl dedicated hours of assistance to ensure proper conduction of mechanical testing and subsequent data interpretation.

I would also like to thank my family whose unconditional love and unwavering support makes all great achievements possible and worthwhile.

Table of Contents

List of Figures

List of Tables

Nomenclature

α	Notch angle
β	Angular location along notch radius
ε_f, ε_y	Elongation for fracture and yield respectively
θ	Angular coordinate in circular plate
ν	Poisson's ratio
ρ	Notch root radius
$\sigma_{\theta\theta}$, σ_{eqv}, σ_{rr}	Hoop, equivalent, and radial stresses, respectively
σ_{uc}, σ_{uf}, σ_{us}, σ_{ut}	Compressive, flexural, shear, and tensile strength, respectively
σ_{0y}, σ_y	0.2% offset yield strength and proportional limit, respectively
$\tau_{r\theta}$, τ_{max}	In-plane shear stress and maximum shear stress, respectively
a	Radius of plate
d	Distance between bottom of plate and tip of v-notch
E_c, E_f, E_t	Compressive, flexural, and tensile modulus, respectively
h	Thickness of plate
K_t	Elastic or theoretical equivalent stress concentration factor

K_{tE}	Elastic or theoretical stress concentration factor for shallow ellipse notch
K_{tH}	Elastic or theoretical stress concentration factor for hyperbolic notch
K_{ts}	Elastic or theoretical shear stress concentration factor
l	Semiaxis of ellipse
q_0	Uniformly applied pressure
r	Radial coordinate of circular plate
r_n	Notch radial location
t	Notch depth
z	Axial coordinate of circular plate

1. Introduction

In the aerospace and defense industries circular plates must be designed to either withstand extreme pressure without fracture or in the case of guided projectiles, fracture in a predictable manner under a specified load. Such a projectile is illustrated in Fig. 1.1. In the case of guided projectiles, a stress raiser is incorporated into the component so that the component will fracture under a specified load and along a desired path. The key microstructural mechanism that confers fracturability is a ductile tearing mode. In most cases, the stress concentration takes the form of a v-shaped notch (i.e., v-notch). Although the geometric dependence of the stress concentration factor (SCF) for the v-notch has been established for uniaxially loaded components (Appl and Koerner, 1969; Noda and Takase, 1999) and components under bending (Leven and Frocht, 1953), the case of the axisymmetrically loaded v-notched plate has yet to be studied. As such, the main motivation behind the current study is to make up for the short comings in this field of study.

To quantify the relationships between notch geometry and the resulting SCFs along the notch root and ahead of the notch, parametric FEA was employed to facilitate the simulation of over ten thousand geometric notch combinations. The state of localized stress in the vicinity of the notch root determined from these simulations was characterized for a wide range of notch geometries. SCFs K_t and K_{ts} were defined which denote the localized increase in equivalent and shear stress due to the presence of the notch, respectively. The relationships between the magnitudes of these SCFs and notch geometry were quantified resulting in mathematical models which provide the SCF for

any geometric notch combination within the studied ranges. Typical SCF behavior was observed with respect to the radius of the notch root, ρ, i.e., notch root radius and the SCF are inversely proportional. It was determined that within the range studied, the notch angle α did not significantly affect the state of stress along the notch root. Similar observations have been made for thin, v-notched beam elements in bending (Leven and Frocht, 1953). With respect to the notch depth, t, it was observed that notches far from mid-plane of the plate (i.e., shallow notches) produced higher SCFs than those close to the mid-plane (i.e., as t/h approaches 0.5). This result is typical for plates in bending because the flexural stresses within a plate are largest at the plate surfaces and decrease to a minimum at the neutral axis (i.e., mid-plane). More novel observations were made with respect to the radial location of the notch r_n, due to the unique stress state within an axisymmetrically loaded clamped circular plate. It was determined that the radial location of the notch had the greatest influence over not only the magnitude of the SCF, but the stress distributions along the notch root and ahead of the notch. Analytical solutions of the stress state throughout an un-notched plate based on elastic theory were used as constitutive models to predict SCF relationships with respect to the radial coordinate for notched plates. Numerous SCF figures were developed which illustrate SCF trends with respect to individual geometric notch parameters. Finite element analysis stress contours are shown for a wide range of notch geometries which depict not only the localized increase in stress, but the relative vicinity within the plate of which the stress concentration is realized. This stress concentration sphere of influence was quantified by comparing stress distributions within notched plates and equivalent un-notched plates.

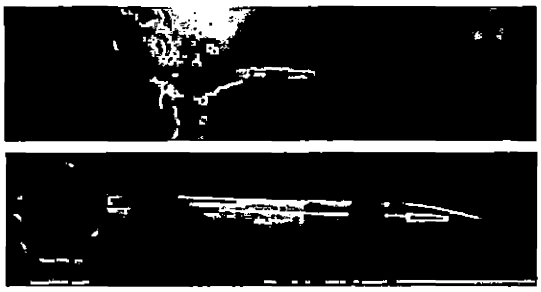

Figure 1.1. Guided projectile utilizing notched circular plate component.

The contents of this thesis continue with a thorough discussion of axisymmetric plate bodies and other background material (Chapter 2). The Ultem 1000 material is discussed in Chapter 3 including material properties, uses throughout various industries, and relevant research findings pertaining to the fracture behavior of Ultem 1000. This section is followed by the experimental approach which details the experimental test procedures employed (Chapter 4). Chapter 5 discusses the results obtained from the experiments, both empirically and through fractography. Immediately following is a discussion on numerical simulations (Chapter 6), which describes the FEM techniques employed to derive relationships between notch geometry and the maximum stresses within the vicinity of the notch. Within the results and discussion section (Chapter 7), data obtained from the parametric FEA is analyzed and stress concentration factor trends are presented along with stress distribution plots for numerous notch geometry configurations. The thesis conclusions are presented in Chapter 8. Numerical simulations, further mechanical testing, and other proposals for future work are reported in Chapter 9. Codes developed throughout the study are found in Appendix A and photographs documenting the fracture surfaces from the experiments are given in Appendix B.

2. Literature Review

2.1 Application

Circular plate components are commonly used in industry applications such as pressure vessel closures, guided projectiles, pump diaphragms, clutches, and turbine disks (Reddy, 1999). The accurate prediction of the stress and strain response to various loading conditions within circular plates is of particular importance to plate component designers. In the majority of applications, circular plate components are designed to withstand static pressure loads subject normal to the plate face without failing, but in specialized cases such as guided projectiles, circular plates are designed to rupture under a specified dynamic load, as shown in Fig. 2.1. Either fracturing prematurely or failing to fracture under the specified load would result in mission failure. To ensure the plate fractures along a desired path, a stress raiser in the form of a v-notch is designed on the plate surface concentric to the plate axis, as shown in Fig. 2.2. The fracture surface of a v-notched Ultem 1000 circular plate is shown in Fig. 2.3. The plate shown in Fig. 2.3 is upside down from the orientation shown in Fig. 2.2.

Although exact solutions exist for the state of stress throughout smooth circular plates (Reddy, 1999) and very accurate approximations have been formulated for stress concentration factors resulting from v-notches for a variety of simple loading conditions (Noda and Takase, 1999), the effects that v-notches have on circular plates under axisymmetric loads have yet to be characterized in literature.

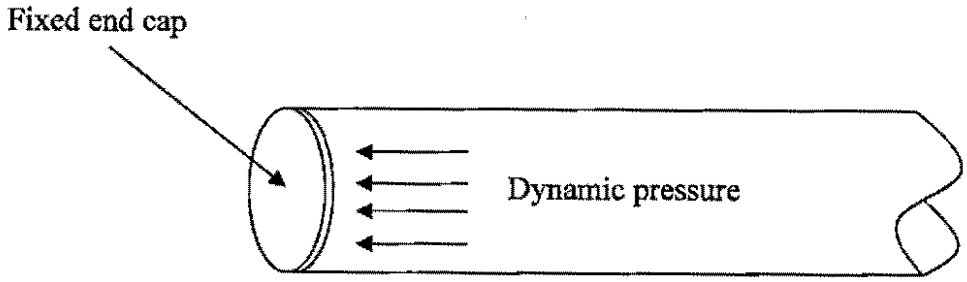

Figure 2.1. Schematic illustrating service loading condition of notched circular plates in guided projectiles.

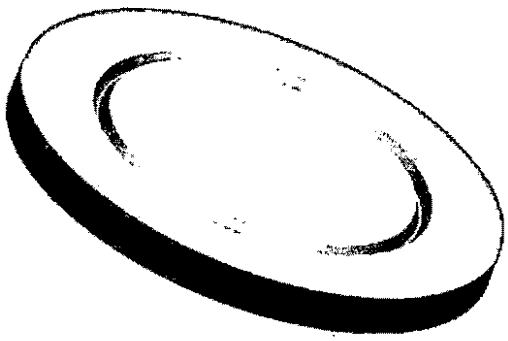

Figure 2.2. V-notched circular plate.

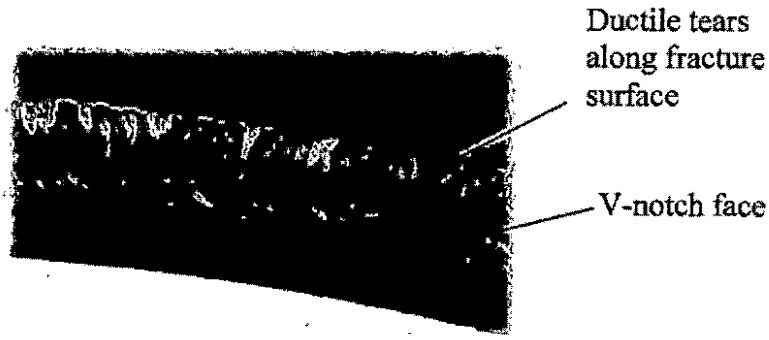

Figure 2.3. Outer ring portion of Ultem 1000 circular plate after fracture along v-notch.

2.2 SCFs and V-Notches

It is often the case that a structural component will contain geometric discontinuities that differentiate the local state of stress from the remote or nominal stress field. Examples of notch shaped stress raisers include shaft shoulders, relief grooves, spring retention grooves, reentrant corners, and notched fatigue test specimens (Pilkey, 1997). The elastic or theoretical stress concentration factor is defined as the ratio between the maximum stress within this annulus local to the notch root to some reference stress (i.e., nominal or remote for a material subjected to nominally elastic conditions). The reference stress chosen depends on the type of stress raiser, component geometry, and loading condition. A comprehensive collection of stress concentration factors for a wide variety of structural components, stress raisers, and loading conditions can be found in the literature (Pilkey, 1997). Stress concentration factor plots for v-notched members in uniaxial tension (Appl and Koerner, 1969) and in bending (Levin and Frocht, 1953) are shown in Fig. 2.3 and Fig. 2.4, respectively.

Classical formulations for theoretical stress concentration factors of deep hyperbolic (K_{tH}) and shallow elliptical notches (K_{tE}) were proposed by Neuber and have proven to provide accurate results for either deep or shallow notches (Neuber, 1958). Also proposed by Neuber (1958) was a relation for the stress concentration factor of notches with arbitrary shapes based on the stress concentration factors of the shallow elliptical and deep hyperbolic notches:

$$K_{tn} = 1 + \sqrt{\frac{(K_{tE}-1)^2(K_{tH}-1)^2}{(K_{tE}-1)^2 + (K_{tH}-1)^2}} \tag{2.1}$$

Here, K_{tE} and K_{tH} are the stress concentration factors of notches with the same geometric notch parameters of the notch under consideration. A set of formulae providing stress concentration factors accurate within 1% for any shape v-notch in a cylindrical test specimen subject to various loading conditions was proposed by Noda and Takase based on numerical results (Noda and Takase, 1999).

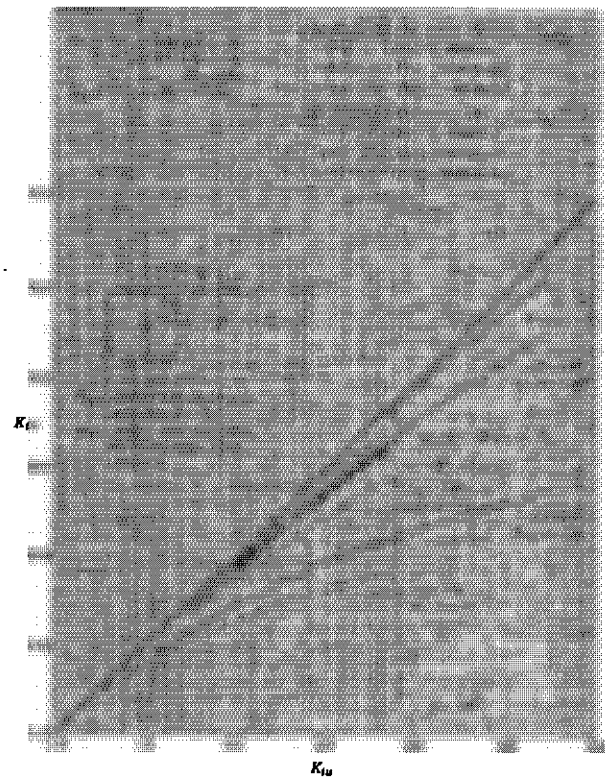

Figure 2.3. Stress concentration factors for a flat tension bar with opposite v-shaped notches.

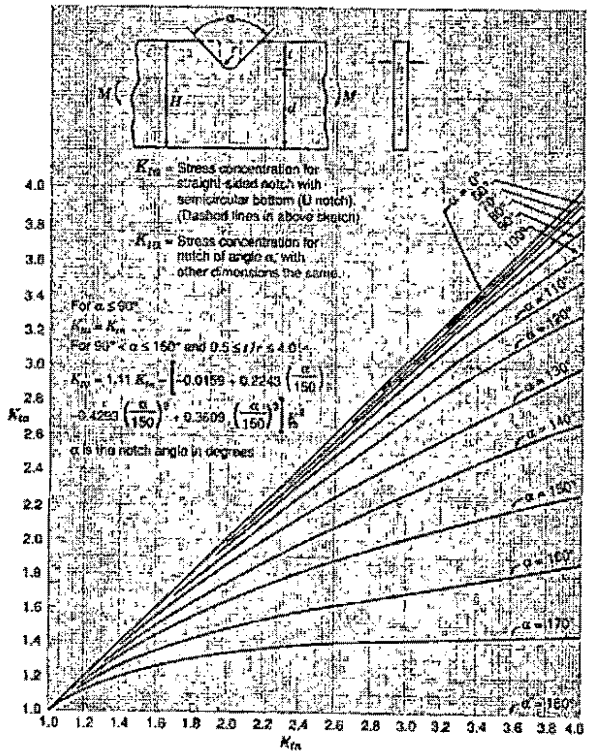

Figure 2.4. Stress concentration factors for a thin beam element in bending with a v-shaped notch.

2.3 Theory of Elasticity for Axisymmetric Plates under Bending

An analytical approach based on the theory of elasticity has been used to determine the state of stress and deformation behavior at any point within a circular plate under a variety of loading conditions and boundary conditions. The general solution for the deflection and stress state was defined by Reddy (1999) for a thin circular clamped plate under a uniformly distributed load, as shown in Fig. 2.5. A circular plate is classified as thin if the thickness does not exceed one-tenth of the diameter. This comparatively small thickness allows for 2D equations to accurately characterize the stresses throughout the plate (e.g. $\sigma_{zz} = 0$). These relations were formulated from the classical elastic Kirchhoff assumptions that lines normal to the mid plane prior to bending remain normal, straight, and in-extensible.

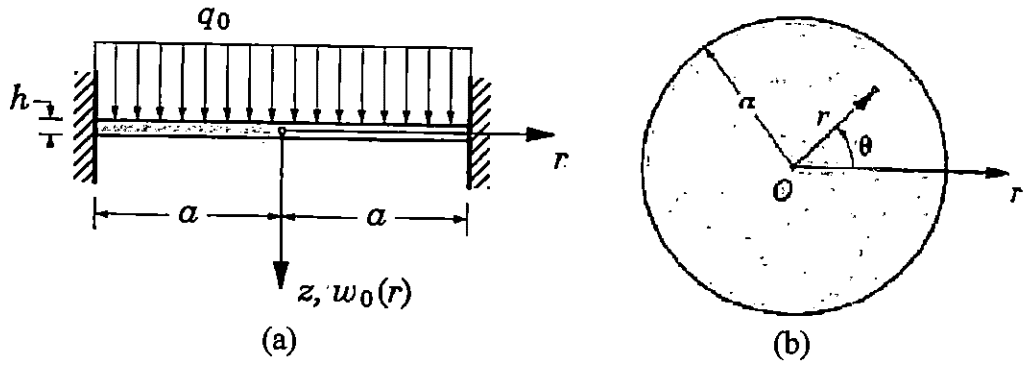

Figure 2.5. Circumferentially clamped plate subject to axisymmetric pressure distribution; (a) cross sectional view, (b) top view (Reddy, 1999).

The derivation of such relations in polar coordinates begins with the general equations for a circular plate subject to an arbitrarily distributed transverse load $q(r)$ applied to the top surface and temperature distribution $\Delta T(r, z)$, i.e.,

$$Dw_0(r) = H(r) + c_2\frac{r^2}{4} + c_4 \tag{2.2}$$

$$D\frac{dw_0}{dr} = H' + c_2\frac{r}{2} \tag{2.3}$$

$$M_{rr} = -\left(H'' + \frac{\nu}{r}H'\right) - \frac{1+\nu}{2}c_2 \tag{2.4}$$

$$M_{\theta\theta} = -\left(\nu H'' + \frac{1}{r}H'\right) - \frac{1+\nu}{2}c_2 \tag{2.5}$$

$$\sigma_{rr} = -\frac{12z}{h^3}\left[\left(H'' + \frac{\nu}{r}H'\right) + \frac{1+\nu}{2}c_2\right] \tag{2.6}$$

$$\sigma_{\theta\theta} = -\frac{12z}{h^3}\left[\left(\nu H'' + \frac{1}{r}H'\right) + \frac{1+\nu}{2}c_2\right] \tag{2.7}$$

Here, w_0 is the plate deflection and M_{rr}, σ_{rr}, $M_{\theta\theta}$, and $\sigma_{\theta\theta}$, are the radial and tangential components of the bending moments and stresses, respectively. In the above equations, r

is the radial coordinate of the plate, z is the axial coordinate of the plate, v is the Poisson's ratio, c_2 and c_4 are constants determined from boundary conditions, and D is the flexural rigidity of the plate which is expressed

$$D = \frac{Eh^3}{12(1-v^2)} \tag{2.8}$$

where h is the thickness of the plate and E is the modulus of elasticity (Timoshenko, 1961; Wang, 2004). The function H is defined

$$H = F - G \tag{2.9}$$

where functions F and G are written

$$F(r) = \int \frac{1}{r} \int r \int \frac{1}{r} \int r\, q(r) dr dr dr dr \tag{2.10}$$

$$G(r) = \frac{1}{(1-v)} \int \frac{1}{r} \int r\, M_T dr dr \tag{2.11}$$

and the thermal moment M_T is expressed

$$M_T = E\alpha \int_{-\frac{h}{2}}^{\frac{h}{2}} \Delta T\,(r,z) z dz \tag{2.12}$$

Here, α is the coefficient of thermal expansion and ΔT is the temperature gradient. For the case of circumferentially clamped plates subjected to an isothermal axisymmetric pressure, the boundary conditions require fixed conditions at the circumference of the plate (i.e., $w_0 = 0$ and $dw_0/dr = 0$ at $r = a$). From these boundary conditions and from Eqs. 2.2 and 2.3, the constants c_2 and c_4 can be solved for and are expressed

$$c_2 = -\frac{q_0 a^2}{8}, \quad c_4 = \frac{q_0 a^2}{64} \tag{2.13}$$

where q_0 is the uniformly distributed load and a is the radius of the plate. From Eqn. 2.2, the deflection of the midsection of the plate as a function of radius is given as

$$w_0(r) = \frac{q_0 a^4}{64D}\left(1 - \frac{r^2}{a^2}\right)^2 \tag{2.14}$$

The maximum deflection is found at the center of the plate, i.e,

$$w_{max} = \frac{q_0 a^4}{64D} \tag{2.15}$$

The bending moments are a function of the radial coordinate only and from Eqs. 2.4 and 2.5 are expressed as

$$M_{rr}(r) = \frac{q_0 a^2}{16}\left[(1+v) - (3+v)\frac{r^2}{a^2}\right] \tag{2.16}$$

$$M_{\theta\theta}(r) = \frac{q_0 a^2}{16}\left[(1+v) - (1+3v)\frac{r^2}{a^2}\right] \tag{2.17}$$

The maximum magnitude of the moments are realized at the circumferential edge and are expressed

$$M_{rr}(a) = -\frac{q_0 a^2}{8} \tag{2.18}$$

$$M_{\theta\theta}(a) = -\frac{v q_0 a^2}{8} \tag{2.19}$$

The out of plane bending moment M_{rr} and the in plane bending moment $M_{\theta\theta}$ are shown graphically as a function of the radial coordinate in Fig. 2.6.

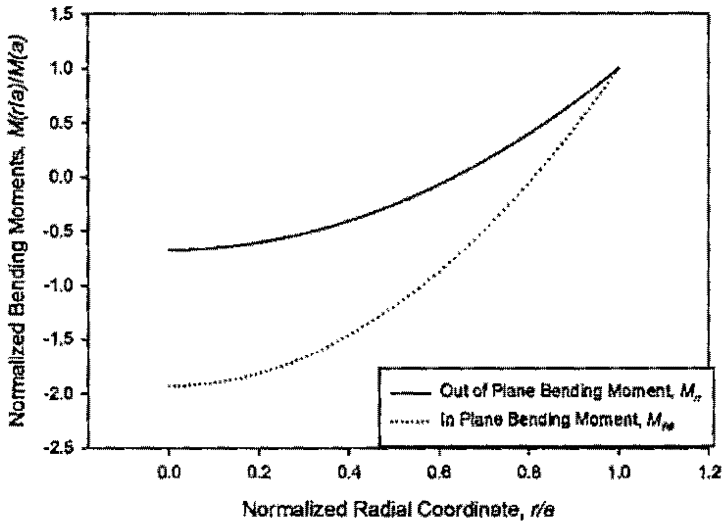

Figure 2.6. In-plane and out-of-plane bending moments throughout circular plate.

From the solution of Eqs. 2.6 and 2.7, the radial stress σ_{rr} and the tangential stress $\sigma_{\theta\theta}$ can be expressed in polar coordinates, i.e.,

$$\sigma_{rr}(r,z) = \frac{3q_0a^2z}{4h^3}\left[(1+v) - (3+v)\frac{r^2}{a^2}\right] \tag{2.20}$$

and

$$\sigma_{\theta\theta}(r,z) = \frac{3q_0a^2z}{4h^3}\left[(1+v) - (1+3v)\frac{r^2}{a^2}\right] \tag{2.21}$$

Similar to simple beam problems, the flexural stresses are zero at the neutral axis (z = 0); however, unlike typical beam problems, the stress distribution elsewhere is a function of material properties. The radial and tangential components of stress are illustrated on a differential element in Fig 2.7.

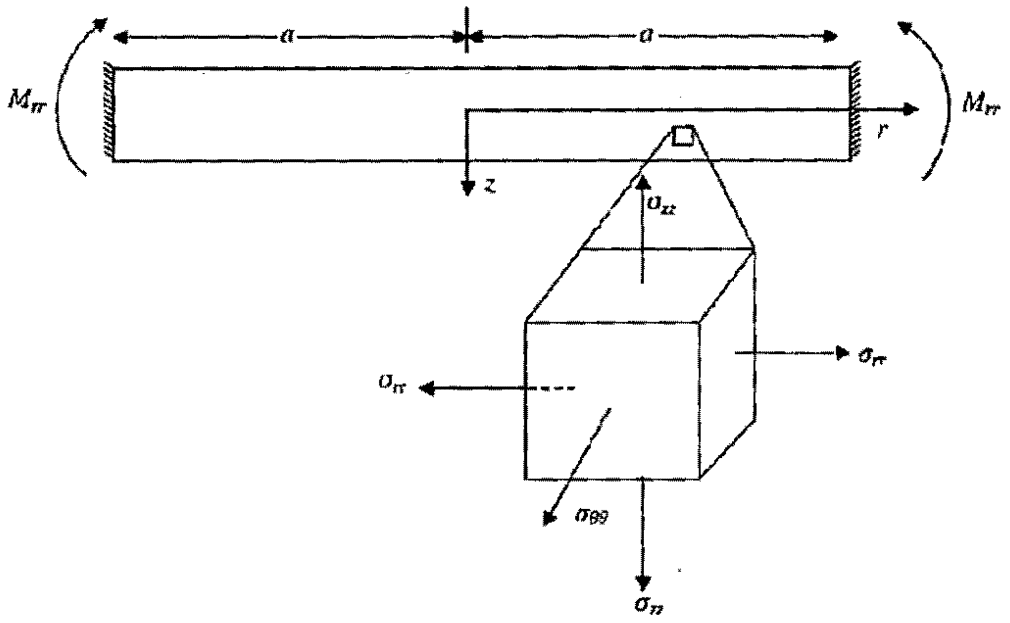

Figure 2.7. Radial and tangential components of stress on a differential element of circular plate.

The maximum stress is found at the clamped boundary on the top surface of the plate and is given

$$\sigma_{rr}\left(a,-\frac{h}{2}\right)=-\frac{6M_{rr}(a)}{h^2}=\frac{3q_0}{4}\left(\frac{a}{h}\right)^2 \tag{2.22}$$

Under plane stress conditions, from Eqs. 2.20 and 2.21, the effective stress throughout the plate can be obtained, i.e.,

$$\sigma_{eqv}=\frac{1}{\sqrt{2}}\sqrt{(\sigma_{rr}-\sigma_{\theta\theta})^2+(\sigma_{rr})^2+(\sigma_{\theta\theta})^2} \tag{2.23}$$

The radial, tangential, and equivalent stresses as a function of the radial coordinate are shown in Fig. 2.8 for a normalized axial location z/h = -0.20. The theoretical stresses at this particular plate depth are shown because this depth corresponds to the benchmark v-

notch depth chosen for this study and a comparison of the stresses between the benchmark smooth plate and the benchmark notched will be discussed in Chapter 6.

Solutions to a variety of cases with various boundary conditions and load states derived from Kirchhoff plate theory can be found in the literature (Szilard, 1974; Ugural, 1999; Reddy, 1999). More specifically, the boundary conditions which have been previously investigated include simply supported edges, clamped edges, and elastic foundations. Additionally, plates subject to uniform and non-uniform pressure distributions as well as point loads and thermal loads have been studied.

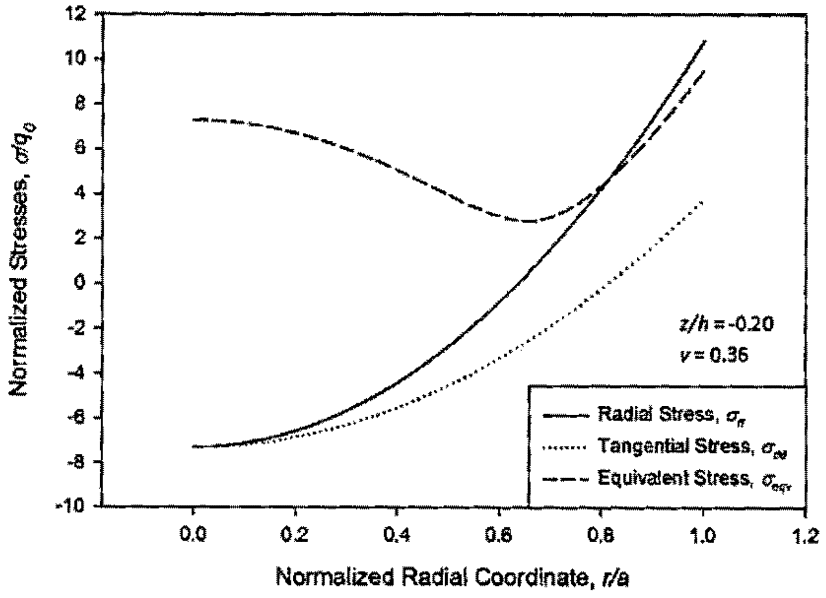

Figure 2.8. Radial, tangential, and equivalent stresses at an axial location z/h equal to -0.20.

3. Materials

Polyetherimide, also referred to as Ultem, is a widely-used amorphous thermoplastic with applications ranging from the aerospace to medical industries. Ultem is extensively used in the aerospace and defense industries due to its high strength, heat resistance, and relatively low-weight compared to aluminum alloys. The mechanical, physical, and thermal properties of Ultem, shown in Table 1, allow for such versatility in a wide variety of industry applications. For example, Ultem was used to injection mold a variety of interior and structural components in the Fokker 50 and 100 series aircraft (Savage, 1988). Also, because of the remarkable resistance to corrosive cleaning chemicals and thermal cycling it displays, Ultem was chosen for sterilization trays and surgical probes that withstand daily autoclaving (Johnson, 1998).

The mechanical properties of Ultem and similar plastics at various temperatures and strain rates have been extensively studied by various researchers. It was found that, generally, an increase in strain rate corresponds to an increase in tensile strength among Ultem and similar thermoplastics (Schobig et al., 2008). Similar results were reported by Bordonaro and Krempl (1993) when cylindrical plastic specimens were tensile tested at various strain rates, ranging from 10^{-3} to 10^{-6} s^{-1}. The temperature effects on the stress-strain relationships of Ultem were studied by Pecht and Wu (1994). They observed that increases in temperature cause a decrease in the yield strength and modulus of elasticity of Ultem while an increase in strain rate causes an increase in tensile strength. These observations are depicted graphically in Fig. 3.1. Pecht and Wu (1994) also investigated temperature effects on two other polymers, Kapton and SE45, and found that the lower

glass transition temperature of Ultem can be attributed to the ether and imide linkages present in Ultem. The chemical structure of Ultem 1000 can be found in Fig. 3.2 (Pecht and Wu, 1994).

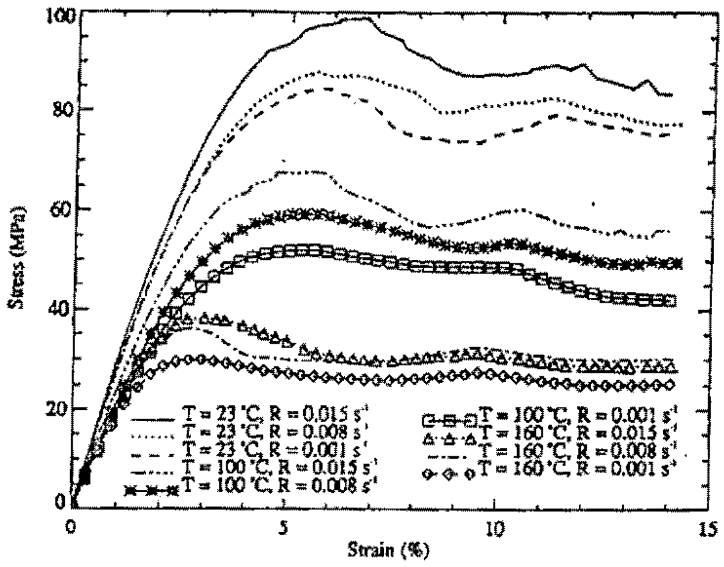

Figure 3.1. Stress-strain curves corresponding to Ultem tensile tests under various temperatures and strain rates (Pecht and Wu, 1994).

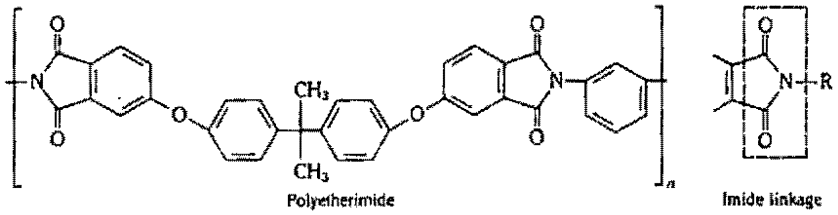

Figure 3.2. Chemical composition of Ultem 1000 (Pecht and Wu, 1994).

The fracture behavior of Ultem has been studied under a wide range of temperatures by Kim and Ye (2004). They employed mechanical tests on compact tension (CT) specimens of various thicknesses at a crosshead speed of 2 mm/min subject

to various temperatures (24°C, 80°C, 130°C) to determine the relationship between temperature and plane strain fracture toughness. They observed three different crack propagation modes, namely unstable, stable and mixed, depending on the temperature and specimen thickness. It was found that at room temperature, all the specimens exhibited brittle fracture and ductile fracture was observed in specimens at higher temperatures. These results are shown in Fig. 3.3.

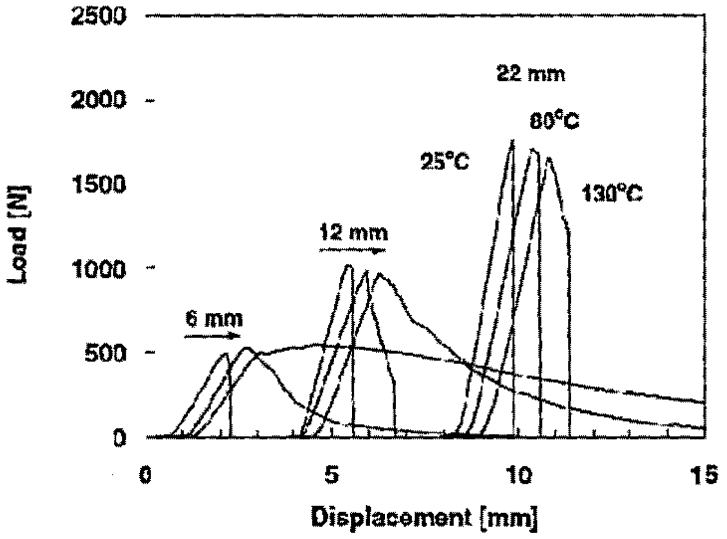

Figure 3.3. Load displacement curves for Ultem CT specimens of various thicknesses (6, 12, and 22 mm) and various temperatures (Kim and Ye, 2004).

Other standard mechanical, thermal, and electrical properties of Ultem have been well characterized and can be found in the literature along with many experiments concerning fatigue, creep, and wear behaviors (Stokes, 1988; Bijwe et al., 1991; Tou and Zihui, 2007; Facca et al., 2007; Smmazcelik, 2008). A variety of Ultem grades are available from SABIC Innovative Plastics which encompass a large range of mechanical, thermal, and chemical properties. For example, Ultem grades are available with glass

fiber or PTFE fillings of up to 45% which increases strength and enhances flow properties. A number of other enhancements are available such as transparency characteristics and finish properties which allow for safe use in the medical and food handling industries. The specific grade of resin chosen for the present study is Ultem 1000 which is unfilled, transparent, and exhibits standard flow characteristics.

Table 3.1. Various properties of Ultem 1000 (SABIC Innovative Plastics).

Mechanical Properties	**Value (English)**	**Value (SI)**
Tensile Modulus, E_t	475 ksi	3.28 GPa
Compressive Modulus, E_c	480 ksi	3.31 GPa
Flexural Modulus, E_f	500 ksi	3.45 GPa
Poisson's Ratio, ν	0.36	-
Elongation (Yield), ε_y	7.0 %	-
Tensile Strength, σ_{ut}	16.5 ksi	113.8 MPa
Compressive Strength, σ_{uc}	22 ksi	151.7 MPa
Shear Strength, σ_{su}	15 ksi	103.4 MPa
Flexural Strength, σ_{uf}	20 ksi	137.9 MPa
Elongation (Fracture), ε_f	60 %	-
Izod Impact Strength, Notched	1.0 ft-lbs/in	0.034 J/m
Rockwell Hardness	109 ("M" Scale)	-
Physical Properties	**Value (English)**	**Value (SI)**
Specific Gravity	1.28	-
Thermal Properties	**Value (English)**	**Value (SI)**
CLTE - Flow, α_f	0.000031 in/in/°F	-
CLTE - Tansverse, α_t	0.000030 in/in/°F	-

4. Experimental Approach

Uniaxial tensile tests were employed on smooth Ultem 1000 cylindrical coupons to determine the tensile properties of Ultem 1000 at room temperature and to investigate the failure behavior of Ultem 1000 under uniaxial tension. Experiments were also conducted on two sets of cylindrical notched specimens with different notch root radii to determine the effects of v-notch stress concentrations on the strength and fracture properties of Ultem 1000. The root radii for the v-notched specimens were 0.035 (ρ/t = 0.23) and 0.016 (ρ/t = 0.11) inches, respectively. The test coupons were machined from extruded Ultem 1000 rod stock with a diameter of 0.5 inches. Tensile tests were conducted until rupture at three cross head displacement rates, 0.5 mm/s, 0.05 mm/s, and 0.005 mm/s to characterize any mechanical property rate dependency. An MTS 100 kN servohydraulic testing frame was used along with an MTS 632-53E-14 extensometer to conduct the experiments and collect strain data, respectively. The three specimen configurations used and the extensometer experimental setup are shown in Fig. 4.1 and Fig. 4.2, respectively. The specimen conditioning and experimental procedure were carried out in accordance with ASTM D638-08, under normal laboratory conditions with an ambient temperature of 74°F and 50% humidity. The standard calls for at least five tests to be conducted for each experimental configuration, but due to available resources, only one experiment was performed per specimen type and strain rate.

The fracture surfaces of the tensile test specimens were examined using a Hitachi S-3500N scanning electron microscope (SEM) to gain insight into the microstructural mechanics facilitating fracture. Due to the non-conductivity of Ultem 1000, the fracture

surfaces were sputter coated with platinum to prevent a built up of static charge on the fracture surface and to increase the signal resolution.

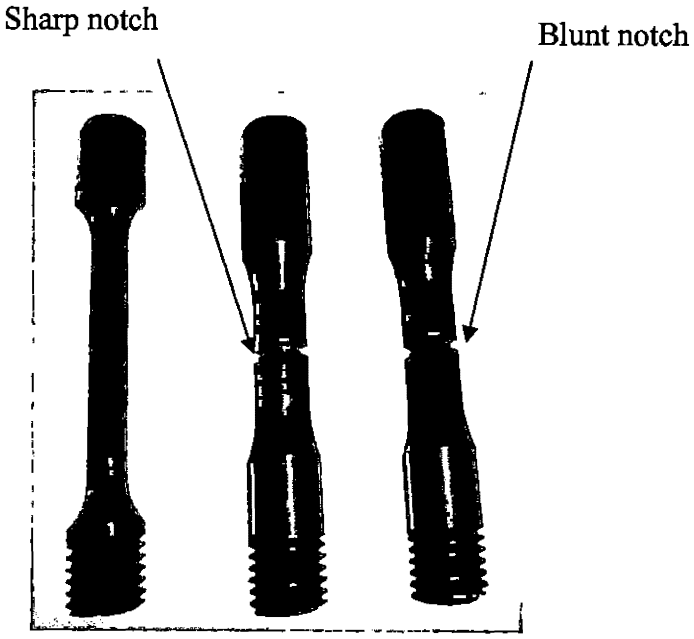

Figure 4.1. Tensile specimen configurations used.

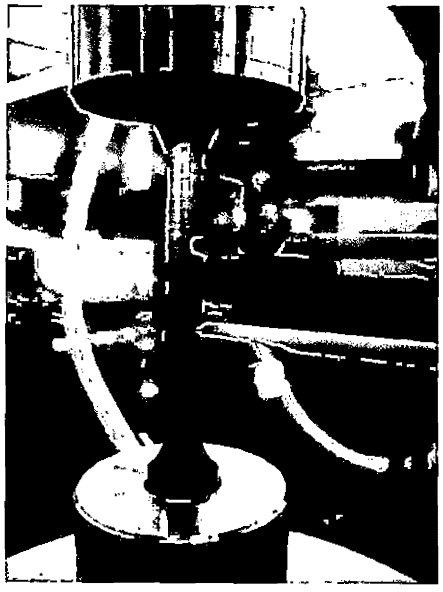

Figure 4.2. Extensometer application.

5. Experimental Results

Mechanical properties of Ultem 1000 under uniaxial tension such as the modulus of elasticity, E, the ultimate tensile strength, σ_{ut}, the fracture strain, ε_f, and the 0.2% offset yield strength, σ_{oy}, were determined from the stress-strain curves of the un-notched specimens. These values were also calculated for both notched cases; however, it should be noted that the values between the notched and un-notched cases cannot be directly compared and that the data for the notched cases is given for the sake of establishing a complete record. Table 5.1 summarizes the data determined from the tensile tests of the un-notched and notched specimens. The values of the modulus of elasticity and the ultimate tensile strength from the smooth specimen experiments match closely to those previously published (See Table 3.1). A rate dependency of the ultimate strength and the yield strength for the smooth case is observed from the stress-strain diagram, as shown in Fig. 5.1, where the ultimate and yield strength increase with strain rate. The observation of an increase in yield strength with an increase in strain rate is consistent with the Eyring theory of yield (Swallowe, 1999), described by the following relation:

$$\sigma_y = \sigma_0 + \frac{RT}{\nu}\log\left(\frac{2\dot{\varepsilon}}{\dot{\varepsilon}_0}\right) \tag{5.1}$$

Here, σ_y is the yield stress, $\dot{\varepsilon}$ is the strain rate, T is the temperature, and $\dot{\varepsilon}_0$, ν, σ_0, and R are regression constants. The relationship between strain rate and the ultimate tensile strength has been observed previously by Krempl (1993) for Ultem 1000 and other thermoplastics. These results suggest that a high strain rate facilitates a more brittle material response than a low strain rate for un-notched tensile experiments.

Table 5.1 Summary of mechanical properties from the notched and un-notched tensile tests.

	Rate (mm/s)	E (GPa)	ε_f (mm/mm)	σ_f (UTS) (MPa)	P_{max} (N)	σ_y (0.2%) (MPa
Un-notched	0.5	3.51	0.0510	111.5	3535	65.4
	0.05	3.22	0.0583	110.0	3487	64.0
	0.005	3.57	0.0541	104.0	3297	58.7
Blunt Notch ($K_t = 2.0$)	0.5	5.74	0.0193	101.9	3230	N/A
	0.05	5.54	0.0245	119.6	3791	108.9
	0.005	5.17	0.0253	113.0	3582	98.3
Sharp Notch ($K_t = 3.0$)	0.5	5.10	0.0219	105.2	3335	N/A
	0.05	5.61	0.0199	99.3	3148	N/A

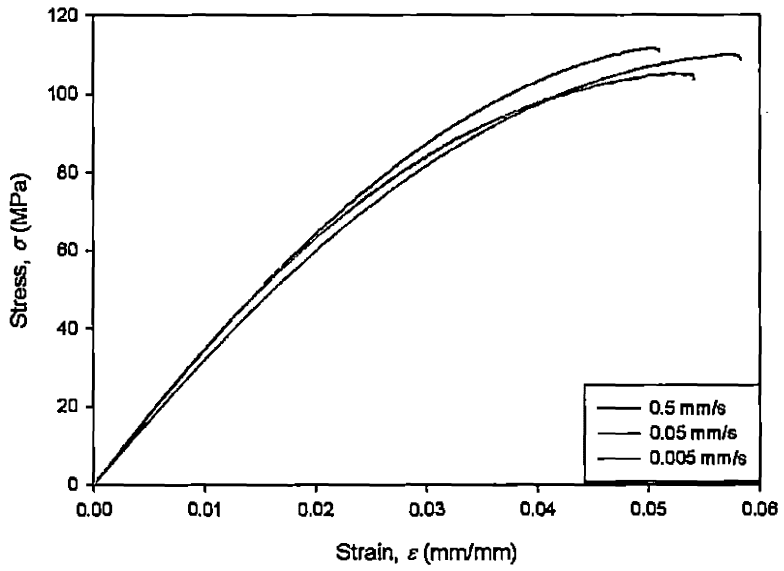

Figure 5.1. Engineering stress-strain curve for smooth specimens.

These trends are based on data from only a single experiment at each configuration and therefore can be easily skewed by experimental error such as machining defects in the test specimens.

The experimental results from the notched tensile tests provide insight into the effects of a stress concentration on the fracture behavior of uniaxially loaded Ultem 1000. In general, the presence of a v-notch facilitated brittle fracture behavior, which is evidenced by the lack of a yield region on a force-strain diagram for the notched cases, as shown in Fig. 5.2.

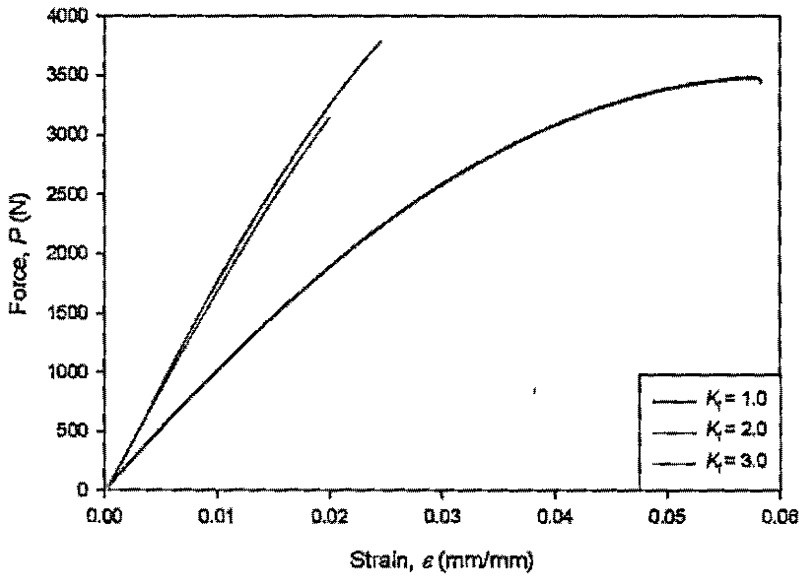

Figure 5.2. Force-strain diagram comparing smooth and notched specimens for tensile experiment at 0.05 mm/s.

The theoretical stress concentration factors for the notches used in these tensile experiments were calculated from empirical relationships provided by Noda and Takase (1999) which are functions of notch geometry and provide a $K_t = 2.0$ for $\rho/t = 0.23$ and $K_t = 3.0$ for $\rho/t = 0.11$. From Fig. 5.2, it should be observed that higher stress concentration

factors facilitate fracture at lower strains than for lower stress concentration factors and un-notched specimens. Another trend apparent in Fig. 5.2 is that the modulus of elasticity increases with the stress concentration factor. An increase in the stiffness of a material is often associated with brittle behavior and in this case could be a result of heat imparted onto the material in the vicinity of the notch during machining.

In addition to an analysis of the stress-strain responses, fractography was employed to explore the effects of strain rate and the presence of a v-notch on the fracture behavior of uniaxially loaded Ultem 1000 specimens. Examination of the fracture surfaces with optical microscopy and a SEM provides knowledge of the modes of fracture present as well as the crack initiation location. For the smooth case, the effect of strain rate on the failure mode, either ductile or brittle, is readily observed from the fracture surfaces. A comparison between the relatively smooth fracture surfaces of a specimen tested at 0.5 mm/s, shown in Fig. 5.3, and the rough fracture surface of a specimen tested at 0.005 mm/s, shown in Fig. 5.4, illustrates the strain rate effect. Detailed photographs of all the smooth tensile specimens tested, including side shots and SEM photographs can be found in Appendix B.

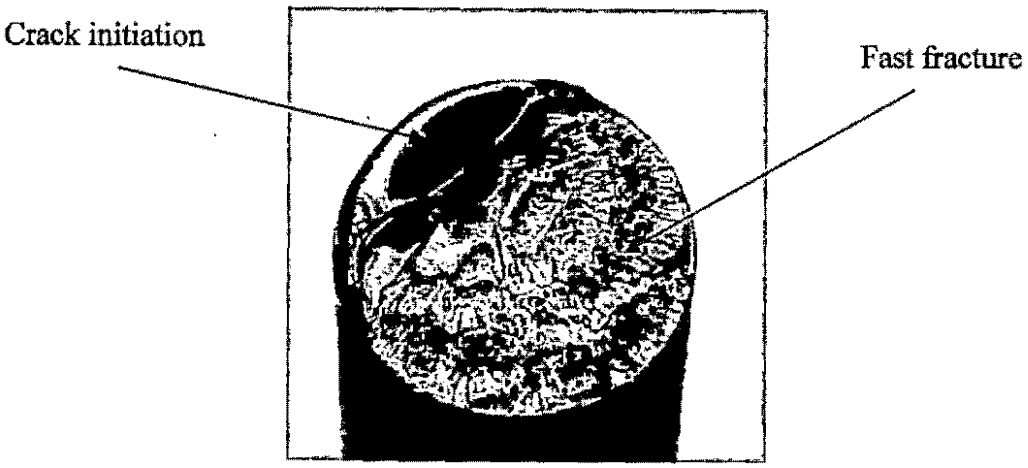

Figure 5.3. Fracture surface of a smooth tensile specimen tested at 0.5 mm/s.

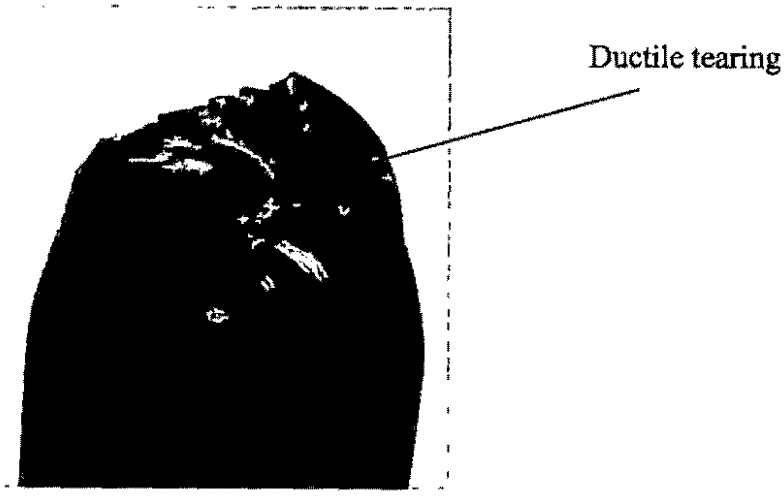

Figure 5.4. Fracture surface of a smooth tensile specimen tested at 0.005 mm/s.

For the notched cases, analysis of the fracture surfaces evidence brittle fracture behavior, supporting the conclusions drawn from the force-strain curves for the notched specimens. The fractography of the notched specimens focused on two areas of interest, the assumed crack initiation point and smooth circumferential bands near the edges of the specimen. The fracture initiation point was determined by tracing radial fracture

propagation paths back to a location of relatively smooth surface. This smooth initiation region is caused by relatively slow fracture speeds where adjacent fibers fracture all on the same plane (Greenhalgh, 2009). From this point, the crack propagates radially with increasing velocities, causing fracture to occur on multiple planes, which facilitates the formation of a rough surface. The evolution of the surface topology is typically divided into three distinct zones; the mirror, mist, and hackle (Greenhalgh, 2009). Figure 5.5 illustrates the crack initiation point, radial propagation lines, and these three zones.

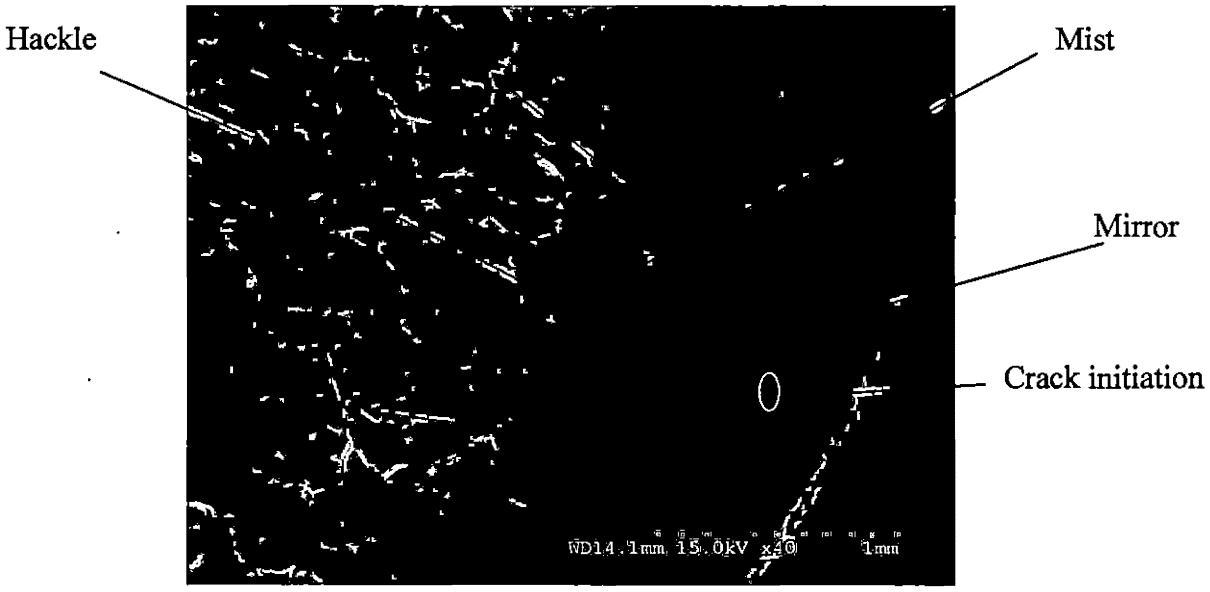

Figure 5.5. SEM fractograph showing crack initiation of blunt notched specimen tested at 0.05 mm/s.

The thicknesses of the smooth circumferential bands observed in all of the notched fracture surfaces were measured to determine if the thickness of the band was a function of strain rate, and are summarized in Table 5.2. An example of these bands is shown on the fracture surface of a blunt notched specimen tested at 0.005 mm/s, depicted in Fig. 5.6. From the data in Table 5.1, it appears that the thickness of the bands increase with

decreasing strain rate for the blunt notched specimen; however, this trend could be an artifact of the few data points recorded.

Table 5.2 Average smooth circumferential band thicknesses for different strain rates.

	Displacement rate (mm/s)	Band thickness (μm)
Blunt Notch (K_t = 2.0)	0.5	250
	0.05	330
	0.005	400
Sharp Notch (K_t = 3.0)	0.5	400
	0.05	200

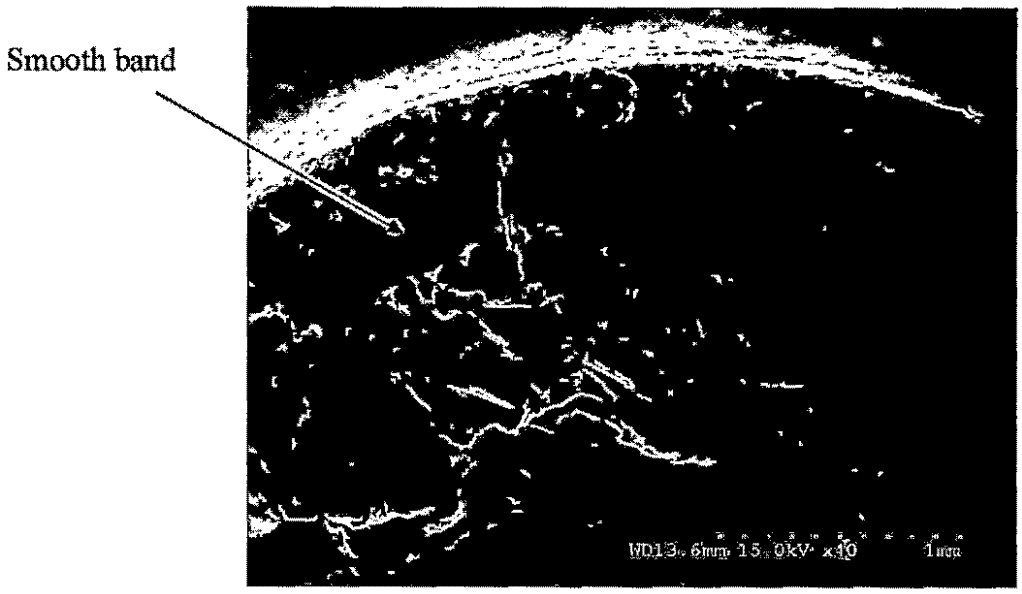

Figure 5.6. SEM fractograph showing smooth band of blunt notched specimen tested at 0.005 mm/s.

Multiple fractographs of each of the specimens tested, detailing the fracture surface and circumferential bands are providing in Appendix B.

6. Numerical Simulation Approach

Because of the versatility and efficiency of such numerical methods, finite element analysis was used to investigate the effects that notch geometry have on the maximum stress on the surface and in the vicinity of a v-notch root on an axisymmetrically loaded plate. Through the use of parametric codes, results from thousands of combinations of notch geometries can be used to formulate numerical relationships not feasible with traditional mechanical testing or elastic theory. The ANSYS general-purpose software was used to numerically simulate the stress, strain, and displacement fields of the component.

Taking advantage of the axisymmetric geometry of the model, only a 2D cross section was required to accurately simulate the component, as shown in Fig. 6.1. Boundary conditions restricting displacement in the radial and axial directions were placed on the circumferential boundary of the plate. The appropriate displacement boundary conditions are automatically imposed by ANSYS on the axial edge of the model in an axisymmetric simulation. The top surface of the plate was subjected to a uniformly distributed static pressure, q_0. As shown in Fig. 6.1, no portion of the distributed load was applied to the notch faces or root; however, cases where a fraction of q_0 are carried across the notch would reflect the service conditions more accurately, but is saved for future research.

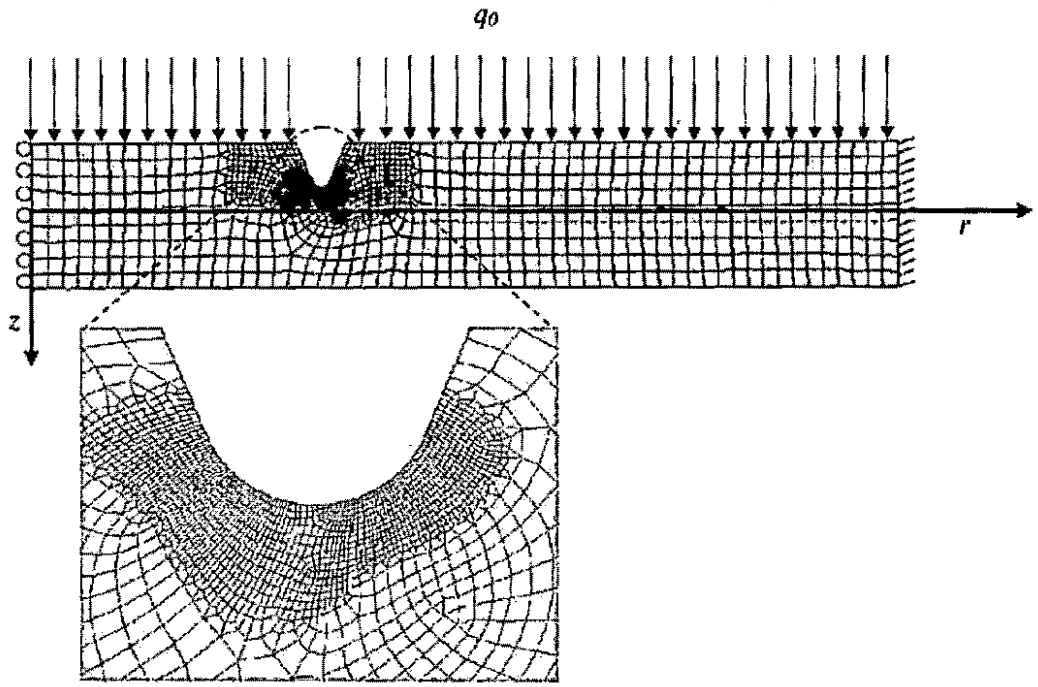

Figure 6.1. Automatic mesh and refinement in vicinity of notch for benchmark geometry.

An ANSYS input file, provided in Appendix A, was developed to facilitate versatile parametric runs with highly customizable user control. The geometry of the plate component was parametrically related to the dimensions and location of the notch. The range and increments of specific variables could be easily manipulated for a variety of custom parametric simulations. The normalized ranges of the geometric notch parameters were chosen to encompass the broadest feasible range of geometric combinations within the limits set by typical component machining and accurate FEA solutions. More specifically, very sharp notch radii ($\rho/t \leq 0.20$) were not considered because such notches would be difficult and expensive to machine and the accuracy of the FEA solutions for very sharp discontinuities are decreased. The geometric notch parameter ranges and corresponding increments are given in Table 6.1.

Table 6.1. Ranges and increments of geometric v-notch parameters simulated.

r_n/a	t/h	ρ/t	α
0.17	0.20	0.13	40°
0.24	0.24	0.15	45°
0.30	0.28	0.17	50°
0.37	0.32	0.19	55°
0.43	0.36	0.21	60°
0.50	0.40	0.23	65°
0.57	0.44	0.25	70°
0.63	0.48	0.27	75°
0.70	0.52	0.29	80°
0.76	0.56	0.31	85°
0.83	0.60	0.33	90°

Limiting cases such as

$$r_n/a \rightarrow 0,\ r_n/a \rightarrow 1.0,\ t/h \rightarrow 1.0,\ \rho/t \rightarrow 0,\ \alpha \rightarrow 0°, \tag{6.1}$$

and so on were left for future study. The one exception was that the smooth case was investigated (i.e., r_n/a is undefined, $t = 0$, and ρ is undefined). The plate radius, a, and thickness, h, were held constant for all simulations. The benchmark notch geometry consists of the following normalized parameters:

$$r_n/a = 0.33,\ t/h = 0.20,\ \rho/t = 0.23,\ \alpha = 60° \tag{6.2}$$

The characterizing geometric parameters of the v-notch and circular plate are shown in Fig. 6.2.

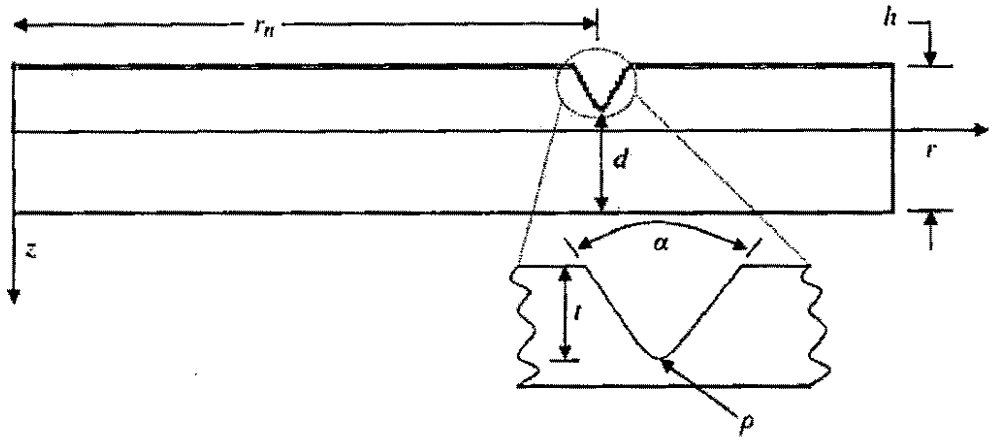

Figure 6.2. Characterizing geometric parameters for v-notched plate.

The FEA model is meshed entirely with PLANE82 8-noded quadrilateral elements. This element was chosen for its ability to tolerate irregular shapes in automatic meshes without much loss in accuracy. The ANSYS automatic meshing algorithm was employed in the parametric simulations for efficient mesh adaptation to the varying notch dimensions. Finite element modeling meshes for some of the extreme geometric combinations such as a shallow notch, deep notch, and sharp notch are shown in Figs. 6.3 - 6.4. Automatic mesh refinement in the vicinity of the notch was utilized which reduced the area of the elements at the notch tip by approximately a factor of two thousand from those in remote regions of the plate. The ratio of the average notch tip element side length to the benchmark normalized notch tip radius ρ/t is 0.0048. Mesh refinement, illustrated in Fig. 6.1, consisted of element cleaning and smoothing in addition to size reduction. The average number of elements and nodes utilized in the parametric runs

were 2,700 and 8,400 respectively. The component is subjected to quasi-static loading and the materials assumed to behave elastically (See Table 3.1). To ensure that the results can be compared with future elastic-plastic studies, q_0 is designed to impart states of stress that do not exceed the yield strength of Ultem 1000.

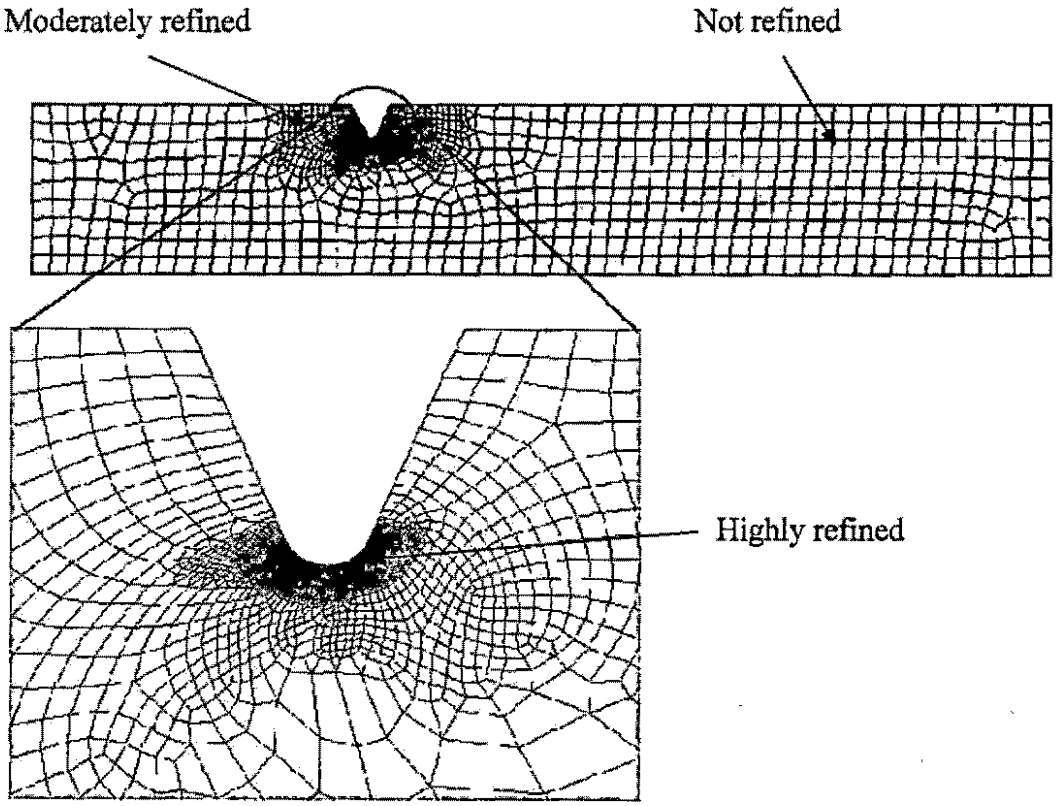

Figure 6.3. Automatic mesh generated for a shallow notch ($t/h = 0.20$) with otherwise benchmark parameters.

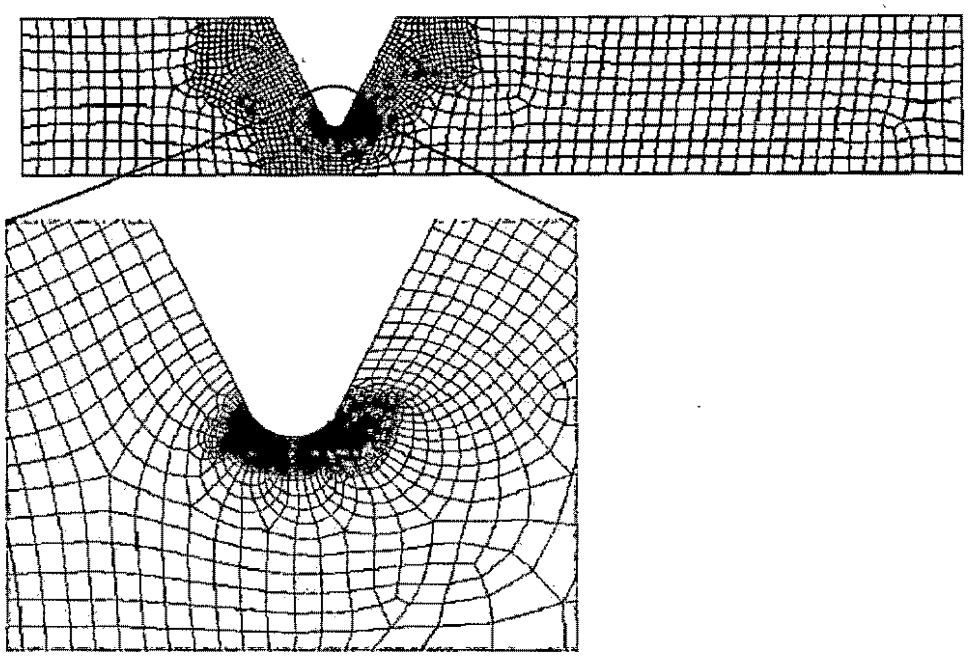

Figure 6.4. Automatic mesh generated for deep notch ($t/h = 0.60$) with otherwise benchmark parameters.

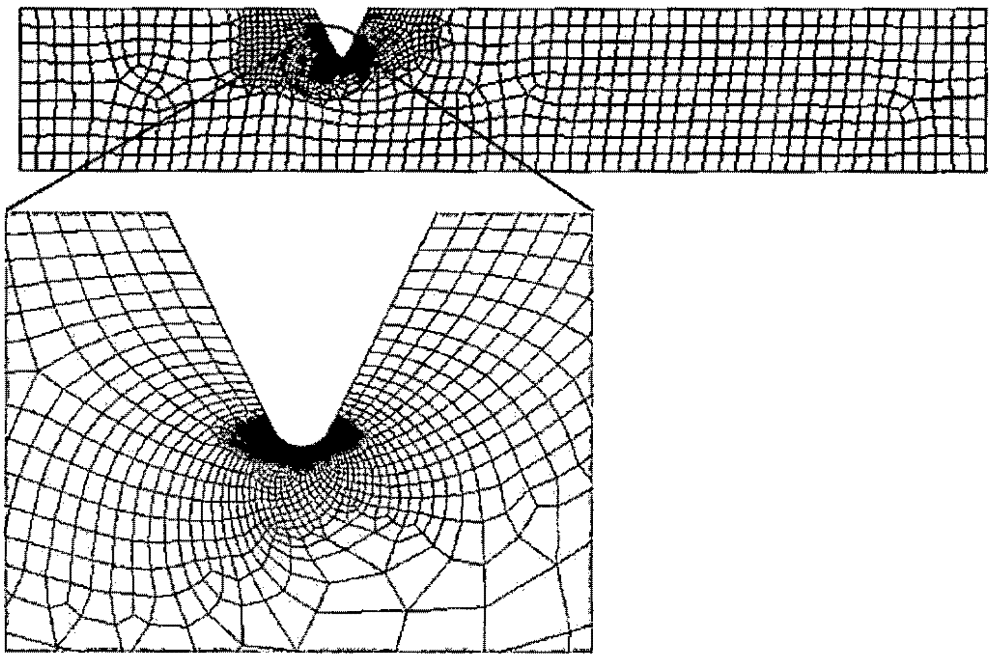

Figure 6.5. Automatic mesh generated for sharp notch ($\rho/t = 0.20$) with otherwise benchmark parameters.

7. Results and Discussion

The discussion of the numerical simulation results are divided into an analysis of elastic stress concentration factors with respect to notch geometry and an investigation of the effects notch geometry has on stress distributions at the notch root. The former is subdivided into individual detailed discussions for each geometric notch parameter supplemented with stress concentration factor plots and curve fit equations. The stress distribution portion of the discussion provides insights into the angular stress distributions along the surface of the notch as well as vertical stress distributions ahead of the notch supported by stress distribution plots and FEA images.

To verify the accuracy of the FEM, the un-notched plate was simulated and the equivalent stresses σ_{eqv} and maximum shear stresses τ_{max} were compared to those obtained from analytical solutions and are shown graphically in Fig. 7.1 and 7.2, respectively.

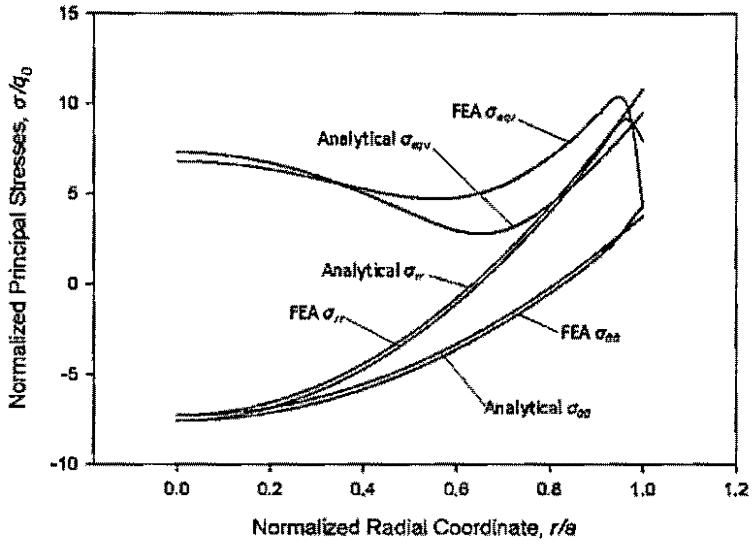

Figure 7.1. Comparison between the equivalent stresses obtained from the FEA and analytical solutions.

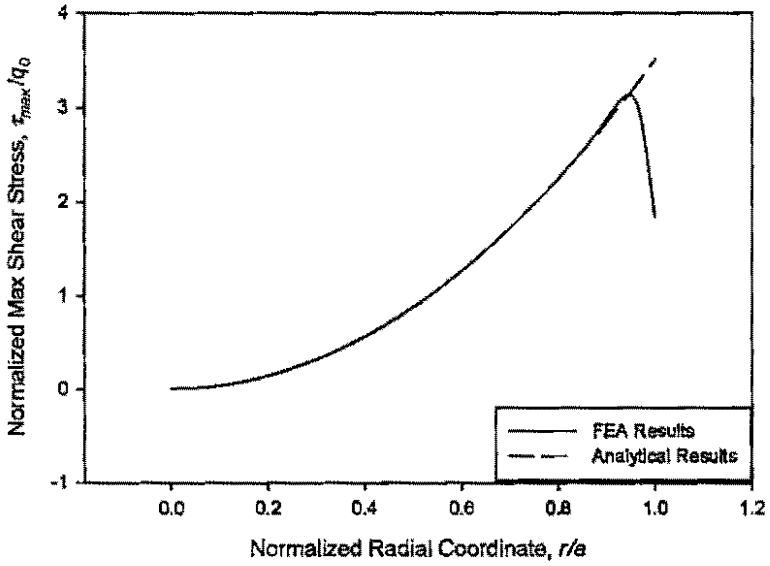

Figure 7.2. Comparison between the max shear stresses obtained from the FEA and analytical solutions.

From these plots, it is shown that the results from the FEA match closely to those obtained from the analytical solutions for the principal stresses; however, there is a deviation between the analytical and numerical results of the equivalent stress. This is due to the assumption made in the analytical solution that there are no stresses in the axial direction This assumption, however, is not made in the FEA and axial stresses are present in the finite element solution. These axial stresses contributed to the equivalent stress value in the FEM and thereby result in a deviation from the analytical solution.

The stress concentration factor, K_t is defined as the equivalent stress divided by the maximum shear stress in an un-notched plate of equal geometry, i.e.,

$$K_t = \frac{2\sigma_{eqv}(r,z)}{\sigma_{rr(\max)}^{(un)} - \sigma_{\theta\theta(\max)}^{(un)}} \tag{7.1}$$

where $\sigma_{eqv}(r,z)$ is the equivalent stress, and $\sigma_{rr(\max)}^{(un)}$ and $\sigma_{\theta\theta(\max)}^{(un)}$ are the analytically derived maximum radial and hoop stresses, respectively, in an equivalent un-notched plate. Substituting in the theoretical maximum stresses from Eqs. 2.20 and 2.21 for $\sigma_{rr(\max)}^{(un)}$ and $\sigma_{\theta\theta(\max)}^{(un)}$ in Eqn. 7.1 yields

$$K_t = \frac{8\sigma_{eqv}(r,z)}{3q_0\left(\frac{a}{h}\right)^2(1-\nu)} \tag{7.2}$$

The shear stress concentration factor K_{ts} is defined as

$$K_{ts} = \frac{8\tau_{max}(r,z)}{3q_0\left(\frac{a}{h}\right)^2(1-\nu)} \tag{7.3}$$

Here τ_{max} is the maximum shear stress determined from

$$\tau_{max} = \frac{\sigma_1 - \sigma_3}{2} \tag{7.4}$$

where σ_1 and σ_3 are the maximum and minimum principal stresses, respectively.

Stress contours of the normalized equivalent stresses and the normalized maximum shear stresses throughout the un-notched plate subject to axisymmetric pressure are shown in Fig. 7.3. The stress contours appear similar between the equivalent and max shear stress and differ only in magnitude. Stress contours illustrating the equivalent stresses and maximum shear stresses for the benchmark notch geometry are shown in Fig. 7.4. From this figure, the localized increase in stress due to the presence of the notch is clearly shown and the maximum stress concentration factor of approximately 5.0 is found on the surface of the notch root.

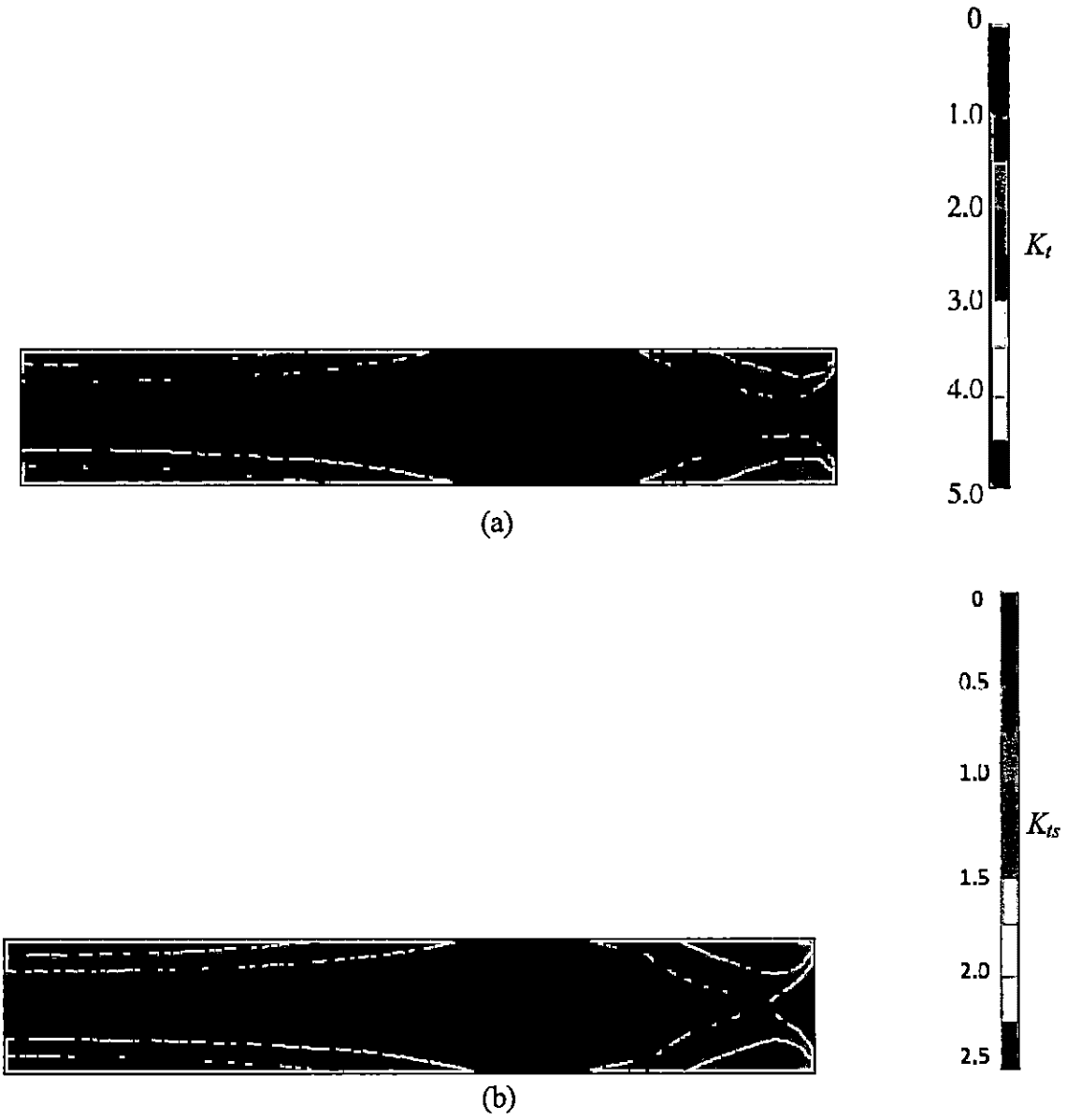

Figure 7.3. Elastic stress concentration factors, K_t (a), and K_{ts} (b), contours for un-notched plate.

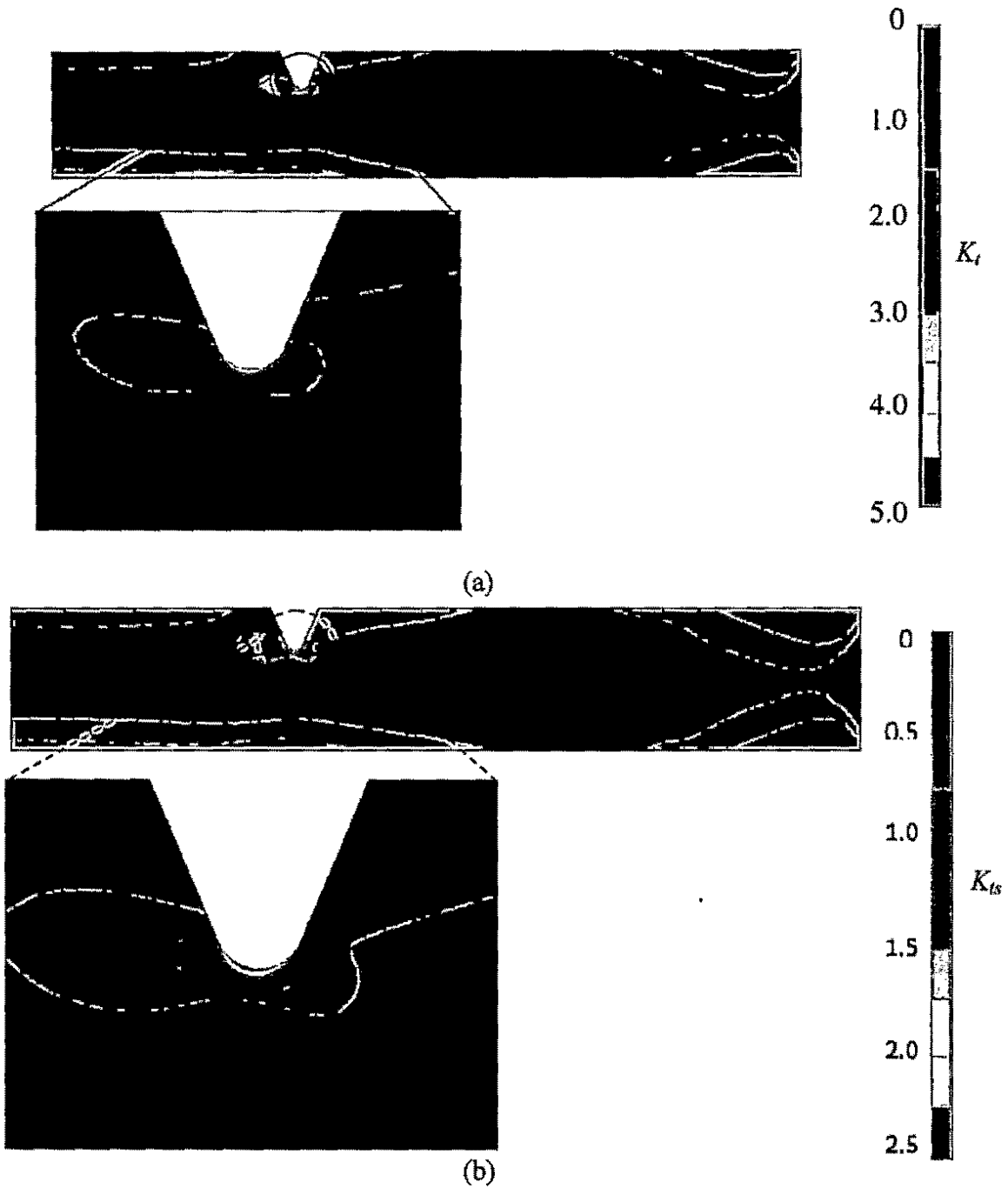

Figure 7.4. Elastic stress concentration factors, K_t (a), and K_{ts} (b), contours for benchmark notched geometry.

The effect notch geometry has on these SCFs are illustrated in a number of stress concentration factor diagrams. These plots were developed directly from data extracted from the parametric FEM simulations. For ease of analysis, the diagrams are divided into sections corresponding to the geometric parameter on the abscissa, namely r_n/a, α, t/h, or ρ/t. Each family of figures with the identical parameter on the abscissa consists of three separate plots, one for each of the other parameters being simultaneously varied. In each case, the two geometric notch parameters held constant take on benchmark conditions.

An important characteristic of stress concentration factors is the size of the zone in which the effect of the stress raiser is realized. Knowledge of the size of this zone is important because outside of this neighborhood of localized stress, the state of stress can be easily determined by traditional analytical methods depending on the loading condition and component geometry; therefore, only the stresses within this small zone need to be explored. The most direct application of this knowledge is in the setup of the FEM. The mesh outside of this zone is permitted to be coarse and only within the small area of interest is significant mesh refinement needed. To establish the relative size of the region of affected stress, the stress distribution along a horizontal line at a depth equal to the benchmark notch depth in both the smooth and notched case are plotted on the same diagram. Such a diagram is shown graphically in Fig. 7.5. Analysis of this comparative figure reveals that the stress distributions between the notched and smooth case differ significantly only in a zone equal to approximately 2.0% of the plate radius.

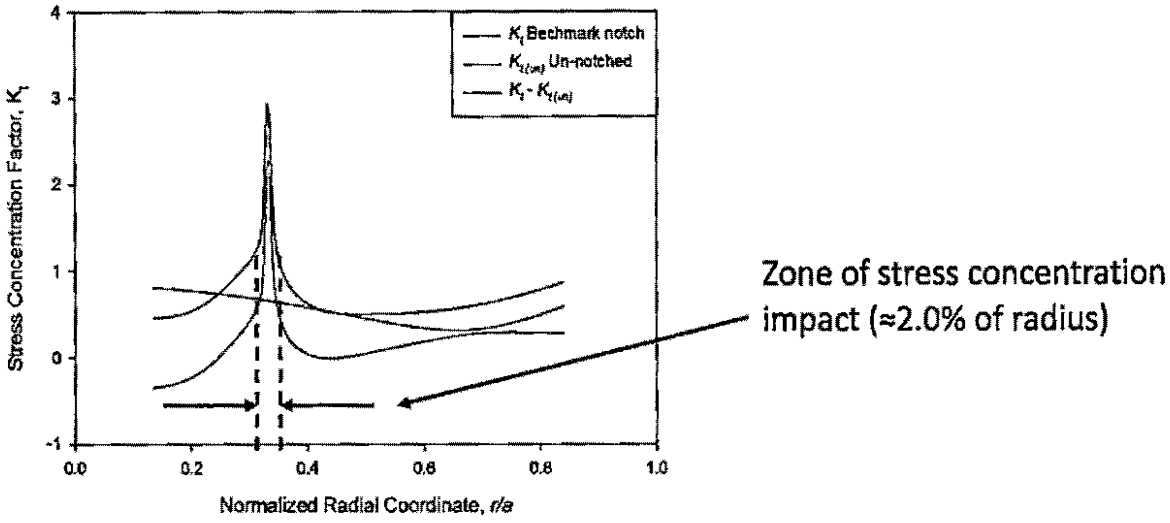

Figure 7.5. Horizontal stress distributions for smooth and benchmark notched cases.

7.1 Radial Location of Notch and SCFs

It was observed that the radial location of the notch, r_n, measured from the notch root middle, has the most significant effect on the maximum effective stress experienced on the surface of the notch. The strong dependence between stress and radial location is a direct result of the bending moments experienced throughout the plate. Referring to Eqs. 2.16 and 2.17, the bending moments throughout the plate are a function of the radial coordinate only and increase from a minimum at the center of the plate to a maximum at the circumferential edge. The radial location of the notch affected both the magnitude of the maximum equivalent stress and the stress distribution within the vicinity of the notch. The effects of the v-notch on the stress state throughout the plate are shown in Fig. 7.6. In this figure, the stress concentration factor, K_t is illustrated in the contours.

(a)

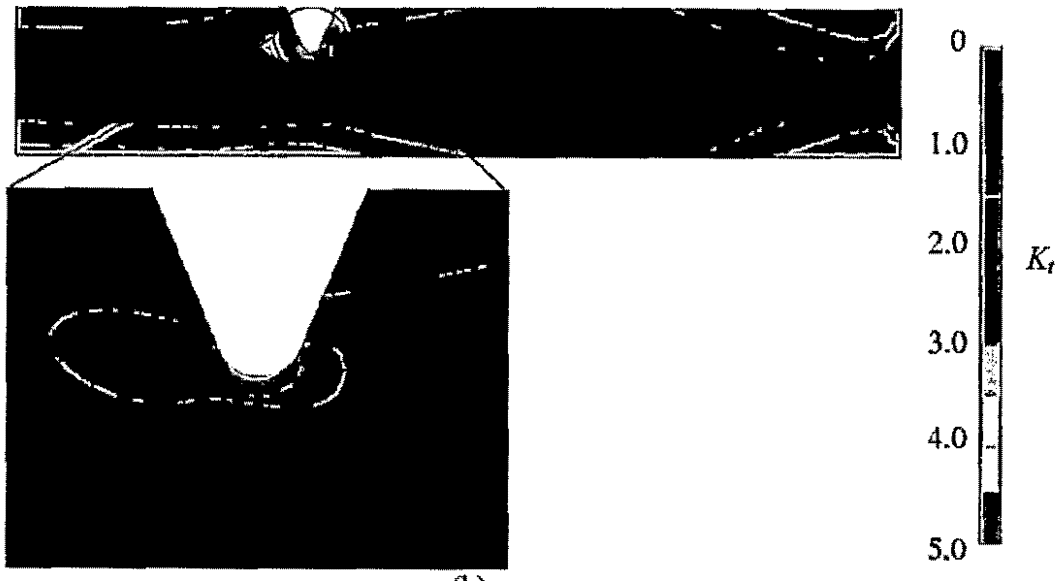

(b)

(c)

(d)

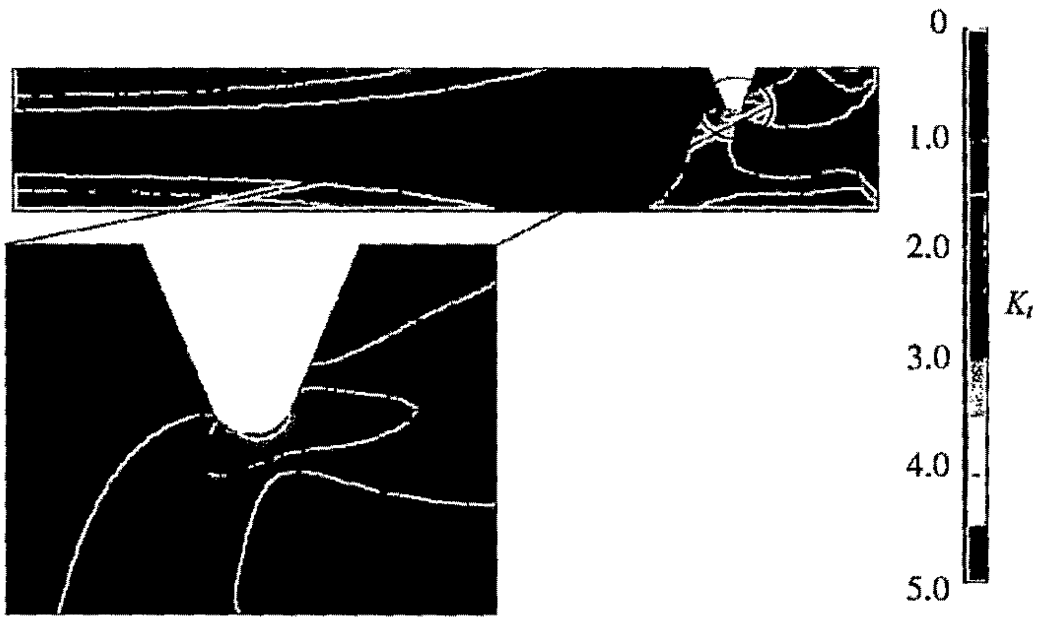

(e)

Figure 7.6. Elastic stress concentration factor, K_t, for various radial notch locations with other parameters at benchmark values; (a) $r/a = 0.17$, (b) $r/a = 0.33$, (c) $r/a = 0.50$, (d) $r/a = 0.67$, (e) $r/a = 0.83$.

It is shown that sharp notch radii yield higher stress concentration factors than blunt radii (Fig. 7.7) and smaller notch angles yield higher stress concentration factors than larger ones (Fig 7.8). These trends are both intuitive and consistent with v-notch elastic stress concentration factor results, and they have been observed in numerous stress concentration factor experiments (Pilkey, 1997). It can be observed from Fig. 7.9 that the stresses within the notch are not highly sensitive to the notch angle within the range studied. Leven and Frocht (1953) found that for a v-notched, thin beam element in bending that the notch angle did not affect the stress concentration factor for notch angles between 0° and 90°.

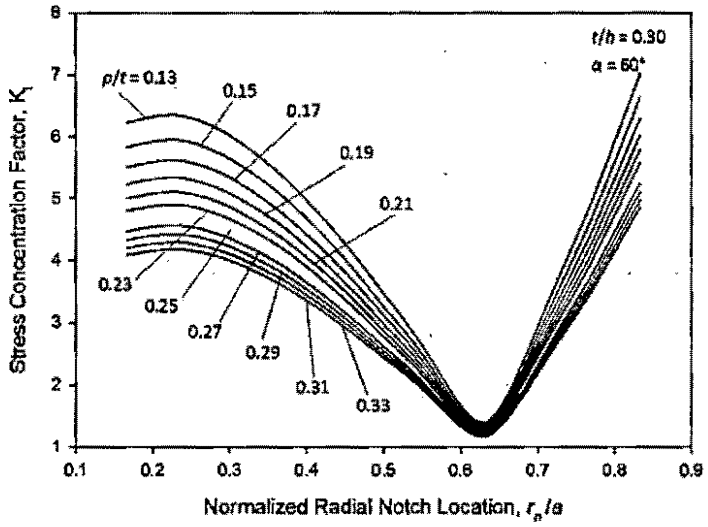

Figure 7.7. Elastic stress concentration factors with respect to the radial location of the notch for different notch root radii.

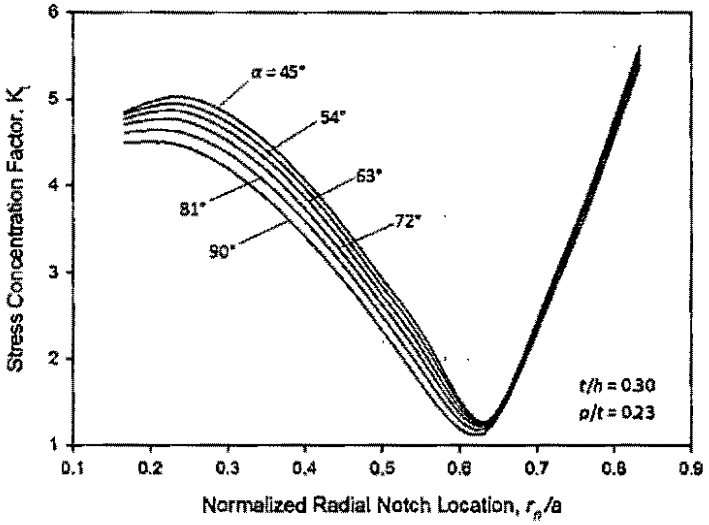

Figure 7.8. Elastic stress concentration factors with respect to the radial location of the notch for different notch angles.

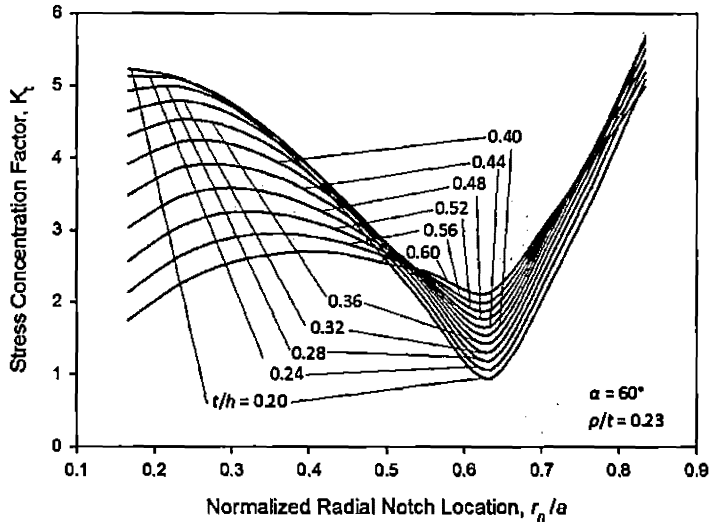

Figure 7.9. Elastic stress concentration factors with respect to the radial location of the notch for different notch depths.

An interesting relationship between stress and normalized notch depth, *t/h*, is shown in Fig. 7.8, specifically that shallow notches result in higher stresses in the regime before the minimum stress point but result in lower stresses at the minimum stress point. In other words, shallow notches are highly sensitive to the radial location of the notch whereas deep notches are weakly dependent on this parameter in the regime before the minimum stress point and all values of stress are similar in the regime after the minimum stress point. This varying level of dependence on the radial location is due to the equivalent stress dependence on the axial coordinate and can be readily observed for the un-notched case. Figure 7.10 shows theoretical equivalent stress distributions with respect to the radial location at various depths for an un-notched plate.

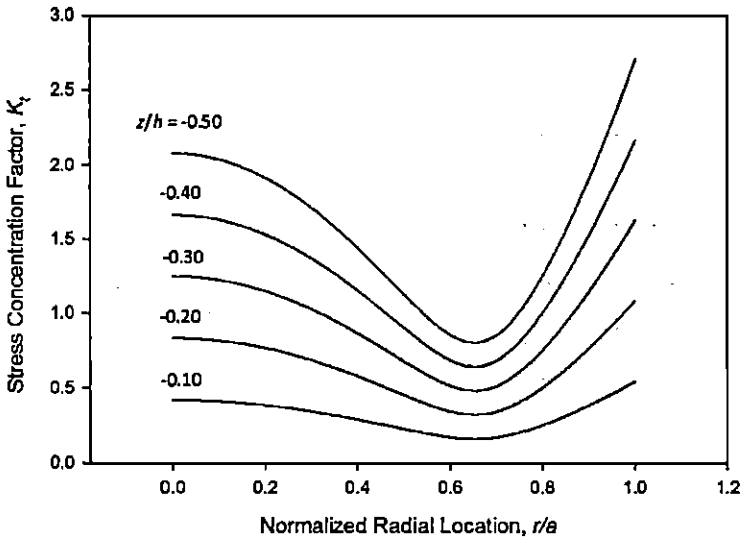

Figure 7.10. Theoretical equivalent stress distributions at various depths in an un-notched plate.

From these stress distributions it can be seen that for shallow depths within the plate, the radial location strongly affects the stress magnitude, whereas for depths closer to the neutral axis, this dependence on radial location becomes weak. A more detailed discussion on the effect notch depth has on the maximum equivalent stress is provided in the next chapter. A general trend observed in all three notched plate stress concentration factor plots is similar to that of the un-notched case. Specifically, the equivalent stress reaches a minimum point at approximately $r_n/a = 0.63$. This location of minimum stress can be derived mathematically for the un-notched case. The simplified equivalent stress formula for plane stress in polar coordinates can be expressed as

$$\sigma_{eqv} = \frac{1}{\sqrt{2}}\sqrt{(\sigma_{rr} - \sigma_{\theta\theta})^2 + (\sigma_{rr})^2 + (\sigma_{\theta\theta})^2} \tag{7.5}$$

Taking the derivative of this relation with respect to r and finding the positive root yields the following expression

$$\frac{r}{a} = \frac{(\nu + 1)\sqrt{14\nu^2 + 4\nu + 14}}{7\nu^2 + 2\nu + 7} \tag{7.6}$$

Equation 7.6 provides the radial location within an un-notched plate for which the von Mises stress will be a minimum and states that this location is a function of Poisson's ratio only. Substituting the value of Poisson's ratio for Ultem 1000 into Eqn. 7.6 yields a normalized radial location of $r/a = 0.65$ which agrees well with results from the FEA.

Another trend similar between all the plots is that stress dependence on the second parameter being varied (the one not on the abscissa) is significantly more pronounced before this minimum stress point, whereas after this minimum point the stress is dependent mostly on the radial location of the notch. This observation can be explained by the relationship between the bending moments within the un-notched plate and the radial location. As the radial location approaches the clamped circumferential edge, the bending moments rise to their maximum, as is shown in Eqs. 2.18 and 2.19; therefore, the stresses in this regime are dominated by the radial coordinate.

7.2 Notch Depth and SCFs

The maximum equivalent stress on the surface of the notch was found to be significantly affected by the depth of the notch. It was found that shallow notches caused higher stress concentration factors than deep notches. To understand the relationship between notch depth and stress, first dependence of stress on the axial coordinate within an un-notched plate is explored. Figure 7.11 represents vertical equivalent stress distributions from the top of the plate to the mid-plate at various radial locations within an un-notched plate.

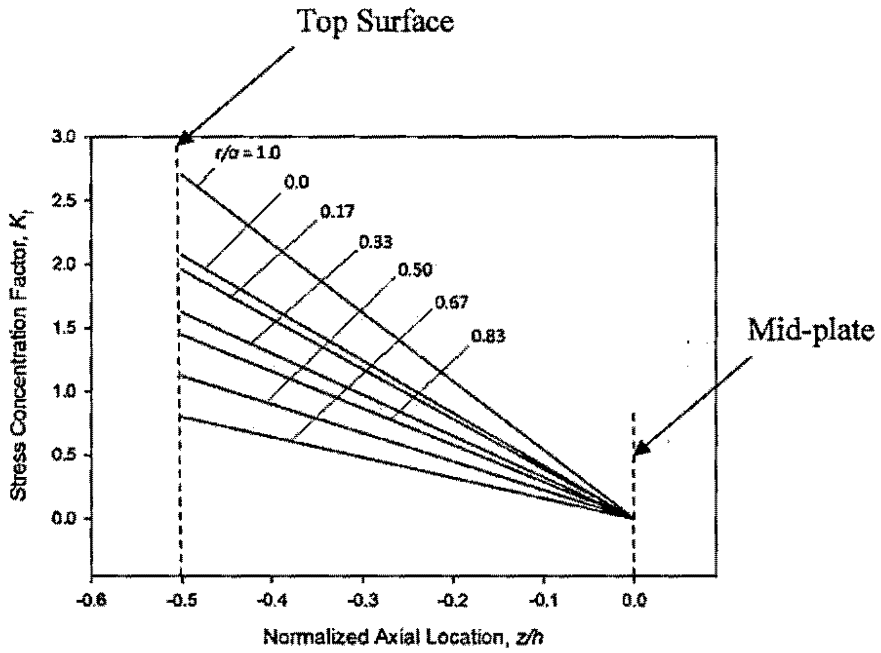

Figure 7.11. Theoretical equivalent stress distributions at various radial locations in an un-notched plate.

In these figures, the normalized axial location, z/h, ranges from -0.5, which corresponds to the top surface of the plate to 0.0, which corresponds to the mid-plane of the plate. From this figure, it is evident that the magnitude of equivalent stress is the greatest at the surface of the plate and decreases linearly to zero at the mid plane. A similar stress dependence on the axial location is present in the notched case. Finite element analysis contours of the stress concentration factor, K_t for plates with various notch depths are shown in Fig. 7.12. It is readily observed from this figure that as the notch depth approaches the mid-plane, the maximum stresses in the vicinity of the notch decrease.

(a)

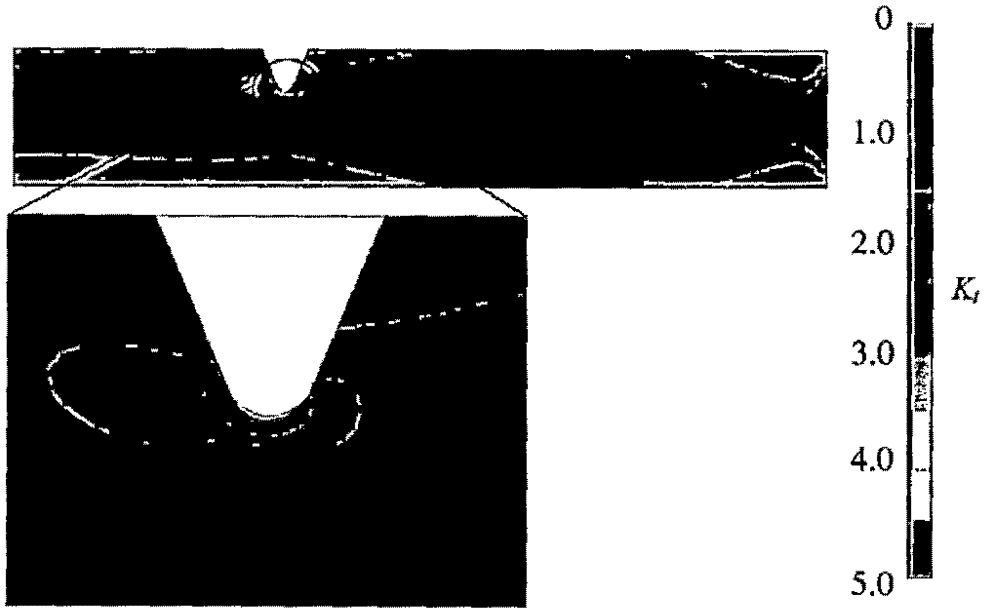

(b)

(c)

(d)

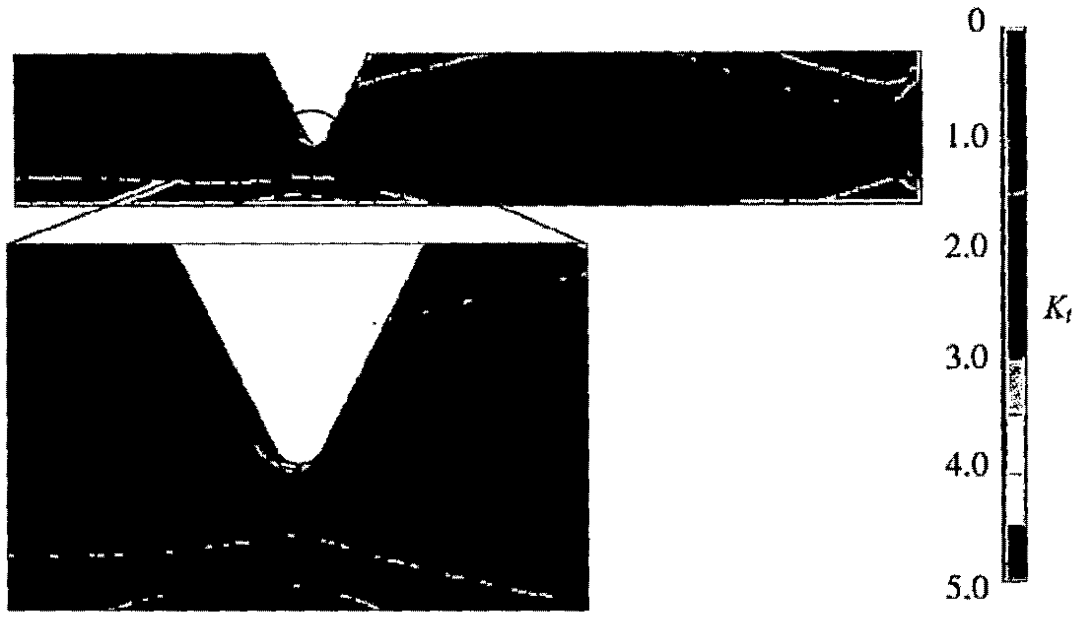

(e)

Figure 7.12. Elastic stress concentration factor, K_t for various notch depths with other parameters at benchmark values; (a) $t/h = 0.20$, (b) $t/h = 0.30$, (c) $t/h = 0.40$, (d) $t/h = 0.50$, (e) $t/h = 0.60$.

The stress concentration factors for various notch depths with respect to the other geometric notch parameters are shown graphically in Figs. 7.13 and 7.14. The trend of decreasing stress with increasing notch depth is depicted in these figures. This family of curves was fit to the following equation with at least an R^2 value of 0.999.

$$K_t = a + b\left(\frac{t}{h}\right)^3 \tag{7.7}$$

where a and b are coefficients which can be found in the inset of Figs. 7.13 and 7.14. The weak correlation between the maximum equivalent stress realized on the surface of the notch and notch angle is shown in Fig. 7.13 where the stress concentration factor varies only slightly for the range of angles. It can be shown, however, Fig. 7.14 that the notch root radius has a significant effect on the stresses within the notch represented by a larger range of stress concentration factors.

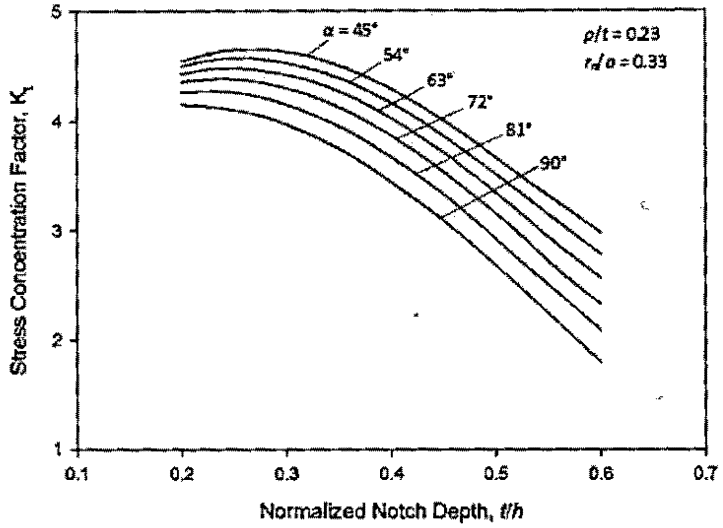

$$K_t = a + b\left(\frac{t}{h}\right)^3$$

α	a	b
45°	4.7848	-8.5157
54°	4.7119	-9.1344
63°	4.6277	-9.8146
72°	4.5306	-10.5574
81°	4.4007	-11.1734
90°	4.2435	-11.8538

Figure 7.13. Elastic stress concentration factors with respect to notch depth for different notch angles.

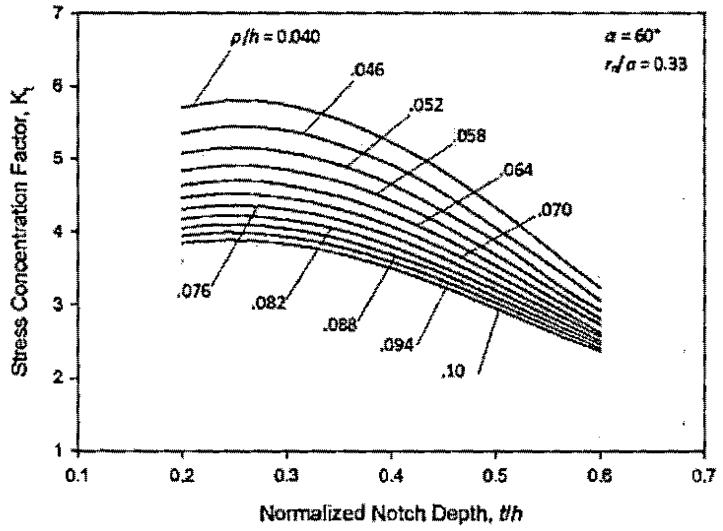

$$K_t = a + b\left(\frac{t}{h}\right)^3$$

ρ/h	a	b
0.040	6.0065	-13.0198
0.046	5.6317	-12.1070
0.052	5.3263	-11.3692
0.058	5.0680	-10.6595
0.064	4.8438	-10.0260
0.070	4.6594	-9.6328
0.076	4.4898	-9.1105
0.082	4.3405	-8.7450
0.088	4.2073	-8.3726
0.094	4.0887	-8.0481
0.100	3.9839	-7.7781

Figure 7.14. Elastic stress concentration factors with respect to notch depth for different notch root radii.

7.3 Notch Root Radius and SCFs

The relationship observed between the notch root radius and the maximum stresses on the surface of the v-notch was consistent with typical notch problems. More specifically, the stresses in the vicinity of the notch where shown to increase as the notch root radius was decreased. This trend is illustrated in a number of stress contours, shown in Fig. 7.15, representing the elastic stress concentration factor, K_t, for v-notches with various root radii. From these contours, the larger stresses are apparent in the notches with sharper notch radii

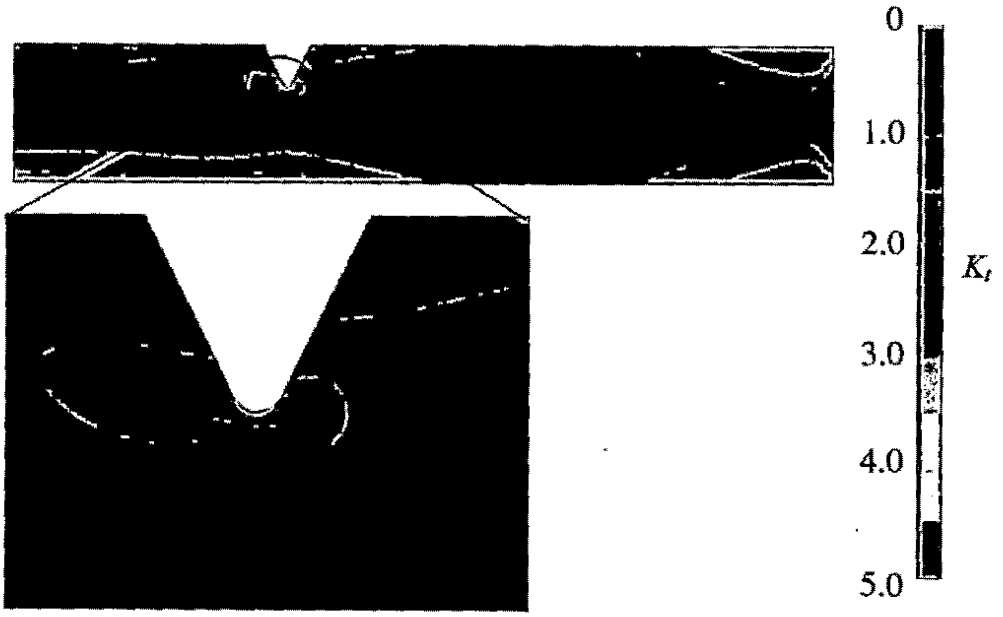

(a)

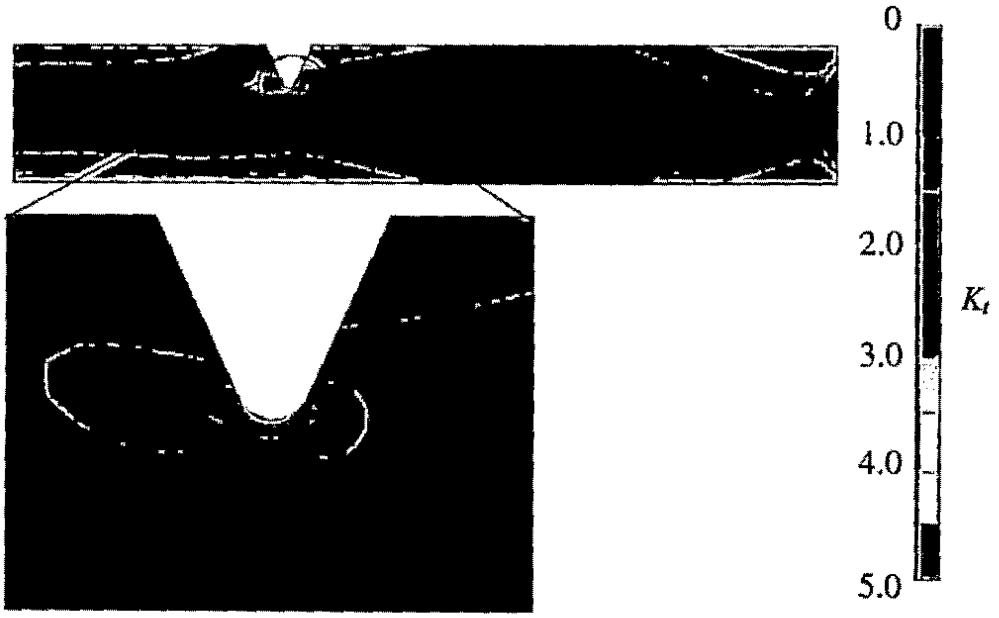

(b)

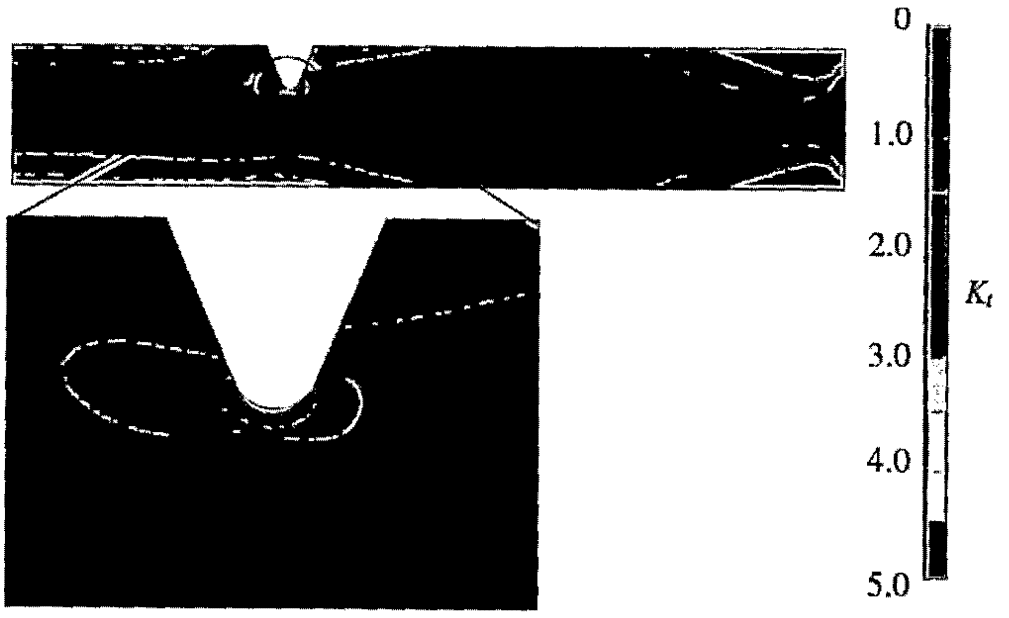

(c)

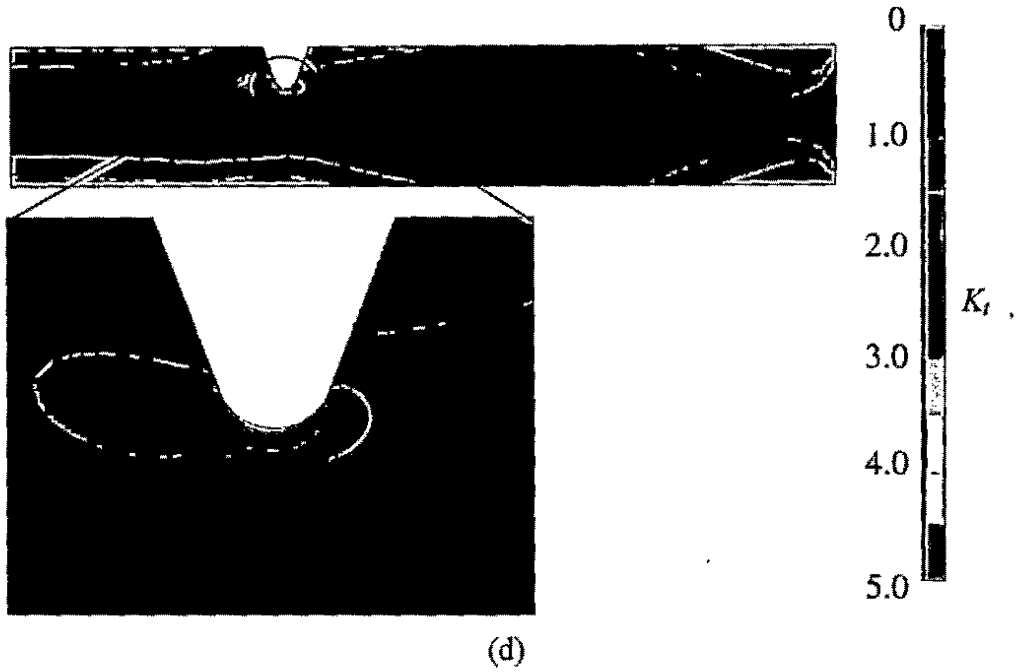

(d)

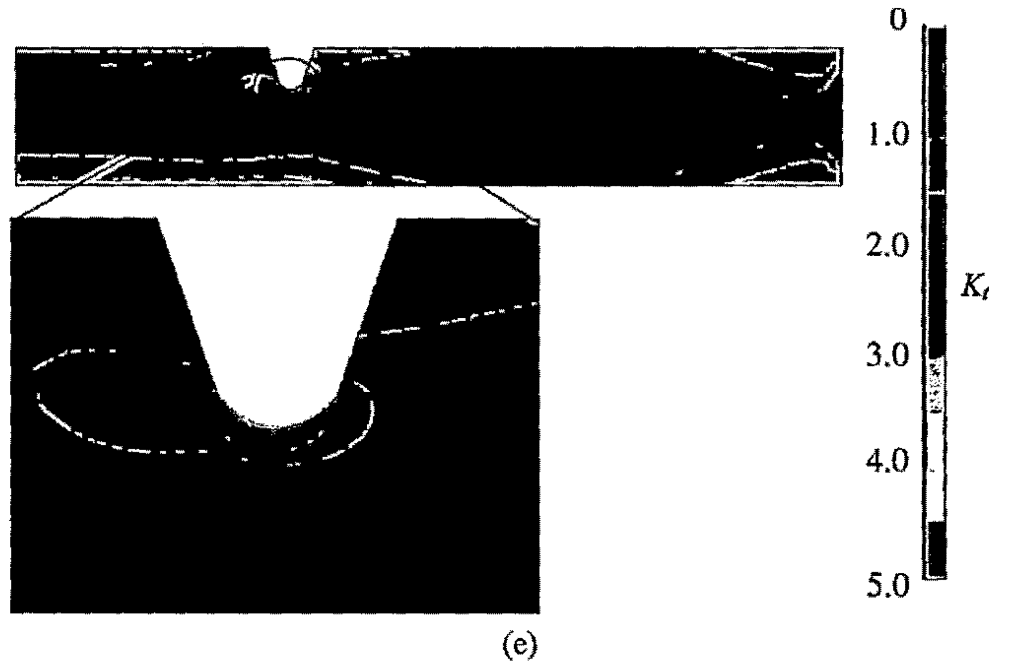

(e)

Figure 7.15. Elastic stress concentration factor, K_t, for various notch root radii with other parameters at benchmark values; (a) $\rho/t = 0.13$, (b) $\rho/t = 0.18$, (c) $\rho/t = 0.23$, (d) $\rho/t = 0.28$, (e) $\rho/t = 0.33$.

Trends highlighting the relationship between notch radius and the maximum equivalent stress on the surface of the notch for the v-notched plate are shown graphically

in Figs. 7.16 – 7.18. These curves were fit to the following equation with a correlation of at least R^2 equal to 0.999.

$$K_t = a + b\sqrt{\frac{t}{\rho}} \tag{7.8}$$

where a and b are coefficients which can be found in the inset of Figs. 7.16 – 7.18. The functional form of Eqn. 7.8 follows the classical stress concentration factor formulation developed by Inglis (1913).

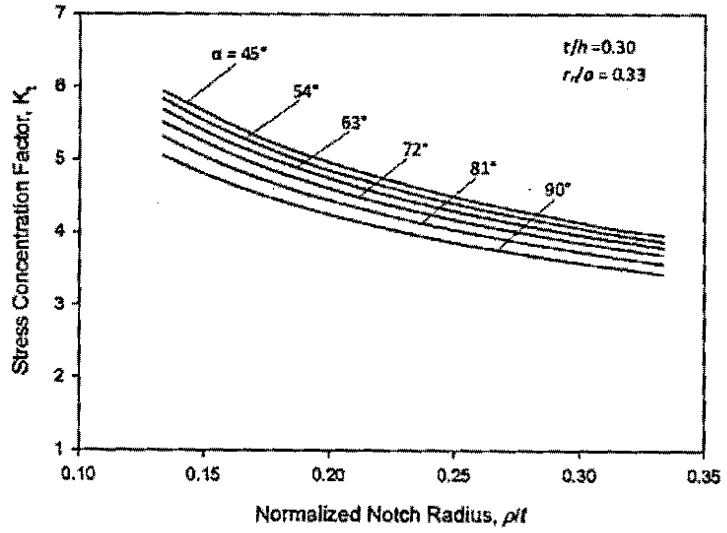

$$K_t = a + b\sqrt{\frac{t}{\rho}}$$

α	a	b
45°	0.5499	1.9702
54°	0.5374	1.9306
63°	0.5540	1.8711
72°	0.5831	1.7972
81°	0.6093	1.7134
90°	0.6620	1.6015

Figure 7.16. Elastic stress concentration factors with respect to notch root radius for different notch angles.

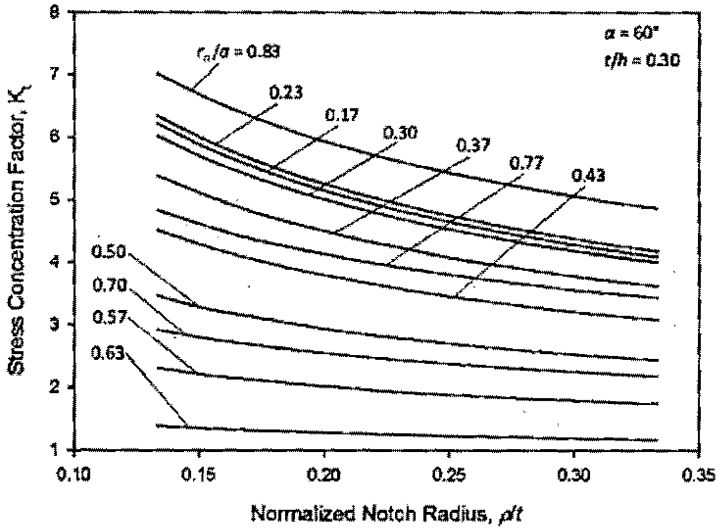

$$K_t = a + b\sqrt{\frac{t}{\rho}}$$

r_n/a	a	b
0.17	0.4010	2.1245
0.23	0.4440	2.1530
0.30	0.5014	2.0154
0.37	0.5592	1.7614
0.43	0.6037	1.4270
0.50	0.6771	1.0134
0.57	0.7546	0.5671
0.63	0.7966	0.2160
0.70	0.9147	0.7319
0.77	1.0230	1.3893
0.83	1.1377	2.1478

Figure 7.17. Elastic stress concentration factors with respect to notch root radius for different radial notch locations.

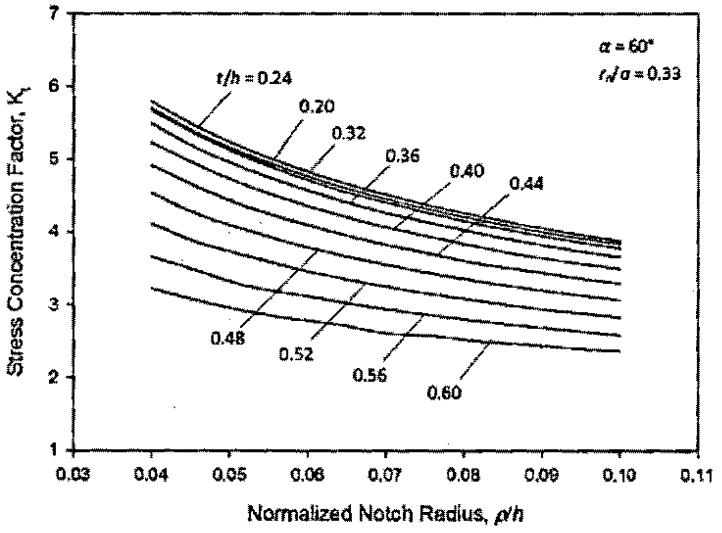

$$K_t = a + b\sqrt{\frac{h}{\rho}}$$

t/h	a	b
0.20	0.6392	1.0114
0.24	0.5847	1.0410
0.28	0.5342	1.0494
0.32	0.5233	1.0296
0.36	0.5180	0.9935
0.40	0.4953	0.9474
0.44	0.5052	0.8811
0.48	0.5584	0.7935
0.52	0.6325	0.6949
0.56	0.7613	0.5784
0.60	0.8810	0.4672

Figure 7.18. Elastic stress concentration factors with respect to notch root radius for different notch depths.

It was found that the notch radius has a greater effect on the maximum equivalent stress than the notch angle within the range studied. This observation is illustrated in Fig.

7.16 where the stress concentration factor varies only slightly for changes in notch angle. The radial location of the notch has a greater effect on the maximum equivalent stress than the notch radius in the range $0.30 \leq r_n/a \leq 1.0$, as is shown in Fig. 7.17, where changes in the radial location within this range yield significant changes in the stress concentration factor K_t. Similarly, the stress is more sensitive to changes in the notch depth than the notch radius in the range $0.40 \leq t/h \leq 0.60$, as is shown in Fig 7.18.

7.4 Notch Angle and SCFs

Within the range of notch angles studied, it was found that the notch angle does not significantly affect the stress concentration factor K_t. From Fig. 7.19, it is shown that the stresses present in the radius of the notch are similar for all values of notch angle.

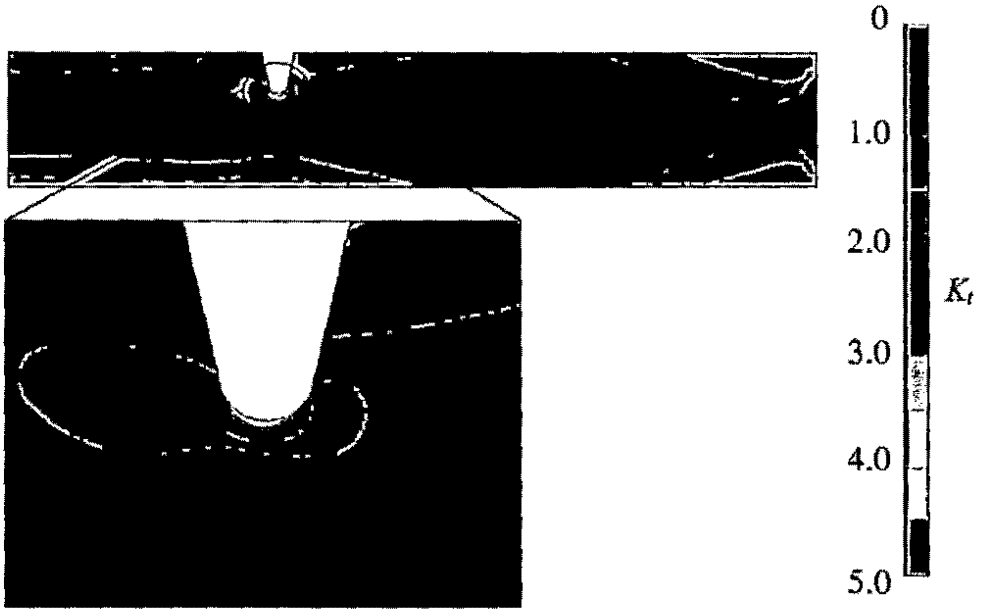

(a)

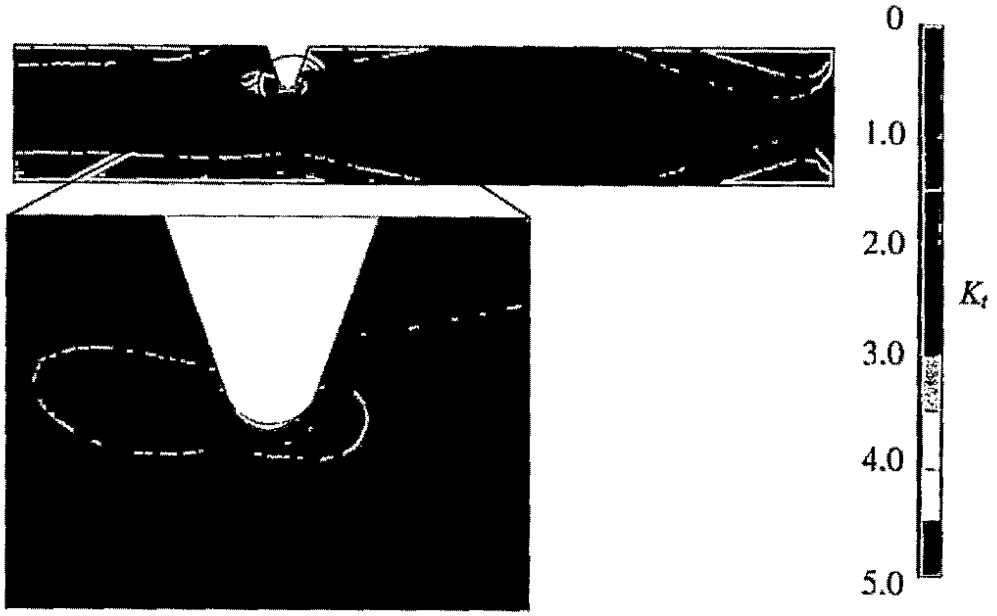

(b)

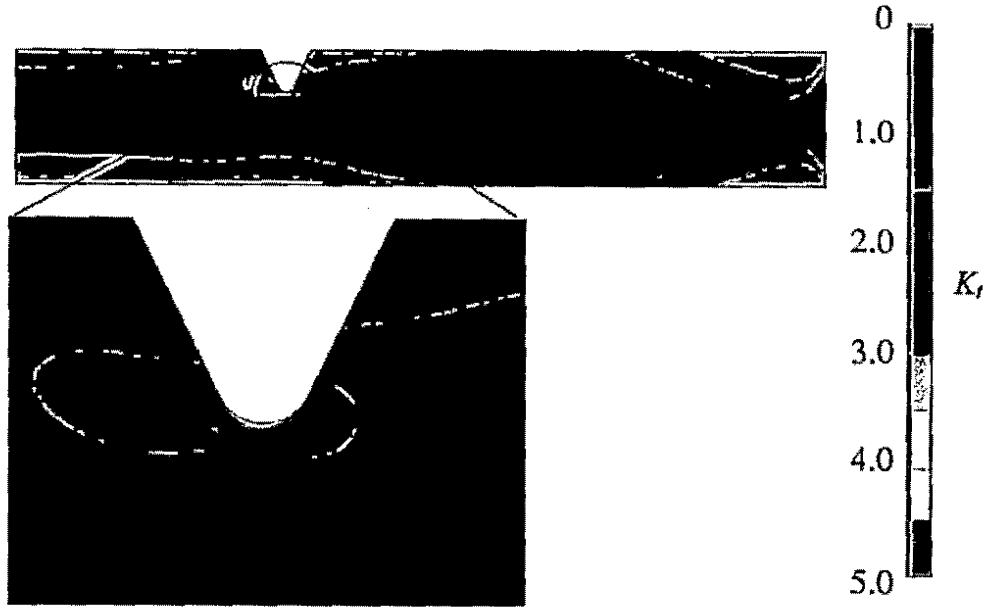

(c)

(d)

(e)

Figure 7.19. Elastic stress concentration factor, K_t, for various notch angles with other parameters at benchmark values; (a) $\alpha = 45°$, (b) $\alpha = 55°$, (c) $\alpha = 65°$, (d) $\alpha = 75°$, (e) $\alpha = 85°$.

These trends are depicted graphically in Figs. 7.20 and 7.21. These plots further solidify the observation that the stresses in the notch are not highly sensitive to the notch angle. This weak correlation is due to the fact that the geometry of the notch root is effectively unchanged throughout the studied range of notch angles. Since the maximum stresses are realized in a very confined vicinity of the notch root, a very minute change in geometric configuration of the radius tip will result in minute change in stress.

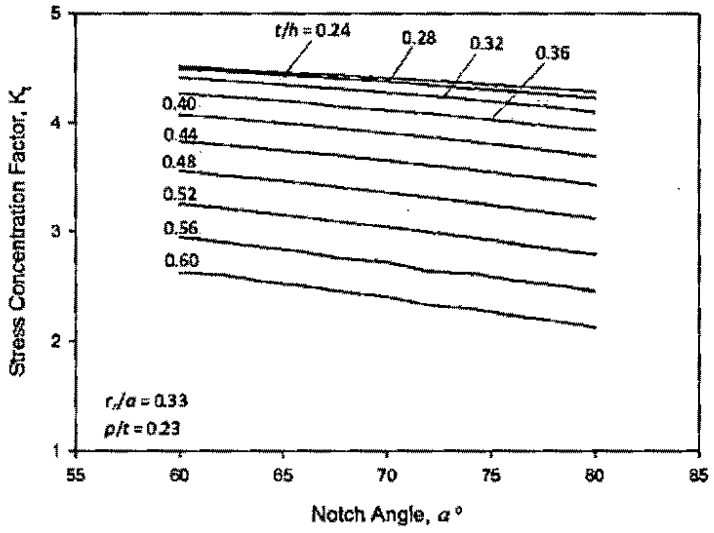

Figure 7.20. Elastic stress concentration factors with respect to notch angle for different notch depths.

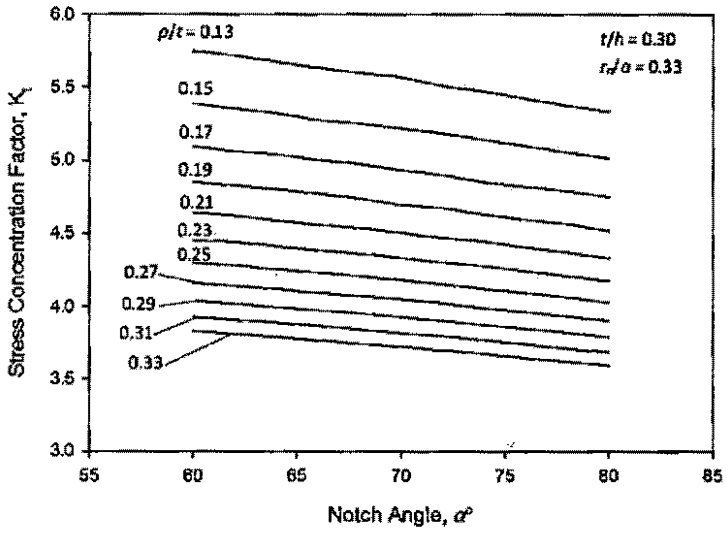

Figure 7.21. Elastic stress concentration factors with respect to notch angle for different notch root radii.

7.5 Angular Stress Distribution

The previous sections focused on how the behavior of the maximum stresses at the notch root varies as a function of various geometric parameters of the notch. The present section investigates the angular stress distributions about the surface of the notch. These stress distributions are characterized by the angular location parameter β, shown in Fig.7. 22. A value of $\beta = 0°$ corresponds to the exact middle of the notch root. The equivalent stress values of nodes along the radius of the notch were extracted along with the Cartesian location of the nodes. The Cartesian locations were converted into angular locations and the nodes were sorted in ascending order based on angular location through use of a Fortran code provided in Appendix A. The resulting angular stress distribution codes provide insight into the location within the notch root experiencing maximum stress. In typical symmetric notch problems, the maximum stress is found at the middle

of the notch root; however, in the case of axisymmetrically loaded plates, the location of the maximum stress is a function of notch geometry and location.

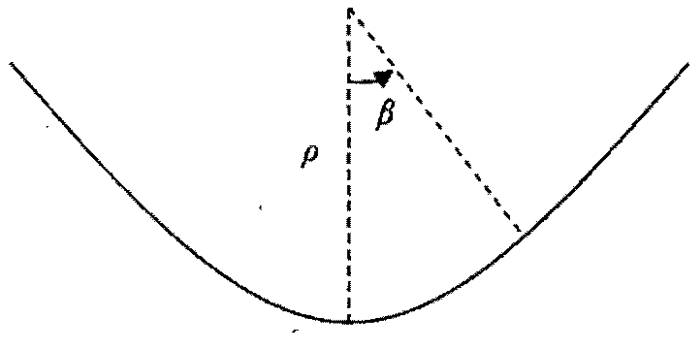

Figure 7.22. Angular stress distribution parameter β along the root radius of the notch.

The radial location of the notch was observed to have the greatest effect on the angular stress distributions. This result is expected since the radial location of the notch was shown to have the largest effect on the state of stress throughout the plate. Figure 7.23 depicts the angular distributions of the elastic stress concentration factor, K_t, for various radial locations of the notch at otherwise benchmark conditions.

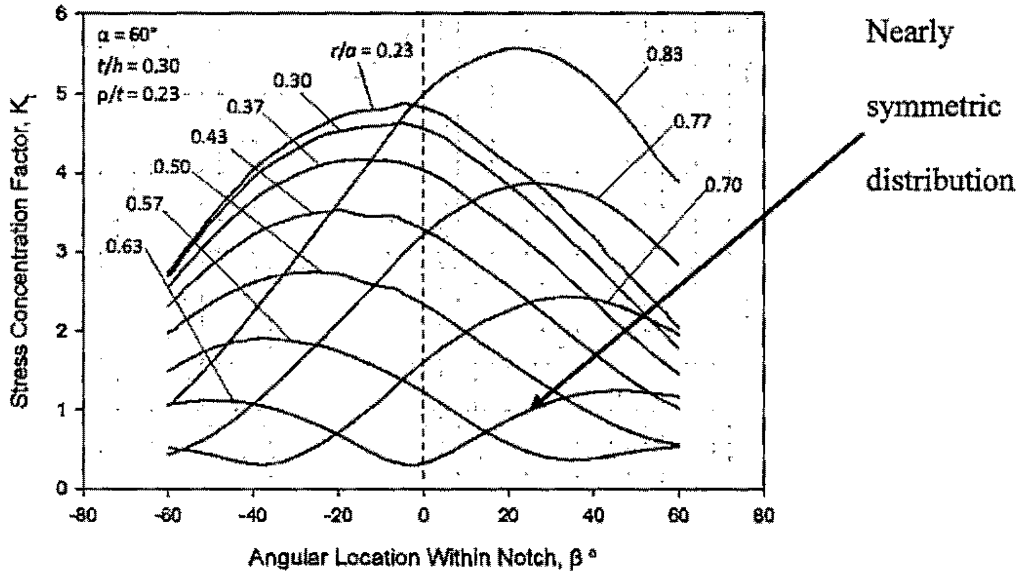

Figure 7.23. Angular stress distributions of K_t along the root radius of the notch for various radial notch locations.

A number of results can be drawn from this figure with respect to the relationship between the radial location of the notch and the magnitude and location of the maximum equivalent stresses along the notch root. Similar to the results discussed in section 7.1, it is shown in Fig. 7.23 that the magnitude of the stresses along the notch radius decrease as the radial location of the notch is increased until a transition point is reached ($r/a = 0.63$), after which an increase in the radial location of the notch causes a large increase in the magnitude of the notch tip stresses. Regarding the angular location of the maximum equivalent stress, Fig. 7.23 illustrates that this location is a negative β for radial locations less the transition point and a positive β for radial locations after this transition point. Interestingly, a nearly symmetric angular stress distribution is observed at this transition point of $r/a = 0.63$ and is highlighted in the figure.

The relationship between the depth of the notch and the resulting angular stress distributions was similarly explored. It was found that the relative magnitude of the angular stress distributions decreased as the depth of the notch approached the mid-plane, similar to the results discussed in section 7.2. This general trend is shown in Fig. 7.24. The radial location of maximum equivalent stress was observed to be near the middle of the notch root for shallow notches, but to diverge towards large negative angular locations as the notch depth was increased.

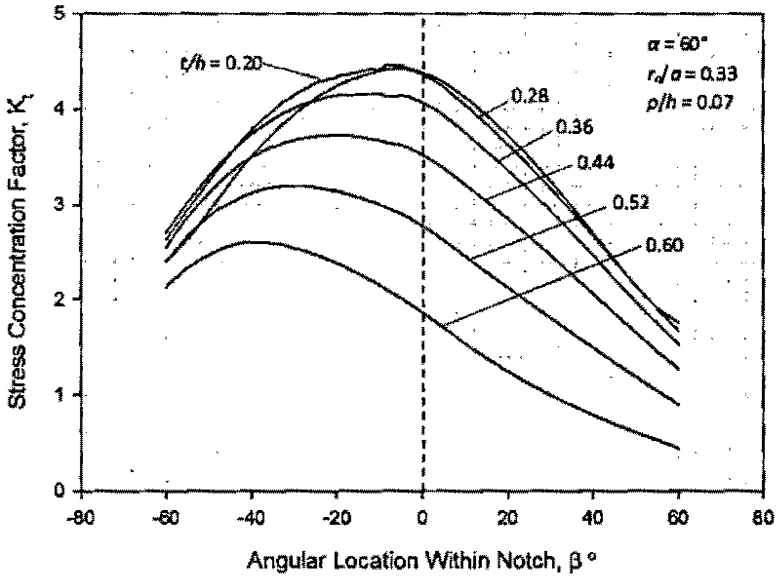

Figure 7.24. Angular stress distributions along the root radius of the notch for various notch depths.

The radius of the notch was observed to have a negligible effect on the angular location of the maximum equivalent stress. As shown in Fig. 7.23, only the magnitude of the stress distribution was affected by notch radii. This observation is due to the fact that a change in the radius of the notch root does not alter the location of the notch tip within the plate, and therefore does not affect the inherent stress state corresponding to that particular radial and axial location. As discussed earlier, changes in the location of the

notch tip throughout the plate affect both the magnitude and shape of the angular stress distributions; however, changes to purely notch geometry only affect the stress magnitude. This point is also illustrated in Fig. 7.26, in which the elastic stress concentration factor distributions with respect to various notch angles are depicted graphically.

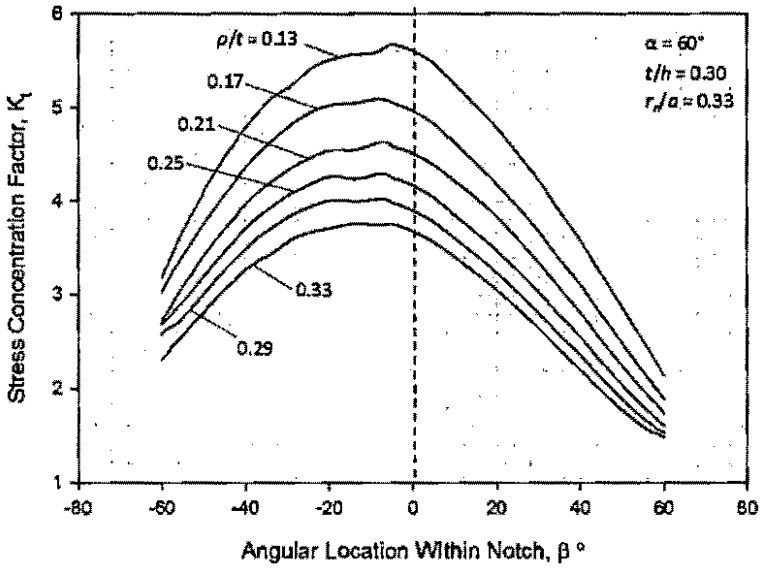

Figure 7.25. Angular stress distributions along the root radius of the notch for various notch radii.

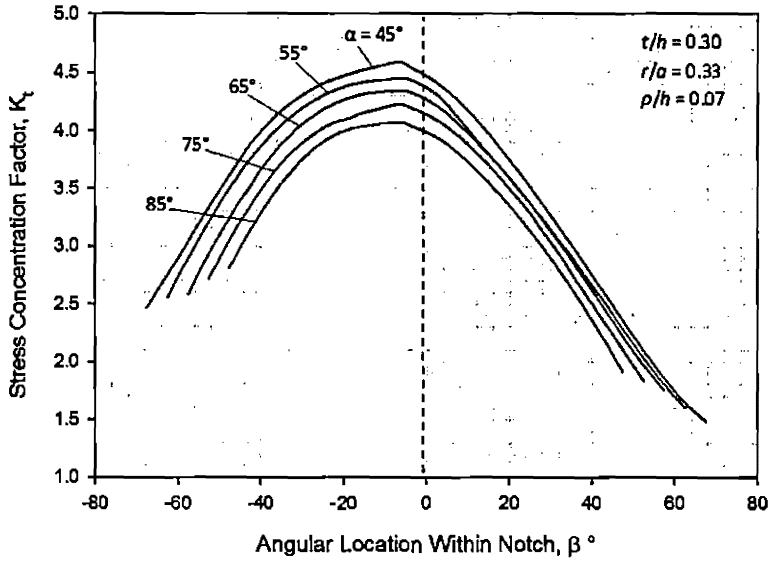

Figure 7.26. Angular stress distributions along the root radius of the notch for various notch angles.

7.6 Vertical Stress Distribution

The vertical stress distributions with respect to various geometric notch parameters were investigated similarly to the angular stress distributions. The vertical stress distribution is characterized by the normalized vertical location parameter, *z/d,* as shown in Fig. 7.27. The vertical stress distribution originates at the middle of the notch root tip and traversed to the bottom of the plate corresponding to a $z/d = 0.714$.

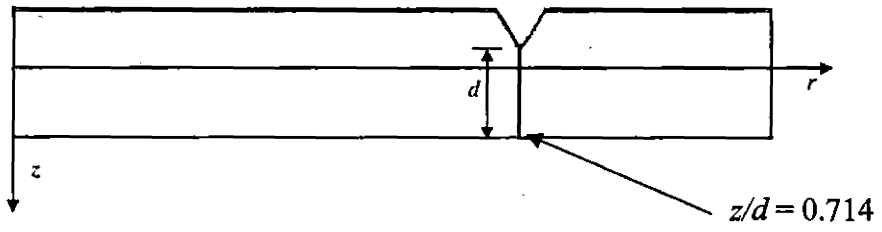

Figure 7.27. Vertical stress distribution parameter *z*.

Both the magnitude and the distribution of the equivalent stresses ahead of the notch were found to be greatly influenced by the radial location of the notch. The vertical elastic stress concentration factor distributions for various radial notch locations are shown in Fig. 7.28. The maximum stresses along this vertical line are realized at the notch tip (z/d = -0.29). It is important to distinguish that this is the maximum stress along this vertical line which bisects the notch root radius and may not be the maximum stress along the notch root. The location of the maximum stress along the notch root was discussed in section 7.5.

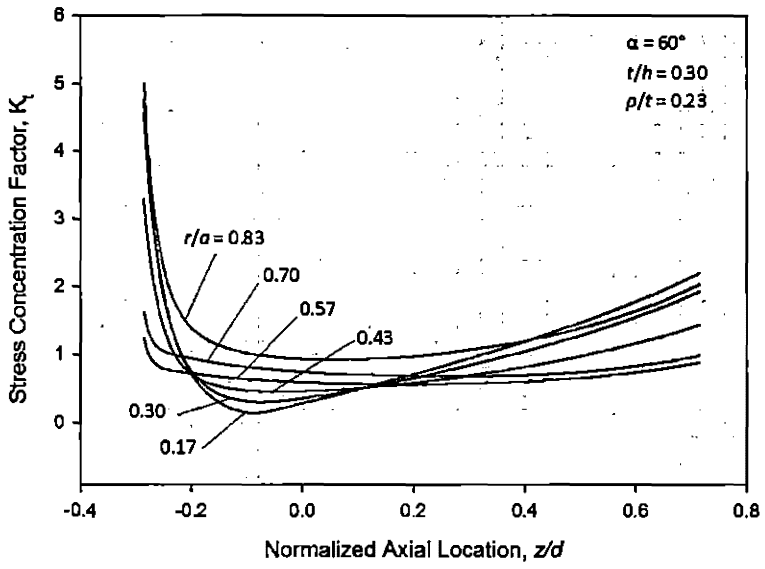

Figure 7.28. Stress distributions ahead of the notch for various radial notch locations.

For all the curves in Fig. 7.28, a common trend observed is that equivalent stresses rapidly decrease from the maximum at the notch tip to the minimum value; after which the stresses slowly increase until the bottom of the plate is reached. Similar to results observed for the angular stress distributions with respect to the radial location, it is shown in Fig. 7.28 that the curves corresponding to r/a = 0.57 and r/a = 0.70 are both the

smallest in magnitude and represent a nearly constant stress concentration factor throughout the thickness of the plate.

The depth of the notch was shown to merely affect the magnitude of the stress concentration factor distribution ahead of the notch. As shown in Fig. 7.29, the stress distributions are similar in shape, but differ in the value of the maximum stress concentration factor. Also, these curves originate at different axial locations because the depth of the notch was the geometric parameter varied in this particular case. This is also the reason that the axial location, *z*, is normalized by the height of plate, *h*, instead of *d*.

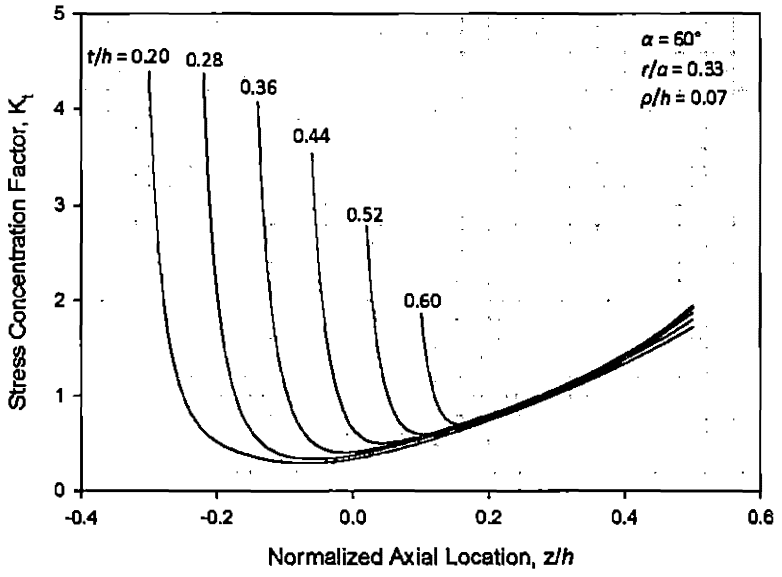

Figure 7.29. Stress distributions ahead of the notch for various notch angles.

The radius of the notch root and the angle of the notch were shown to only slightly affect the elastic stress concentration factor distributions ahead of the notch. These results are consistent with the previously observed results with respect to the influence of these geometric parameters on stress in the vicinity of the notch. The stress

distributions ahead of the notch with respect to the radius of the notch root and the notch angle are depicted graphically in Figs. 7.30 and 7.31, respectively.

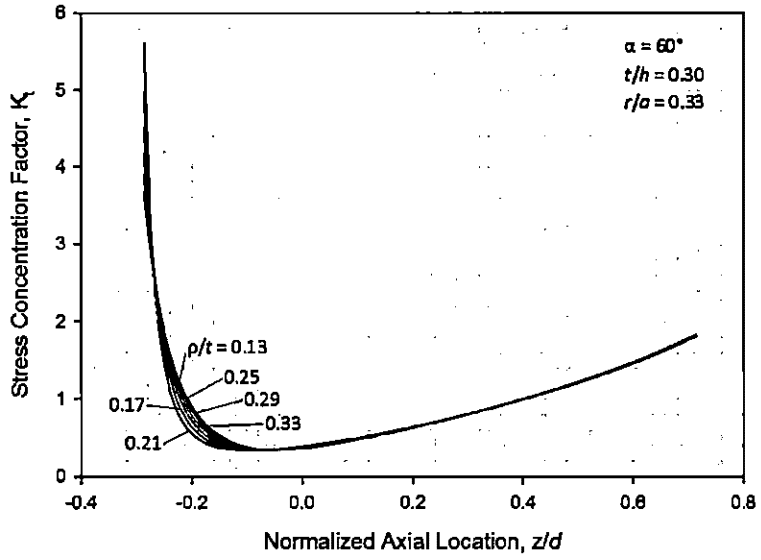

Figure 7.30. Stress distributions ahead of the notch for various notch root radii.

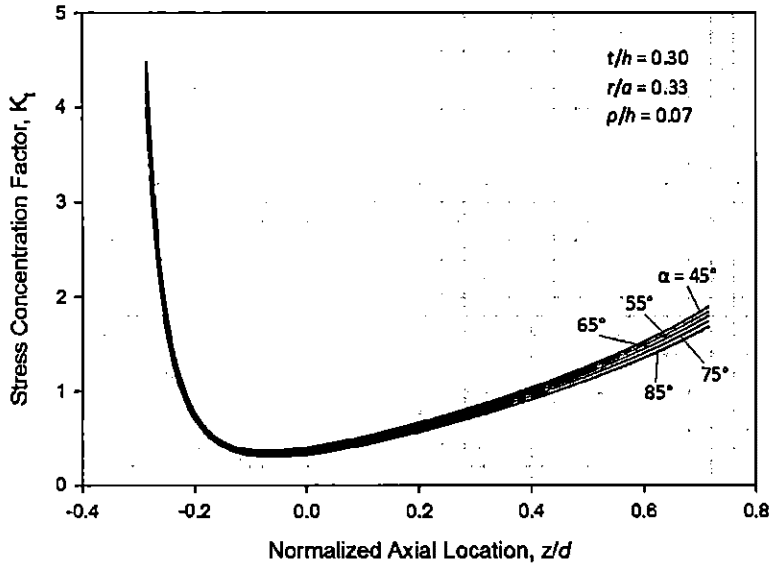

Figure 7.31. Stress distributions ahead of the notch for various notch angles.

A key distinction between these two diagrams is that the stress distributions vary at different axial locations. For example, as shown in Fig. 7.30, the notch root radii affect only the magnitude of the minimum stress concentration value and this deviation is confined to a small axial range. Regarding Fig. 7.31, the stress distribution curves differ only in the region close to the bottom of the plate.

7.7 Solution Mesh Independence Verification

To verify that the FEA solutions were independent of the meshing scheme, a mesh independence verification was performed. The purpose of this verification is to prove that the FEA solutions approach a value with successive mesh refinements and that the solutions are independent of mesh asymmetry about the notch tip. To best illustrate this, the angular stress distribution about the notch tip was solved using various mesh refinements and plotted on the same figure. The angular stress distribution was chosen in the mesh independence study to verify that the asymmetry in the stress distribution is not an artifact of mesh asymmetry. Figure 7.32 shows the meshing scheme of the benchmark notched configuration at four successive levels of refinement.

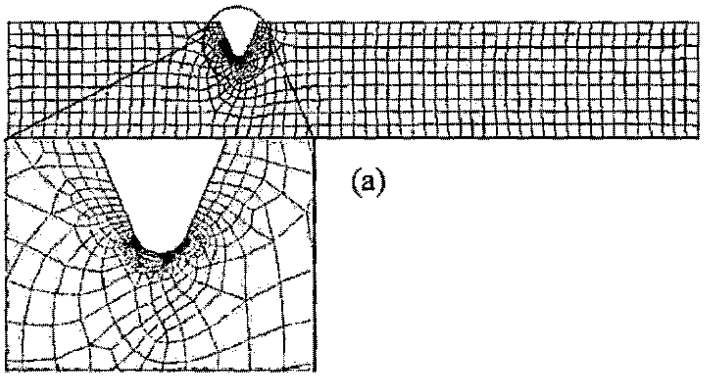

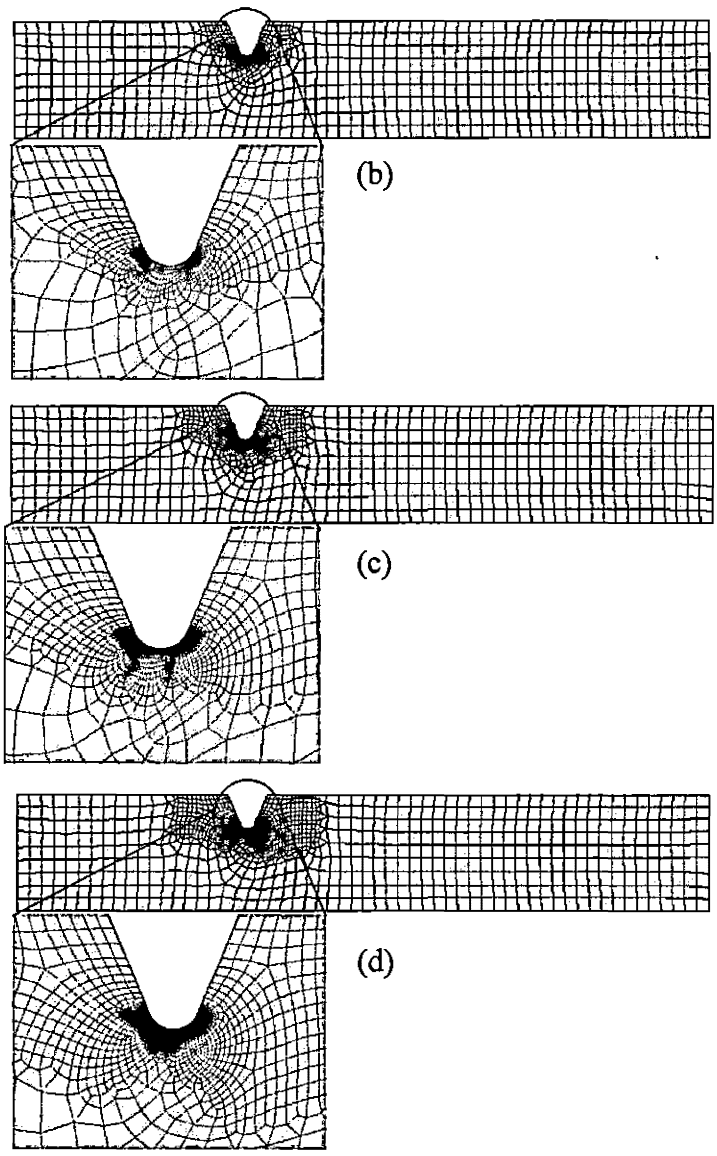

Figure 7.32. Mesh of benchmark notch configuration at refinement (a) level 1, (b) level 2, (c) level 3, and (d) level 4.

The angular stress distributions solved from each of these meshing schemes are illustrated in Fig. 7.33. From this figure, it is evident that the angular stress distribution is only slightly affected by the mesh refinement level and is shown to approach a common curve with successive refinements. The level 4 mesh refinement was used throughout the entire FEA of the current paper. It can be concluded from this mesh independence

analysis that the solutions of the stress distributions in the vicinity of the notch are independent of the mesh asymmetry about the notch tip. Furthermore, it was shown that the solution to the stress distribution approaches a value and continued levels of refinement would not yield higher accuracy.

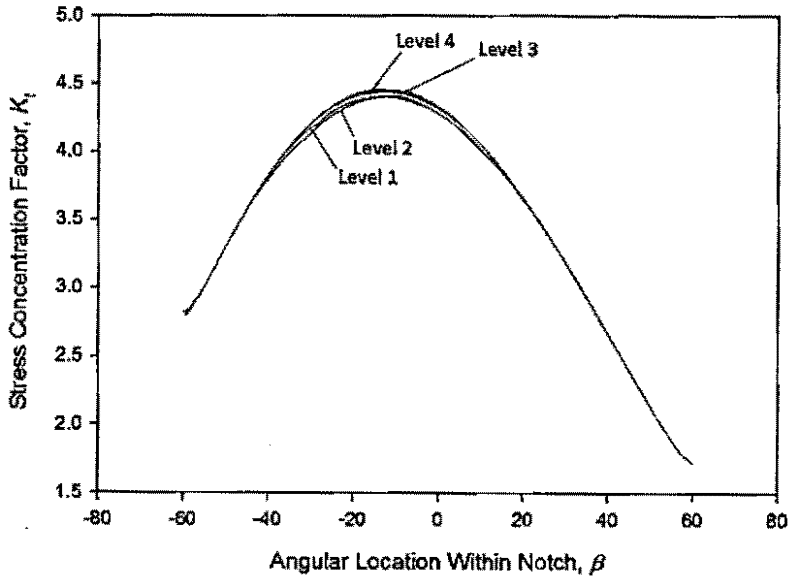

Figure 7.33. Angular stress distribution solutions for various mesh refinement levels.

8. Conclusions

In summary, relationships between v-notch stress concentration factors and notch geometry and location were formulated through parametric finite element analysis. Correlations between individual geometric notch parameters and resulting stress concentration factors were mathematically modeled. Such models could be used by plate designers to determine the necessary notch geometry for a desired stress concentration factor. The relation formulated providing the stress concentration factor as a function of the notch root radius was found to closely match the form of that determined by Inglis (1913). This result suggests that further correlations between stress concentration factor relations for simple and axisymmetric loading can be developed. In general, it was determined that the stresses in the vicinity of the notch tip were more sensitive to changes in notch location (r and t) than in pure notch geometry (ρ and α). This result is due to the inherent stress dependence on the radial and axial location within the plate. A formulation for the location of minimum equivalent stress within a smooth plate was developed and it was observed that this location acts as a point of symmetry for stress distributions along the radius of the notch.

9. Future Work

The results presented in the current paper were solved assuming a series of idealizations and simplifications which provided a solid framework for the understanding of the complex relationships between the stresses in the vicinity of the notch tip and the notch geometry and location. Idealizations in the FEA such as static loading, isotropic material, elastic behavior, and isothermal conditions allow for only approximate solutions to be found, which cannot be readily applied to the service conditions of the component under consideration; therefore, future studies are planned which will employ further mechanical testing and advanced FEA to provide solutions more applicable to the actual application of circular v-notched components.

Future mechanical testing will consist of flexural experiments of notched, rectangular components to understand the effects of pure bending stresses on the fracture behavior. Additionally, flexural experiments will provide correlations between simple and axisymmetric bending. The tensile experiments conducted previously will be repeated with multiple tests at each configuration to provide statistical certainties associated with experimental results. Notched members will be tested at high strain rates to simulate the impact these plate components experience in service and to further quantify rate dependency of the mechanical properties and fracture behavior of Ultem 1000.

In regards to advanced FEA, elastic-plastic simulations will provide insights into the strain hardening effects on the maximum stresses in the vicinity of the notch. Also, elastic and plastic deformation distributions will be characterized within the vicinity of

the notch. Dynamic simulations will consider the rate dependence of Ultem 1000 and the resulting effects on the v-notch stress concentration factors and fracture behavior. Since in the industry application of guided projectiles the circular plate components are subject to extreme fluctuations in heat, future numerical simulations will incorporate the known thermal properties of Ultem 1000 and attempt to predict the resulting fracture behaviors. Finally, studies of similar materials such as Ultem variations or custom material blends will be conducted to determine an optimized material composition which will yield a more predictable and controllable fracture behavior.

Appendix A: Codes

A.1 Parametric ANSYS Input File (para_notch_plate.inp)

```
Finish
/Clear
/PREP7
/OUTPUT,junk,txt

! Specify initial, final, and increment values for parameters:

!X_ini=.5
!X_inc=.2
!X_fin=2.5
!DEP_ini=.1
!DEP_inc=.02
!DEP_fin=.3
ANG_ini=45
ANG_inc=9
ANG_fin=90
!RAD_ini=.02
!RAD_inc=.003
!RAD_fin=.05

i=1

!*DO,X_LOC_RD,X_ini,X_fin,X_inc
!*DO,DEP_NTCH,DEP_ini,DEP_fin,DEP_inc
*DO,ANG_NTCH,ANG_ini,ANG_fin,ANG_inc
!*DO,RAD_NTCH,RAD_ini,RAD_fin,RAD_inc
PARSAV,,parameters,txt
*IF,i,GT,1,THEN
finish
/clear
/PREP7
PARRES,,parameters,txt
*ENDIF

finish
/FILNAME, 4 Parameter Study
/title, 4 Parameter Study

/prep7
/OUTPUT,junk1,txt
!*************************************************************************************************************
*********
! Primary Function:
!
! This input file simulates a circular plate with a concentric v-notch on the top surface subject to a static, uniform,
! axisymmetric pressure load on the top surface. Multiple parameters are independently varied and corresponding
! results are output for further analysis to provide insight into the effect each parameter has on stress ditribution
! in the vicinity of the notch.
!
! Results:
!
! The results of this simulation are output to independently named text files and include the radial, hoop, and
! equivalent stresses in the vicinity of the notch and the deflection of the center of the plate.
!
! Parametric Setup:
!
! Four variables are independently varied through use of a DO LOOP, namely X_LOC_RD, DEP_NTCH, and ANG_NTCH, and
! RAD_NTCH. The results for each run are stored in individual text files:
!
! Output files:
!
! The results are output into individually named text files with the following naming convention:
!
! Plate Deflection Results:
        DEFLECTN_"X_LOC_RD"_"DEP_NTCH"_"ANG_NTCH"_"RAD_NTCH".txt
! Locations of nodes along notch tip:                NNLOC_"X_LOC_RD"_"DEP_NTCH"_"ANG_NTCH"_"RAD_NTCH".txt
! Component stresses along notch tip:                NCSTR_"X_LOC_RD"_"DEP_NTCH"_"ANG_NTCH"_"RAD_NTCH".txt
```

```
! Principal stresses along notch tip:                NPSTR_"X_LOC_RD"_"DEP_NTCH"_"ANG_NTCH"_"RAD_NTCH".txt
! Locations of nodes along vertical line:            VNLOC_"X_LOC_RD"_"DEP_NTCH"_"ANG_NTCH"_"RAD_NTCH".txt
! Component stresses along vertical line:            VCSTR_"X_LOC_RD"_"DEP_NTCH"_"ANG_NTCH"_"RAD_NTCH".txt
! Principal stresses along vertical line:            VPSTR_"X_LOC_RD"_"DEP_NTCH"_"ANG_NTCH"_"RAD_NTCH".txt
! Locations of nodes along horizontal line:          HNLOC_"X_LOC_RD"_"DEP_NTCH"_"ANG_NTCH"_"RAD_NTCH".txt
! Component stresses along horizontal line:          HCSTR_"X_LOC_RD"_"DEP_NTCH"_"ANG_NTCH"_"RAD_NTCH".txt
! Principal stresses along horizontal line:          HPSTR_"X_LOC_RD"_"DEP_NTCH"_"ANG_NTCH"_"RAD_NTCH".txt
!
!
! Meshing Scheme and other FEM Characteristics:
!
! This input file utilizes ANSYS "free meshing" and the element size is based on the "smart size" tool
! with refinement set to level 4. Extra mesh refinement exists along areas of interest, namely the notch tip,
! the outer circumferential boundary, and the inner axial boundary. Since this is an axisymmetric analysis, only
! one half of a 2D cross section of the disk need be modeled. B.C's are set appropriately to take advantage of symmetry.
! The PLANE82 8-Node element is used in this model. This analysis is modeled as static.
!
!
! Future Updates:
!
! 1. Modify code to simulate dynamice loading.
! 2. Modify code to simulate thermal loading.
! 3. Modify code to simulate elastic-plastic deformation.
!
!*********************************************************************************************************************
*********
! Author: Nathan Mutter
! ver. 3.4
! Date: 12/05/09
!*********************************************************************************************************************
*********
! List of Parameters and descriptions:
!*********************************************************************************************************************
*********
! Input Parameters (Define system and do not change)
! ---------------
! HT_PLATE        Thickness of the plate              [in]
! RD_PLATE        Radius of the plate                 [in]
! PRESSURE        Evenly distributed pressure         [psi]
! DENS_ULT    Density of Ultem 1000                   [lb/in^3]
!
! Varied Parameters
! ---------------
! X_LOC_RD        Radial distance of notch tip        [in]            (.1<X_LOC_RD<2.9)
! DEP_NTCH    Depth of the notch          [in]                (.1<DEP_NTCH<.4)
! ANG_NTCH        Angle of notch          [degrees]   (60<ANG_NTCH<120)
! RAD_NTCH    Radius of notch tip         [in]                (.03125<RAD_NTCH<.09375)
!
! Parameters Derived from Geometric Relationships
! ---------------------------------------------
! HT_NOTCH        Height of the notch tip                 [in]
! HT_RADIU        Height of the center of radius  [in]
! PHI             Half of angle of notch          [degrees]
!*********************************************************************************************************************
*********

PI = 3.14159265
*AFUN, DEG

X_LOC_RD = 1
ANG_NTCH = 60
DEP_NTCH = .15
RAD_NTCH = .035

HT_PLATE = .5               ! Thickness of the plate        [in]
RD_PLATE = 3                ! Radius of the plate           [in]
PRESSURE = 300              ! Evenly distributed pressure   [psi]

! Specify horizontal and vertical bands for stress distributions
X1=X_LOC_RD-.02
```

```
X2=X_LOC_RD+.02
Y1=DEP_NTCH-.02
Y2=DEP_NTCH+.02

! Geometric relationships
HT_NOTCH = HT_PLATE - DEP_NTCH
HT_RADIU = HT_NOTCH + RAD_NTCH
PHI = ANG_NTCH/2
l = DEP_NTCH*tan(PHI)              ! distance of corner keypoint from center line of notch tip
r_x = RAD_NTCH*cos(PHI)            ! x projection of the radius
r_y = RAD_NTCH*sin(PHI)            ! y projection of the radius
x = RD_PLATE - (X_LOC_RD + l)      ! distance from far end of disk to corner keypoint

! Keypoints
k, 1, 0.0,          0.0            ! keypoint located at (0.0, 0.0)
k, 2, RD_PLATE,     0
k, 3, RD_PLATE,     HT_PLATE
k, 4, 0,            HT_PLATE
k, 5, X_LOC_RD,     HT_RADIU
k, 6, X_LOC_RD,     HT_NOTCH
k, 7, X_LOC_RD + r_x, HT_RADIU - r_y
k, 8, X_LOC_RD - r_x, HT_RADIU - r_y
k, 9, X_LOC_RD + l,  HT_PLATE
k, 10, X_LOC_RD - l,  HT_PLATE


! Lines
L, 1, 2                            ! L1 connecting keypoints 1 and 2
L, 2, 3                            ! L2
L, 3, 9                            ! L3
L, 9, 7                            ! L4
L, 8, 10                           ! L5
L, 10, 4                           ! L6
larc, 8, 7, 5, RAD_NTCH            ! L7 arc centered at keypoint 5 with radius r connecting keypoints 8 and 7
L, 4, 1                            ! L8

! Areas
AL, all                            ! define an area bounded by all lines

ksel,all

! Element
ET,1,PLANE82                       ! axisymmetric structural element
KEYOPT,1,3,1                       ! turn on axisymmetric key option

! Material Properties of Ultem 100
MP, EX, 1, 420e3                   ! modulus of elasticicy (psi)
MP, PRXY, 1, .35                   ! poissons ratio
MP, DENS, 1, 0.046243              ! density (lb/in^3)


! Meshing of entire 2D cross section using free meshing and "smart sizing"
MSHAPE, 0, 2D                      ! mesh with quadrilateral-shaped elements
MSHKEY, 0                          ! free mesh
SMRTSIZE,3                         ! refinement level 3
AMESH, 1


! Refine Mesh
LREFINE, 4,5,1,2,4,,
LREFINE, 7,7,1,2,1,,               ! refine mesh along notch tip
!LREFINE, 2,2,1,1                  ! refine mesh along circumferential boundary
!LREFINE, 8,8,1,1                  ! refine mesh along axial boundary

! Boundary Conditions
LSEL,S,LINE,,2,2,1                 ! constrain movement in x direction for nodes on line 2 (circumferential boundary)
NSLL,S,1
D,ALL,UX,0
LSEL,ALL
LSEL,S,LINE,,2,2,1                 ! constrain movement in y direction for nodes along line 2 (circumferential boundary)
```

```
NSLL,S,1
D,ALL,UY,0
LSEL,ALL

! Loads
LSEL,S,LINE,,3,6,3                    ! select lines 3 and 6
NSLL,S,1                              ! select nodes associated with those lines
SF,all,PRES,PRESSURE                  ! apply uniform pressure load along top surface of plate
LSEL,all

! Output files containing node locations
LSEL,S,LINE,,7,7,1
NSLL,S,1
NWRITE,NNLOC_%X_LOC_RD%_%DEP_NTCH%_%ANG_NTCH%_%RAD_NTCH%_.txt,   ! outputs Cartesian location of
nodes along notch tip
!NSEL,S,LOC,X,X1,X2
!NWRITE,VNLOC_%X_LOC_RD%_%DEP_NTCH%_%ANG_NTCH%_%RAD_NTCH%_.txt,   ! outputs Cartesian location of
nodes along vertical line
!NSEL,S,LOC,Y,Y1,Y2
!NWRITE,HNLOC_%X_LOC_RD%_%DEP_NTCH%_%ANG_NTCH%_%RAD_NTCH%_.txt,   ! outputs Cartesian location of
nodes along horizontal line
LSEL,all
NSEL,all

FINISH
/SOLU
solve
FINISH

/POST1

! Create job names for each run for each output file
DEF_JOB = 'DEF_%X_LOC_RD%_%DEP_NTCH%_%ANG_NTCH%_%RAD_NTCH%_.txt'
NNLOC_JOB = 'NNLOC_%X_LOC_RD%_%DEP_NTCH%_%ANG_NTCH%_%RAD_NTCH%_.txt'
NCSTR_JOB = 'NCSTR_%X_LOC_RD%_%DEP_NTCH%_%ANG_NTCH%_%RAD_NTCH%_.txt'
NPSTR_JOB = 'NPSTR_%X_LOC_RD%_%DEP_NTCH%_%ANG_NTCH%_%RAD_NTCH%_.txt'
VNLOC_JOB = 'VNLOC_%X_LOC_RD%_%DEP_NTCH%_%ANG_NTCH%_%RAD_NTCH%_.txt'
VCSTR_JOB = 'VCSTR_%X_LOC_RD%_%DEP_NTCH%_%ANG_NTCH%_%RAD_NTCH%_.txt'
VPSTR_JOB = 'VPSTR_%X_LOC_RD%_%DEP_NTCH%_%ANG_NTCH%_%RAD_NTCH%_.txt'
HNLOC_JOB = 'HNLOC_%X_LOC_RD%_%DEP_NTCH%_%ANG_NTCH%_%RAD_NTCH%_.txt'
HCSTR_JOB = 'HCSTR_%X_LOC_RD%_%DEP_NTCH%_%ANG_NTCH%_%RAD_NTCH%_.txt'
HPSTR_JOB = 'HPSTR_%X_LOC_RD%_%DEP_NTCH%_%ANG_NTCH%_%RAD_NTCH%_.txt'

! Create index files for each output file set
*CFOPEN, INDEX_DEFLECTN,txt,,append
*VWRITE, DEF_JOB
%C
/OUTPUT,junk2,txt
*CFOPEN, INDEX_NNLOC,txt,,append
*VWRITE, NNLOC_JOB
%C
/OUTPUT,junk3,txt
*CFOPEN, INDEX_NCSTR,txt,,append
*VWRITE, NCSTR_JOB
%C
/OUTPUT,junk4,txt
*CFOPEN, INDEX_NPSTR,txt,,append
*VWRITE, NPSTR_JOB
%C
/OUTPUT,junk5,txt
!*CFOPEN, INDEX_VNLOC,txt,,append
!*VWRITE, VNLOC_JOB
!%C
!/OUTPUT,junk6,txt
!*CFOPEN, INDEX_VCSTR,txt,,append
!*VWRITE, VCSTR_JOB
!%C
!/OUTPUT,junk7,txt
!*CFOPEN, INDEX_VPSTR,txt,,append
!*VWRITE, VPSTR_JOB
```

```
!%C
!/OUTPUT,junk8,txt
!*CFOPEN, INDEX_HNLOC,txt,,append
!*VWRITE, HNLOC_JOB
!%C
!/OUTPUT,junk9,txt
!*CFOPEN, INDEX_HCSTR,txt,,append
!*VWRITE, HCSTR_JOB
!%C
!/OUTPUT,junk10,txt
!*CFOPEN, INDEX_HPSTR,txt,,append
!*VWRITE, HPSTR_JOB
!%C
!/OUTPUT,junk11,txt

! Deflection data
KSEL,S,KP,,4,4,1
NSLK,S
/OUTPUT,DEF_%X_LOC_RD%_%DEP_NTCH%_%ANG_NTCH%_%RAD_NTCH%_.txt  ! outputs y deflection of center of
plate for each run
PRNSOL,U,Y
/OUTPUT,junk12,txt

! Notch data
LSEL,S,LINE,,7,7,1
NSLL,S,1
/OUTPUT,NCSTR_%X_LOC_RD%_%DEP_NTCH%_%ANG_NTCH%_%RAD_NTCH%_.txt  ! outputs component stress data
along notch tip for each run
PRNSOL,S,COMP
/OUTPUT,NPSTR_%X_LOC_RD%_%DEP_NTCH%_%ANG_NTCH%_%RAD_NTCH%_.txt  ! outputs principle stress data along
notch tip for each run
PRNSOL,S,PRIN
/OUTPUT,junk13,txt
LSEL,all
NSEL,all

! Vertical range data
!NSEL,S,LOC,X,X1,X2
!/OUTPUT,VCSTR_%X_LOC_RD%_%DEP_NTCH%_%ANG_NTCH%_%RAD_NTCH%_.txt  ! outputs component stress data
along vertical band for each run
!PRNSOL,S,COMP
!/OUTPUT,VPSTR_%X_LOC_RD%_%DEP_NTCH%_%ANG_NTCH%_%RAD_NTCH%_.txt  ! outputs principal stress data
along vertical band for each run
!PRNSOL,S,PRIN
!/OUTPUT,junk14,txt
!LSEL,all
!NSEL,all

! Horizontal range data
!NSEL,S,LOC,Y,Y1,Y2
!/OUTPUT,HCSTR_%X_LOC_RD%_%DEP_NTCH%_%ANG_NTCH%_%RAD_NTCH%_.txt  ! outputs component stress data
along horizontal band for each run
!PRNSOL,S,COMP
!/OUTPUT,HPSTR_%X_LOC_RD%_%DEP_NTCH%_%ANG_NTCH%_%RAD_NTCH%_.txt  ! outputs principal stress data
along horizontal band for each run
!PRNSOL,S,PRIN
!/OUTPUT,junk15,txt
!LSEL,all
!NSEL,all


PLDISP,0
PLESOL,S,X,0

i=i+1
FINISH
*ENDDO
!*ENDDO
!*ENDDO
!*ENDDO
```

A.2 FORTRAN Data Extractor Code (data_extract.f90)

```
program data_extractor

!!!!!!!!!!!!!!!!!!!!!!!!!!!!!!!!!!!!!!!!!!!!!!!!!!!!!!!!!!!!!!!!!!!!!!!!!!!!!!!!
! Program Function:
! This program extracts results from simulation output files and writes the
! data in tabulated format to one output file.
!
! Author: Nathan Mutter
! Date:   2-20-2010
! Version: 1.3
!
! Future Updates:
!   1.
!   2.
!!!!!!!!!!!!!!!!!!!!!!!!!!!!!!!!!!!!!!!!!!!!!!!!!!!!!!!!!!!!!!!!!!!!!!!!!!!!!!!!

! Array and variable declaration:

          character*40, dimension (700) :: NCSTR_JOB
          character*40, dimension (700) :: NPSTR_JOB
          character*40, dimension (700) :: DEFLECTN_JOB
          character(len=80) line
          character(len=80) line_clean_c
          character(len=80) line_clean_p
          character(len=80) line_clean_d
          integer :: job_num, job_num_max
          real :: MX_RAD_STRES, MX_AXI_STRES, MX_HOP_STRES, MX_PRIN_STRES, MX_EQ_STRES, DEFLECTN,
MX_SHR_STRES


! Determine number of files to be read and store as job_num_max:

          open (1, file='INDEX_NCSTR.txt', status='old')
          job_num_max=0
          do
          read(1,100,iostat=io)
          if (io .eq. -1) then
          go to 1
          else
          job_num_max = job_num_max+1
          endif
          end do
1         continue

          close(1)

! Create job name arrays from each job name index file:

          ! INDEX_NCSTR
          do job_num=1,job_num_max
          open (2, file='INDEX_NCSTR.txt', status='old')
          read (2,100) line
          NCSTR_JOB(job_num)=line
          enddo

          ! INDEX_NPSTR
          do job_num=1,job_num_max
          open (3, file='INDEX_NPSTR.txt', status='old')
          read (3,100) line
          NPSTR_JOB(job_num)=line
          enddo
```

```
        ! INDEX_DEFLECTN
        do job_num=1,job_num_max
        open (4, file='INDEX_DEFLECTN.txt', status='old')
        read (4,100) line
        DEFLECTN_JOB(job_num)=line
        enddo

        close(2)
        close(3)
        close(4)

! Open individual simulation results files, extract data of interest
! and store in arrays:

! Open component stress result files and extract the max Radial, Axial
! Hoop and Shear stresses.
        do job_num =1,job_num_max
                open(6,file=NCSTR_JOB(job_num),status='old')
2               read (6,100,end=3) line_clean_c
      if (line_clean_c(2:4).eq.'MAX') then
                                read (6,100) junk
                                read (6,110) MX_RAD_STRES, MX_AXI_STRES, MX_HOP_STRES,
MX_SHR_STRES
                                continue
                 else
                                goto 2
                        end if
3               continue

! Open principle stress result files and extract the max first principle stress.

                open(7,file=NPSTR_JOB(job_num),status='old')
4    read (7,100,end=5) line_clean_p
      if (line_clean_p(2:4).eq.'MAX') then
                                read (7,100) junk
                                read (7,120) MX_PRIN_STRES, MX_EQ_STRES
                                continue
                 else
                                goto 4
                        end if
5               continue

! Open deflection result files and extract deflection of center plate.

                open (8, file=DEFLECTN_JOB(job_num), status='old')
6               read (8,100,end=7) line_clean_d
      if (line_clean_d(2:4).eq.'MAX') then
                                read (8,100) junk
                                read (8,130) DEFLECTN
                                continue
                 else
                                goto 6
                        end if
7               continue

! Write data in tabulated form to an output file:

        open (9, file='CLEAN_DATA.txt', status='unknown')
        write (9,140) DEFLECTN_JOB(job_num)(5:30), MX_RAD_STRES, MX_AXI_STRES, &
&                                       MX_HOP_STRES, MX_SHR_STRES, MX_PRIN_STRES, MX_EQ_STRES,
DEFLECTN
        enddo

        ! Formats

100     format(a80)
110 format(8X F10.2,1X F10.2, 3X F10.2, 2X F10.2)
120     format (7X F10.2,41X F10.2)
130     format (8X F7.3)
```

```
140     format (a25,7(6X F10.3))

        close(6)
        close(7)
        close(8)
        close(9)


        end
```

A.3 FORTRAN Stress Distribution Code (stress_dist.f90)

```
program stress_distributions

!!!!!!!!!!!!!!!!!!!!!!!!!!!!!!!!!!!!!!!!!!!!!!!!!!!!!!!!!!!!!!!!!!!!!!!!
! Program Function:
! This program extracts shear stress and von Mises stress values from nodes along
! the radius of the notch and converts the nodal Cartesian coordinates into
! polar coordinates centered above the notch tip with a constant radius equal to
! the notch tip radius.  This program also extracts shear and von Mises stress
! values from nodes along a vertical line from the notch tip to the bottom of the
! plate.  The stresses and nodal locations for both the angular and vertical
! distribution cases are written to separate text files for each parametric
! combination.
!
! Author:  Nathan Mutter
! Date:    2-27-2010
! Version: 1.0
!
! Future Updates:
!
!
!
!
!!!!!!!!!!!!!!!!!!!!!!!!!!!!!!!!!!!!!!!!!!!!!!!!!!!!!!!!!!!!!!!!!!!!!!!!

! Array and variable declaration


! If varying X_LOC_RD:
!REAL,PARAMETER :: X_INI=0.5, X_FIN=2.5, X_INC=0.2
!REAL,PARAMETER :: X_SIZE=((X_FIN-X_INI)/X_INC)+1
!REAL,DIMENSION(1:X_SIZE) :: X_LOC_RD
REAL :: RAD_NTCH

! If varying RAD_NTCH:
!REAL,PARAMETER :: RAD_INI=0.02, RAD_FIN=0.05, RAD_INC=0.003
!REAL,PARAMETER :: RAD_SIZE=((RAD_FIN-RAD_INI)/RAD_INC)+1
!REAL,DIMENSION(1:RAD_SIZE) :: RAD_NTCH
REAL :: X_LOC_RD

CHARACTER*40, DIMENSION(100) :: NCSTR_JOB, NPSTR_JOB, C_NCSTR_JOB, &
            C_NPSTR_JOB, NNLOC_JOB, VCSTR_JOB, VPSTR_JOB, C_VCSTR_JOB, C_VPSTR_JOB, &
            VNLOC_JOB, ANG_DIST_JOB, VERT_DIST_JOB
CHARACTER (len=80) :: line
INTEGER :: job_num, job_num_max, NODE_NUM, NNLOC_NODE, NPSTR_NODE, VNLOC_NODE, &
                                    VPSTR_NODE
REAL :: X_COORD, Y_COORD, ANG_SEQV, ANG_SHEAR, ANG_SINT, ANG_MX_SHEAR, ANGLE, VERT_SEQV, &
                        VERT_SINT, VERT_MX_SHEAR, VERT_SHEAR


!!!!!!!!!!!!!!!!!!!!!!!!!!!!!!!!!!!!!!!!!!!!!!!!!!!!!!!!!!!!!!!!!!!!!!!!

! Determine number of jobs to be read based on index file:

            open (1, file='INDEX_NCSTR.txt', status='old')
            job_num_max=0
            do
            read(1,100,iostat=io)
            if (io .eq. -1) then
            go to 1
            else
            job_num_max=job_num_max+1
```

```
        endif
        end do
1       continue

        close(1)

!!!!!!!!!!!!!!!!!!!!!!!!!!!!!!!!!!!!!!!!!!!!!!!!!!!!!!!!!!!!!!!!!!!!!!
! Define geometric parameters neccessary for angular coordinate calculation:
!  1. If varying the DEP_NTCH or ANG_NTCH then X_LOC_RD and RAD_NTCH are
!                   constants and the below do loop declarations are not neccessary.
!  2.       If varying X_LOC_RD then RAD_NTCH is constant.
!           3.          If varying RAD_NTCH then X_LOC_RD is constant.
!           4.          Depending on which notch parameters are being varied, the correct "ANGLE"
!    formula must be chosen in the body of the code (see ***).
!!!!!!!!!!!!!!!!!!!!!!!!!!!!!!!!!!!!!!!!!!!!!!!!!!!!!!!!!!!!!!!!!!!!!!
!
! VARY X_LOC_RD:

RAD_NTCH=.035

!do i=1,job_num_max
!X_LOC_RD(i)=X_INI+((i-1)*X_INC)
!enddo



!               OR


! VARY NTCH_RAD:

X_LOC_RD=1

!do i=1,job_num_max
!RAD_NTCH(i)=RAD_INI+((i-1)*RAD_INC)
!enddo

!!!!!!!!!!!!!!!!!!!!!!!!!!!!!!!!!!!!!!!!!!!!!!!!!!!!!!!!!!!!!!!!!!!!!!


! Create job name arrays from each job name index file:

! INDEX_NCSTR
        do job_num=1,job_num_max
        open (2, file='INDEX_NCSTR.txt',status='old')
        read (2,100) line
        NCSTR_JOB(job_num)=line
        enddo

! INDEX_NPSTR
        do job_num=1,job_num_max
        open (3, file='INDEX_NPSTR.txt',status='old')
        read (3,100) line
        NPSTR_JOB(job_num)=line
        enddo

! INDEX_NNLOC
        do job_num=1,job_num_max
        open (4, file='INDEX_NNLOC.txt',status='old')
        read (4,100) line
        NNLOC_JOB(job_num)=line
        enddo

! INDEX_VCSTR
        do job_num=1,job_num_max
        open (6, file='INDEX_VCSTR.txt',status='old')
        read (6,100) line
        VCSTR_JOB(job_num)=line
        enddo
```

```
! INDEX_VPSTR
            do job_num=1,job_num_max
            open (7, file='INDEX_VPSTR.txt',status='old')
            read (7,100) line
            VPSTR_JOB(job_num)=line
            enddo

! INDEX_VNLOC
            do job_num=1,job_num_max
            open (8, file='INDEX_VNLOC.txt',status='old')
            read (8,100) line
            VNLOC_JOB(job_num)=line
            enddo

!!!!!!!!!!!!!!!!!!!!!!!!!!!!!!!!!!!!!!!!!!!!!!!!!!!!!!!!!!!!!!!!!!!!!!!!!!!!!!!!

! Clean stress files and rename:

do job_num=1,job_num_max

            open(unit=9, file=NCSTR_JOB(job_num), status='old')
            open(unit=10,file='C_'//NCSTR_JOB(job_num), status='unknown')
            do while (.true.)
  read (9,100,end=5) line
  do i=1,80
       if (line(i:i).eq.' ') goto 2
       if (line(i:i).eq.'0') goto 4
       if (line(i:i).eq.'1') goto 4
       if (line(i:i).eq.'2') goto 4
       if (line(i:i).eq.'3') goto 4
       if (line(i:i).eq.'4') goto 4
       if (line(i:i).eq.'5') goto 4
       if (line(i:i).eq.'6') goto 4
       if (line(i:i).eq.'7') goto 4
       if (line(i:i).eq.'8') goto 4
       if (line(i:i).eq.'9') goto 4
       goto 3
4      continue
       write (10,100) line
       goto 3
2      continue
     enddo
3    continue
   enddo
5  continue

            open(unit=11, file=NPSTR_JOB(job_num), status='old')
            open(unit=12,file='C_'//NPSTR_JOB(job_num), status='unknown')
            do while (.true.)
  read (11,100,end=9) line
  do i=1,80
       if (line(i:i).eq.' ') goto 6
       if (line(i:i).eq.'0') goto 8
       if (line(i:i).eq.'1') goto 8
       if (line(i:i).eq.'2') goto 8
       if (line(i:i).eq.'3') goto 8
       if (line(i:i).eq.'4') goto 8
       if (line(i:i).eq.'5') goto 8
       if (line(i:i).eq.'6') goto 8
       if (line(i:i).eq.'7') goto 8
       if (line(i:i).eq.'8') goto 8
       if (line(i:i).eq.'9') goto 8
       goto 7
8      continue
       write (12,100) line
       goto 7
6      continue
     enddo
7    continue
   enddo
```

```
9   continue


            open(unit=13, file=VCSTR_JOB(job_num), status='old')
            open(unit=14,file='C_'//VCSTR_JOB(job_num), status='unknown')
            do while (.true.)
    read (13,100,end=13) line
    do i=1,80
        if (line(i:i).eq.' ') goto 10
        if (line(i:i).eq.'0') goto 12
        if (line(i:i).eq.'1') goto 12
        if (line(i:i).eq.'2') goto 12
        if (line(i:i).eq.'3') goto 12
        if (line(i:i).eq.'4') goto 12
        if (line(i:i).eq.'5') goto 12
        if (line(i:i).eq.'6') goto 12
        if (line(i:i).eq.'7') goto 12
        if (line(i:i).eq.'8') goto 12
        if (line(i:i).eq.'9') goto 12
        goto 11
12      continue
        write (14,100) line
        goto 11
10      continue
      enddo
11    continue
    enddo
13  continue

            open(unit=15, file=VPSTR_JOB(job_num), status='old')
            open(unit=16,file='C_'//VPSTR_JOB(job_num), status='unknown')
            do while (.true.)
    read (15,100,end=17) line
    do i=1,80
        if (line(i:i).eq.' ') goto 14
        if (line(i:i).eq.'0') goto 16
        if (line(i:i).eq.'1') goto 16
        if (line(i:i).eq.'2') goto 16
        if (line(i:i).eq.'3') goto 16
        if (line(i:i).eq.'4') goto 16
        if (line(i:i).eq.'5') goto 16
        if (line(i:i).eq.'6') goto 16
        if (line(i:i).eq.'7') goto 16
        if (line(i:i).eq.'8') goto 16
        if (line(i:i).eq.'9') goto 16
        goto 15
16      continue
        write (16,100) line
        goto 15
14      continue
      enddo
15    continue
    enddo
17  continue

enddo

close(2)
close(3)
close(4)
close(6)
close(7)
close(8)
close(9)
close(10)
close(11)
close(12)
close(13)
close(14)
close(15)
```

```
close(16)

!!!!!!!!!!!!!!!!!!!!!!!!!!!!!!!!!!!!!!!!!!!!!!!!!!!!!!!!!!!!!!!!!!!!!!!!!!!!!

! Extract SEQV, shear stress, and X_COORD of the nodes along notch radius.  Convert
! to angular location around radius of notch and write to ANG_DIST.txt.


do job_num=1,job_num_max

        do while (.true.)

                open(2,file='C_'//NCSTR_JOB(job_num),status='old')
                open(3,file='C_'//NPSTR_JOB(job_num),status='old')
                open(4,file=NNLOC_JOB(job_num),status='old')

                read(2,110,end=25) NODE_NUM, ANG_SHEAR

18              read(3,120,end=19) NPSTR_NODE, ANG_SINT, ANG_SEQV
                        if (NPSTR_NODE .eq. NODE_NUM) then
                        go to 20
                        else
                        go to 18
                        endif
19              print*, 'Node number not found'
20              continue
                ANG_MX_SHEAR=ANG_SINT/2

21              read(4,130,end=22) NNLOC_NODE, X_COORD
                        if (NNLOC_NODE .eq. NODE_NUM) then
                        go to 23
                        else
                        go to 21
                        end if
22              print*, 'Node number not found'
23              continue

! ********************************************************************************
!!!!!!!!!!!!!!!!!!!!!!!!!!!!!!!!!!!!!!!!!!!!!!!!!!!!!!!!!!!!!!!!!!!!!!!!!!!!!!!!
! Convert cartesian coordinates into polar:
!
! Depending on which parameters of the notch are being varied, choose the
! appropriate "ANGLE" statement below and "comment" out the other two:


! If varying DEP_NTCH or ANG_NOTCH, use below statement:

ANGLE=ASIN((X_COORD-X_LOC_RD)/RAD_NTCH)*(180/3.1416)

! If varying X_LOC_RD, use below statement:

!ANGLE=ASIN((X_COORD-X_LOC_RD(job_num))/RAD_NTCH)*(180/3.1416)

! If varying RAD_NTCH, use below statement:

!ANGLE=ASIN((X_COORD-X_LOC_RD)/RAD_NTCH(job_num))*(180/3.1416)

!!!!!!!!!!!!!!!!!!!!!!!!!!!!!!!!!!!!!!!!!!!!!!!!!!!!!!!!!!!!!!!!!!!!!!!!!!!!!!!!
! ********************************************************************************

! Write ANG_DIST text files for each job:
open(6,file='ANG_DIST_'//NCSTR_JOB(job_num),status='unknown')
write(6,140) NODE_NUM, X_COORD, ANGLE, ANG_SHEAR, ANG_MX_SHEAR, ANG_SEQV

        enddo

25      continue

enddo
```

```
close(2)
close(3)
close(4)
close(6)
!!!!!!!!!!!!!!!!!!!!!!!!!!!!!!!!!!!!!!!!!!!!!!!!!!!!!!!!!!!!!!!!!!!!!!!!!!

! Extract SEQV, shear stress, and Y_COORD of the nodes along a vertical line from
! the notch tip to the bottom of the plate and write results to VERT.DIST.txt.

do job_num=1,job_num_max

        do while (.true.)

                open(2,file='C_'//VCSTR_JOB(job_num),status='old')
                open(3,file='C_'//VPSTR_JOB(job_num),status='old')
                open(4,file=VNLOC_JOB(job_num),status='old')

                read(2,110,end=30) NODE_NUM, VERT_SHEAR

38              read(3,120,end=31) VPSTR_NODE, VERT_SINT, VERT_SEQV
                        if (VPSTR_NODE .eq. NODE_NUM) then
                        go to 40
                        else
                        go to 38
                        endif
39              print*, 'Node number not found'
40              continue
                VERT_MX_SHEAR=VERT_SINT/2

31              read(4,150,end=32) VNLOC_NODE, Y_COORD
                        if (VNLOC_NODE .eq. NODE_NUM) then
                        go to 33
                        else
                        go to 31
                        end if
32              print*, 'Node number not found'
33              continue


! Write VERT_DIST text files for each job:
open(6,file='VERT_DIST_'//NCSTR_JOB(job_num),status='unknown')
write(6,160) NODE_NUM, Y_COORD, VERT_SHEAR, VERT_MX_SHEAR, VERT_SEQV

        enddo

30      continue

enddo


!!!!!!!!!!!!!!!!!!!!!!!!!!!!!!!!!!!!!!!!!!!!!!!!!!!!!!!!!!!!!!!!!!!!!!!!!!

! Formats:

100 format(a80)
110 format(4X I4, 36X F10.2)
120 format(4X I4, 38X F9.2,3X F9.2)
130 format(4X I4, 2X F10.8)
140 format(I4,5X F8.5,4(5X F8.2))
150 format(4X I4, 20X F20.17)
160 format(I4,5X F8.5,3(5X F8.2))
!!!!!!!!!!!!!!!!!!!!!!!!!!!!!!!!!!!!!!!!!!!!!!!!!!!!!!!!!!!!!!!!!!!!!!!!!!


end
```

Appendix B: Mechanical Testing Photographs and Fractographs

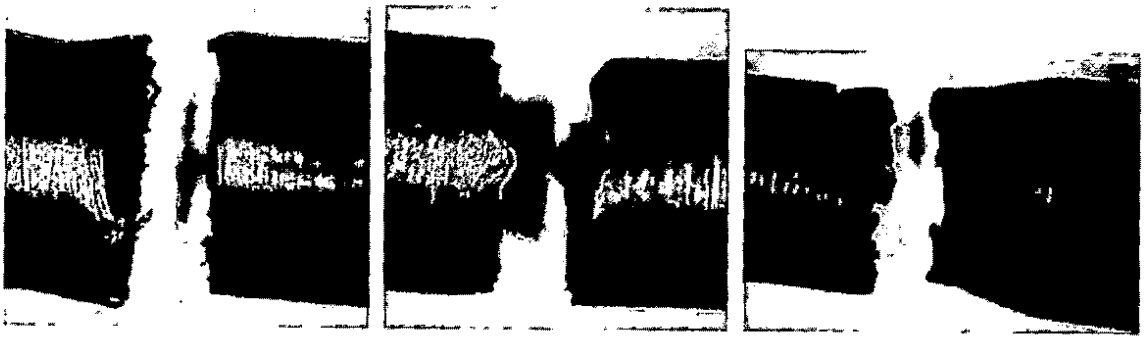

(a) (b) (c)

Figure B.1. Side view of fracture surfaces of smooth specimens from tensile experiments at (a) 0.5 mm/s, (b) 0.05 mm/s, and (c) 0.005 mm/s.

(a) (b) (c)

Figure B.2. Isometric view of fracture surfaces of smooth specimens from tensile experiments at (a) 0.5 mm/s, (b) 0.05 mm/s, and (c) 0.005 mm/s.

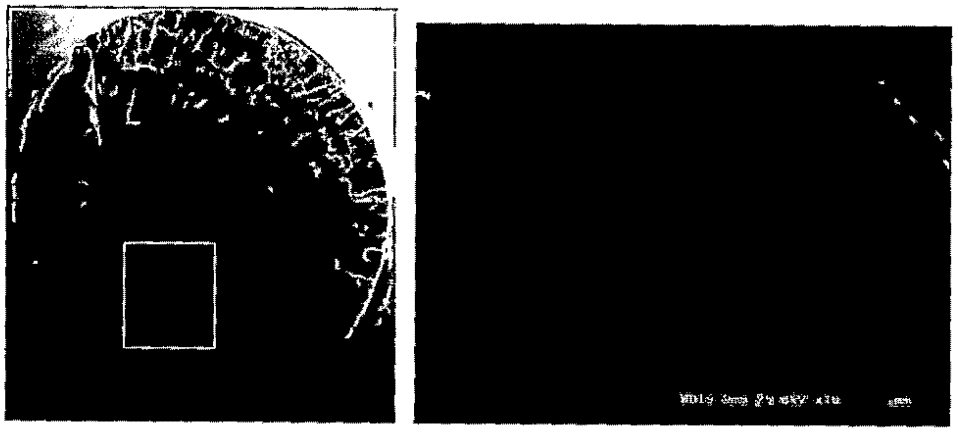

Figure B.3. SEM fractograph of smooth specimen from tensile test at 0.5 mm/s.

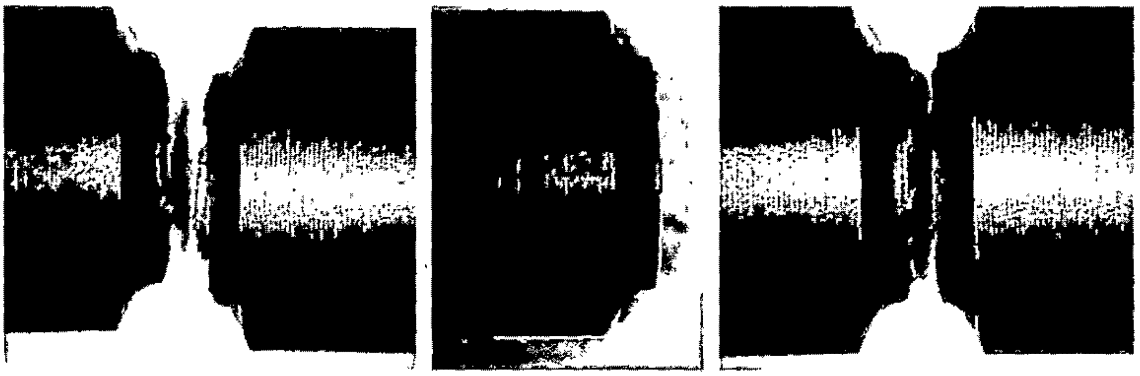

(a) (b) (c)

Figure B.4. Side view of fracture surfaces of blunt notched specimens from tensile experiments at (a) 0.5 mm/s, (b) 0.05 mm/s, and (c) 0.005 mm/s.

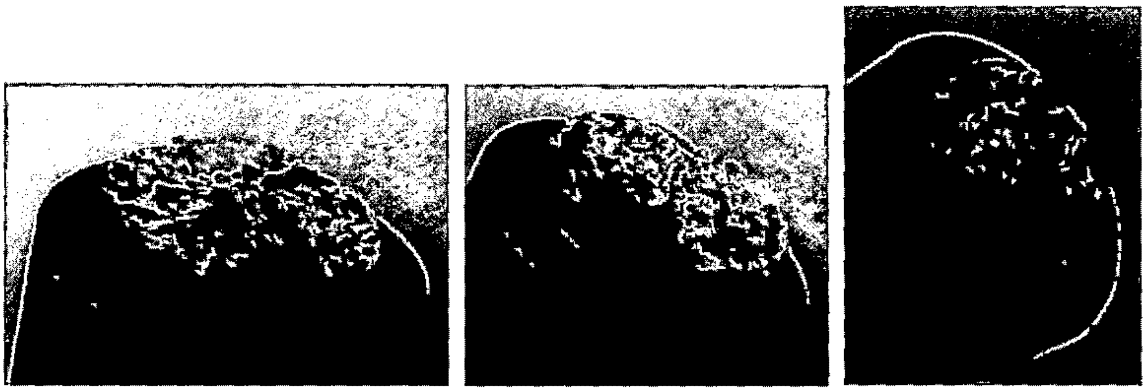

(a) (b) (c)

Figure B.5. Isometric view of fracture surfaces of blunt notched specimen from tensile experiments at (a) 0.5 mm/s, (b) 0.05 mm/s, and (c) 0.005 mm/s.

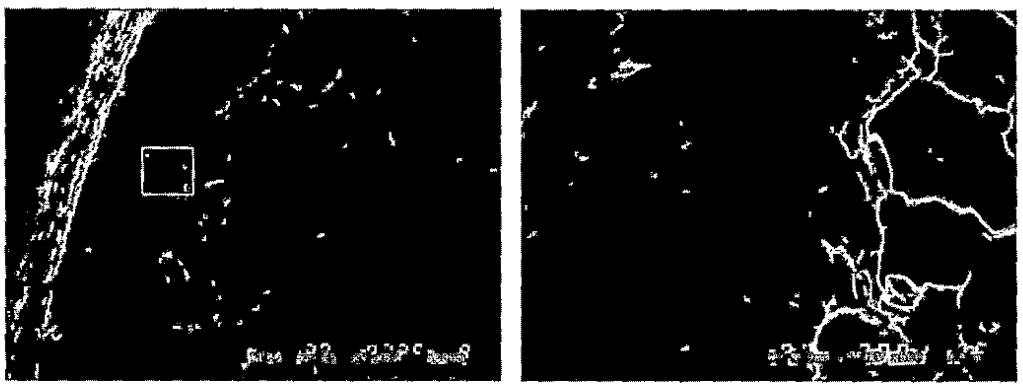

Figure B.6. SEM fractographs showing smooth ridge of blunt notched specimen tested at 0.5 mm/s.

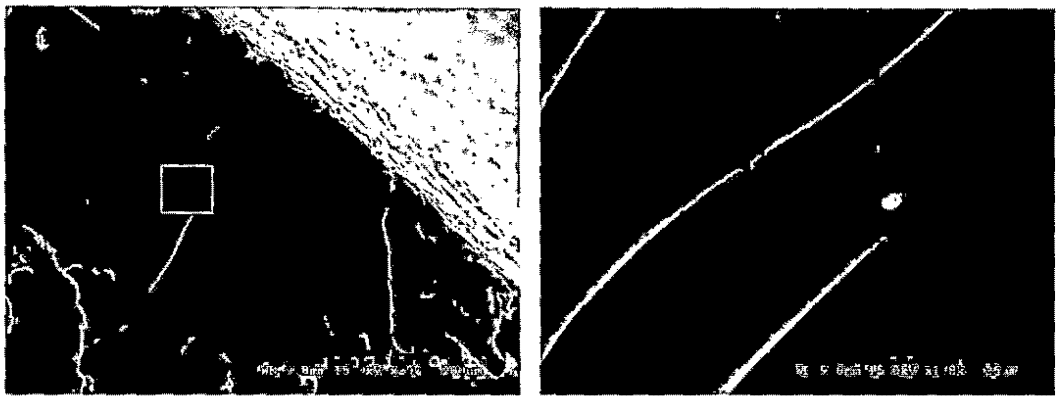

Figure B.7. SEM fractographs showing crack initiation of blunt notched specimen tested at 0.5 mm/s.

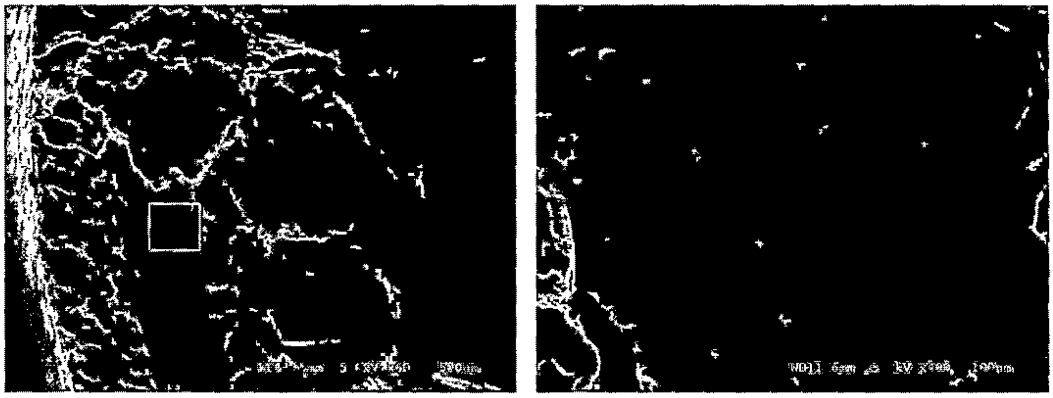

Figure B.8. SEM fractographs showing smooth ridge of blunt notched specimen tested at 0.05 mm/s.

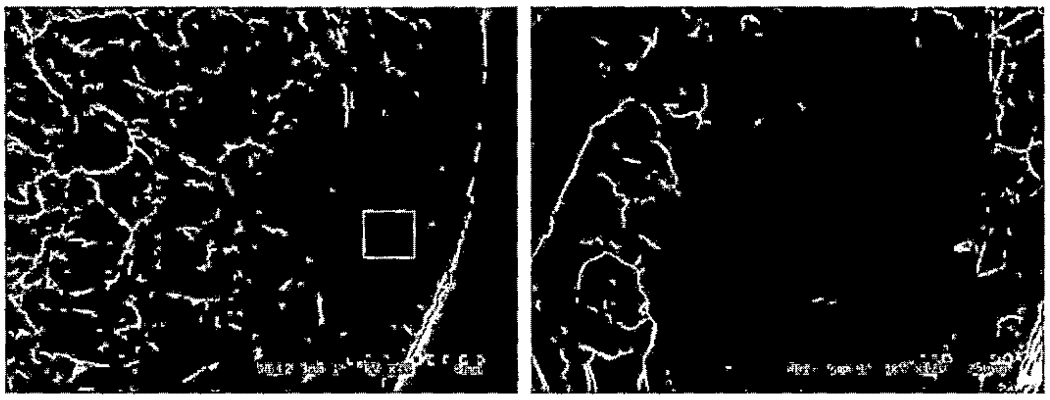

Figure B.9. SEM fractographs showing crack initiation of blunt notched specimen tested at 0.05 mm/s.

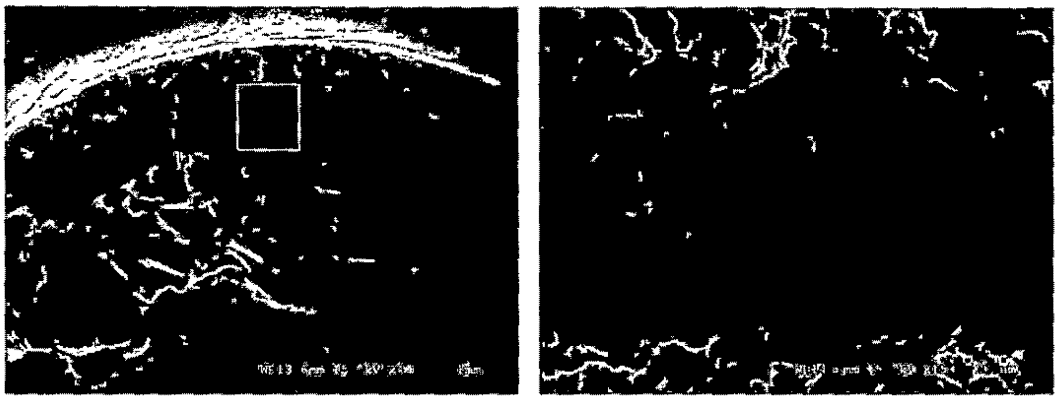

Figure B.10. SEM fractographs showing smooth ridge of blunt notched specimen tested at 0.005 mm/s.

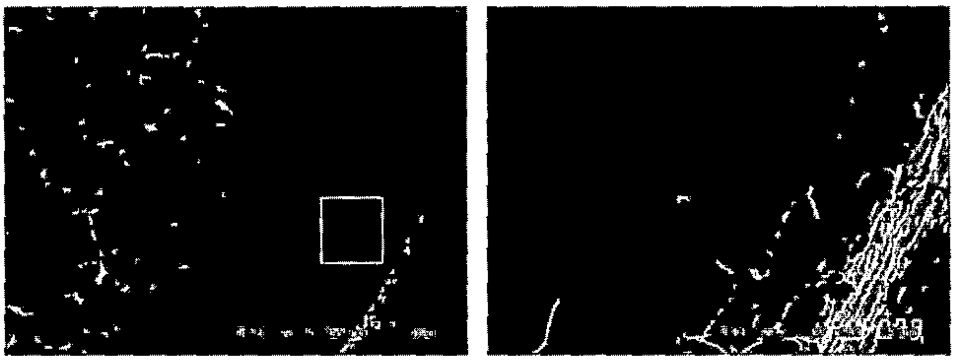

Figure B.11. SEM fractographs showing crack initiation of blunt notched specimen tested at 0.005 mm/s.

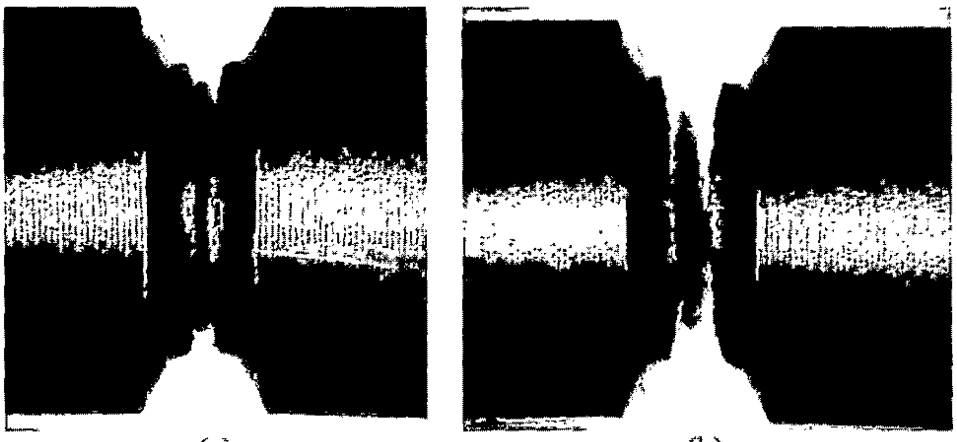

(a) (b)

Figure B.12. Side view of fracture surfaces of sharp notched specimens from tensile experiments at (a) 0.5 mm/s and (b) 0.05 mm/s.

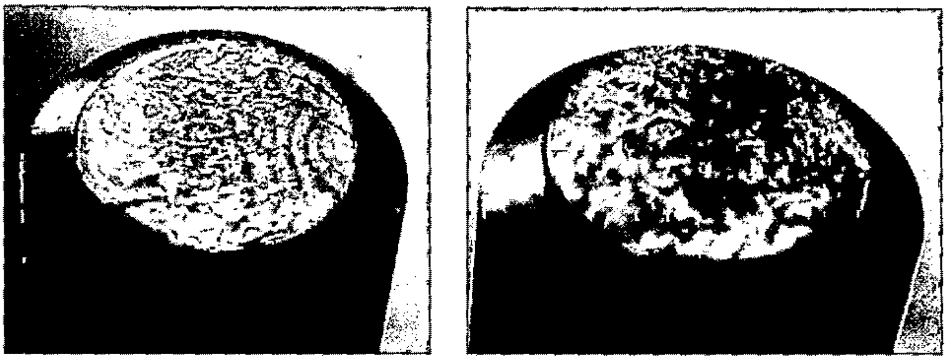

(a) (b)

Figure B.13. Isometric view of fracture surfaces of sharp notched specimens from tensile experiments at (a) 0.5 mm/s and (b) 0.05 mm/s.

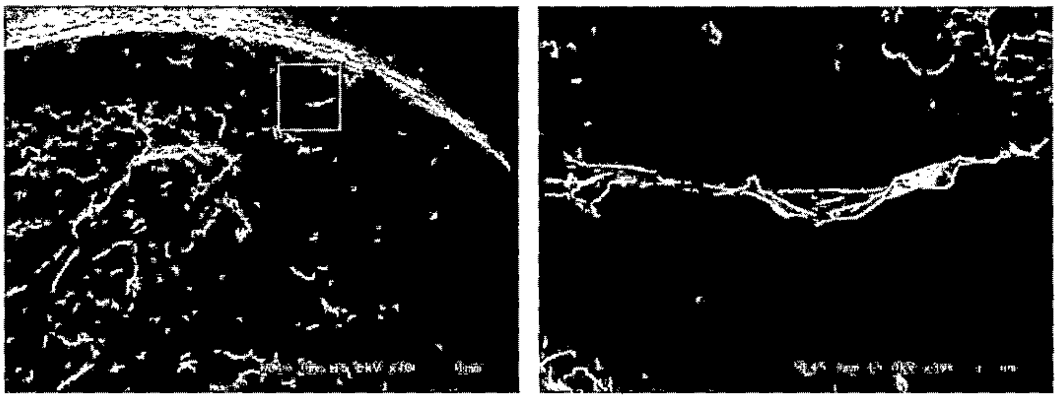

Figure B.14. SEM fractographs showing smooth ridge of sharp notched specimen tested at 0.5 mm/s.

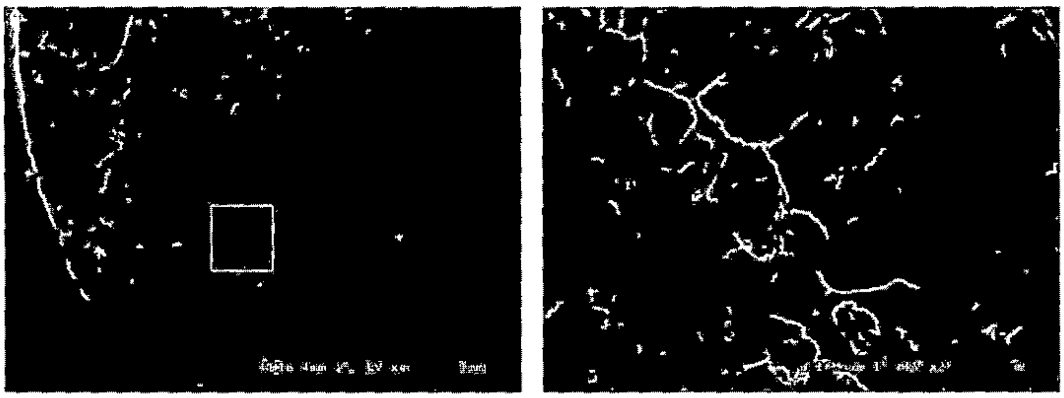

Figure B.15. SEM fractographs showing crack initiation of sharp notched specimen tested at 0.5 mm/s.

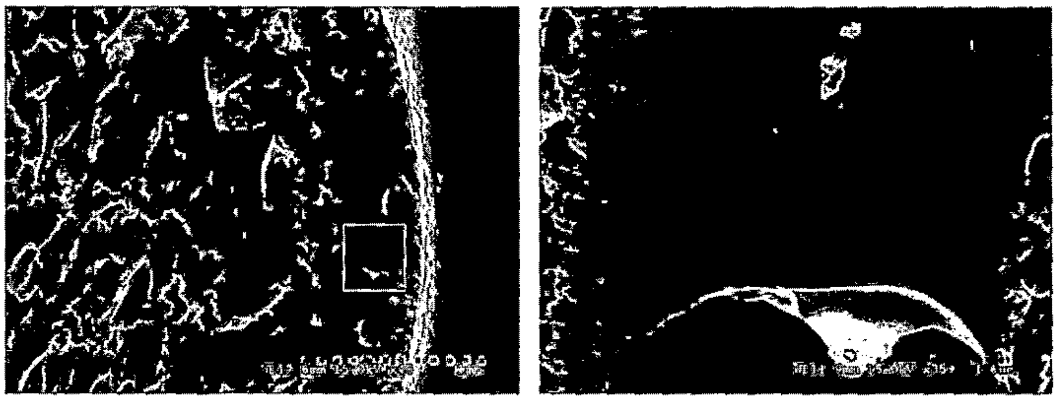

Figure B.16. SEM fractographs showing smooth ridge of sharp notched specimen tested at 0.05 mm/s.

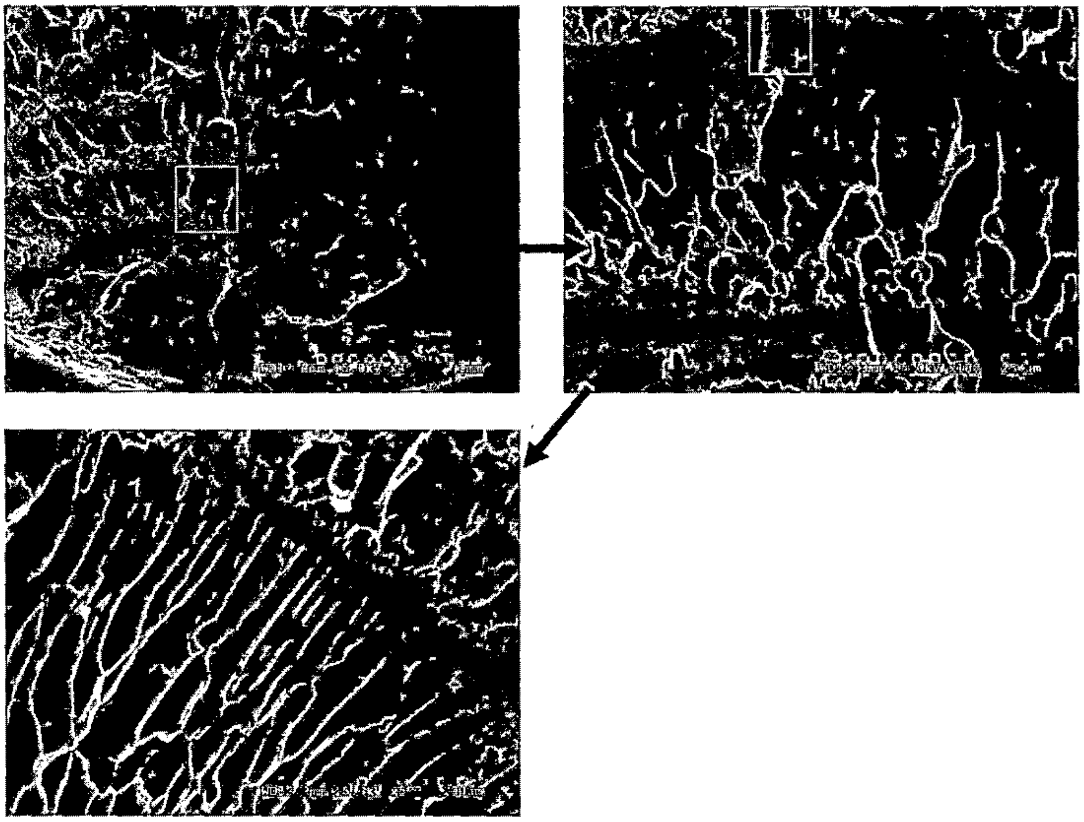

Figure B.17. SEM fractographs showing crack initiation of sharp notched specimen tested at 0.05 mm/s.

References

1. Apple, F. J., and Koerner, D. R. "Stress Concentration Factors for U-Shaped, Hyperbolic and Rounded V-Shaped Notches." ASME Paper 69-DE-2, Eng. Soc. Library, United Eng. Center, New York. (1969).
2. Bijwe, J., Tewari, U. S., and Vasudevan, P. "Friction and Wear Studies of Bulk Polyetherimide." *Journal of Materials Science,* 25(1) (1991): 548-556.
3. Bordonaro, C. M., and Krempi, E. "The Rate-Dependent Mechanical Behavior of Plastics: A Comparison between 6/6 Nylon, Polyetherimide and Polyetheretherketone." *Proceedings – 1993 American Society of Mechanical Engineers Winter Annual Meeting,* New Orleans, LA. November 28 – December 3.
4. Facca, A. G., Kortschot, M. T., and Yan, N. "Predicting the Tensile Strength of Natural Fibre Reinforced Thermoplastics." *Composites Science and Technology,* 67(6) (2007): 2454-2466.
5. Greenhalgh, E. S., *Failure Analysis and Fractography of Polymer Composites.* Boca Raton: Woodhead Publishing Limited, 2009.
6. Inglis, C. E. "Stresses in a Plate Due to the Presence of Cracks and Sharp Corners." *Trans. Inst. Naval Architects*, A221 (1913): 219-230.
7. Johnson, R., and Jafry, S. "Ultem Polyetherimide Resin for the Medical Industry." *Proceedings – Society of Petroleum Engineers Annual Western Regional Meeting,* (1998). Anaheim, CA. January 19-22.

8. Kim, K., and Ye, L. "Effects of Thickness and Environmental Temperature on Fracture Behavior of Polyetherimide (PEI)." *Journal of Materials Science,* 39(4) (2004): 1267-1376.

9. Leven, M. M., and Frocht, M. M. "Stress Concentration Factors for a Single Notch in a Flat Plate in Pure and Central Bending." *Proc. System Engineering Society of Australia,* 11(2) (1953): 179.

10. Neuber, H. *Kerbspannungslehre,* 2nd ed. Berlin: Springer, 1958; Translation, *Theory of Notch Stresses*, Washington, D.C.: Office of Technical Services, Dept. of Commerce, 1961.

11. Noda, N. A., and Takase, Y. "Stress concentration formulae useful for any shape of notch in a round test specimen under tension and under bending." *Fatigue and Fracture of Engineering Materials and Structures*, 22(12) (1999): 1071-1082.

12. Pecht, M., and Wu, X. "Characterization of Polyimides Used in GE-High Density Interconnects." *International Society for the Advancement of Material and Process Engineering Electronics Conference,* 7.2 (1994): 432-445. Parsippany, NJ. June 20-23.

13. Pilkey, W. D. *Peterson's Stress Concentration Factors Second Edition.* New York: Wiley-Interscience, 1997.

14. Reddy, J. N. *Theory and Analysis of Elastic Plates.* Philadelphia, PA: Taylor & Francis, 1999.

15. Rodriguez, J. E., Brennan, F. P., and Dover, W. D. "Minimization of Stress Concentration Factors in Fatigue Crack Repairs." *International Journal of Fatigue,* 20(10) (1998): 719-725.

16. SABIC Innovative Plastics Ultem 1000 Data Sheet. Retrieved June 15, 2008, from <http://www.matweb.com/search/datasheet.aspx?matguid=4b8cf67e11ee4c08aee413e45643f956&ckck=1>

17. Savage, T. "Ultem Resin Plays a Dual Cost Saving and Safety Role in Aviation." *Aircraft Engineering and Aerospace and Technology,* 60(4) (1988): 24-25.

18. Schmidt, R. "Finite Axisymmetric Deflections of a Loosely Clamped Circular Plate Subjected to a Two-Parameter Distributed Load." *The Journal of Industrial Mathematics Society,* 34(1) (1984): 89-98.

19. Schobig, M., Bierogel, C., Grellmann, W., and Mecklenburg, T. "Mechanical Behavior of Glass-Fiber Reinforced Thermoplastic Materials Under High Strain Rates." *Polymer Testing*, 27(7) (2008): 893-900.

20. Smmazcelik, T., Coban, O., Bora, M. O., Gunay, V., and Curgul, I. "The Effects of Thermal Cycles on the Impact Fatigue Properties of Thermoplastic Matrix Composites." *Applied Composite Materials,* 15(2) (2008): 99-113.

21. Stokes, V., and Nied, H. "Lateral Strain Effects During the Large Extension of Thermoplastics." *Polymer Engineering and Science,* 28(19) (1988): 1209-1218.

22. Swallowe, G. M., *Mechanical Properties and Testing of Polymers.* Dordrecht: Kluwer Academic Publishers, 1999.

23. Szilard, R. *Theories and Analysis of Plates.* New Jersey: Prentice-Hall, 1974.

24. Timoshenko, S. P., and Gere, J. M. *Theory of Elastic Stability.* New York: McGraw Hill, 1961.

25. Tlilan, H. M., Sakai, N., and Majim, T. "Effect of Notch Depth on Strain-Concentration Factor of Rectangular Bars with Single-Edge Notch Under Pure Bending." *International Journal of Solids and Structures,* 43(3) (2006): 459-474.

26. Tou, G., and Zihui, X. "Mean Stress/Strain Effect on Fatigue Behavior of an Epoxy Resin." *International Journal of Fatigue,* 29(12) (2007): 2180-2190.

27. Ugural, A.C. *Stresses in Plates and Shells Second Edition.* New York: McGraw-Hill, 1999.

28. Wang, C. M., Nazmul, I. M., and Wang, Q. "Exact Bending Solutions of Axisymmetric Reissner Plates in Terms of Classical Thin Plate Solutions." *Advances in Structural Engineering,* 7(2) (2004): 129-145.

29. Wescott, R., Semple, B., and Heller, M. "Stress Analysis of Near Optimal Surface Notches in 3D Plates." *Journal of Mechanical Design,* 127(6) (2005): 1173-1183.